Adaptive proportional resonant controller for single-phase grid-connected PV inverter based on grid impedance estimation technique

Hamza O Khalfalla

B.Sc., M.Sc.

A thesis submitted for the degree of

Doctor of Philosophy

July 2019

School of Engineering

Newcastle University

United Kingdom

Abstract

Photovoltaic PV systems have shown a significant growth in recent years driven by the increased efficiency and reductions in the cost of PV modules. Today, distribution generation based PV systems have a major contribution to the total electricity production worldwide. However, in areas with high penetration of PV system connected to the grid, interaction may arise between the grid and PV system. This research focuses on the effect of grid operating conditions on the performance of grid-connected PV inverter systems. A simulation model of the system under investigation has been developed to evaluate the impact of frequency deviation, grid voltage distortion and grid impedance variation on the harmonic performance of the injected current as well as the voltage at the point of the common coupler. Proportional resonance PR controller is employed to regulate the current produced from the PV inverter due to its reputation in tracking sinusoidal signals. The obtained simulation results demonstrate that the harmonic performance of the grid current and PCC voltage can be significantly influenced by the change of grid operating conditions. In particular, grid impedance variation can result in a shift in the system resonance frequency leading to distortion in network current and voltage. To adapt the PR controller to the grid impedance variation, a novel adaptive PR controller which takes into account the change in grid impedance is proposed. The adaptive consists of a high-order digital band-pass filter and chain of statistical signal processing technique. Simulation results show that the harmonic performance of grid current and PCC voltage can be enhanced and the proposed APR controller is robust against impedance variation. Finally, the proposed control method is experimentally implemented and the obtained results validate the effectiveness of the proposed control structure.

List of Contents

List of Tables

List of Figures

Abbreviation and Symbols

Abbreviations

AC	Alternative Current
ADC	Analogue to Digital Converter
APR	Adaptive Proportional and Resonant
BP	Band Pass
BPF	Band Pass Filter
CCS	Code Composer Studio
CSP	Concentrating Solar Power
DC	Direct Current
DG	Distribution Generation
DSP	Digital Signal Processing
DAC	Digital to Analogue Converter
ESR	Equivalent Series Resistance
FFT	Fast Fourier Transform
FLL	Frequency Locked Loop
FRT	Frequency Ride Through
GCB	General Control Board
GUI	General User Interface
HC	Harmonic Compensator
IEA	International Energy Agency
IEEE	Institute of Electrical and Electronic Engineering
IET	Institute of Engineering and Technology
IGBT	Isolated Gate Bipolar Transistor
LF	Loop Filter

LPF	Low Pass Filter
PCC	Point of Common Coupling
PV	Photovoltaic
PI	Proportional and Integral
PR	Proportional and Resonant
PD	Phase Detector
PF	Power Factor
PR+HC	Proportional and Resonant with Harmonic Compensator
PLL	Phase Locked Loop
p-PLL	Power Phase Locked Loop
PSO	Partial Swarm optimization algorithm
PWM	Pulse Width Modulation
RE	Renewable Energy
MOSFET	Metal Oxide Field Effect Transistor
MPP	Maximum Power Point
MPPT	Maximum Power Point Tracking
THD	Total Harmonic Distortion
TI	Texas Instruments
VCO	Voltage Controlled Oscillator
VRT	Voltage Ride Trough
VSI	Voltage Source Inverter
ZCD	Zero Crossing Detection
ZOH	Zero Order Hold

Symbols

C_f	Filter capacitor
f	Frequency
I_{in}	Inverter output current

Imeas	Measured current
Iref	Reference current
Ithd	Current total harmonic distortion
K_P	Proportional gain
K_I	Integral gain
K_R	Resonance gain
L_1	Inverter side inductor
L_2	Grid side inductor
L_g	Grid inductor
R_1	Series resistance of inverter side inductor
R_2	Series resistance of grid side inductor
R_d	Damping resistance
R_g	Grid resistance
T	Sampling time
V_{inv}	Inverter output voltage
V_{PCC}	Point of common coupling voltage
V_g	Grid voltage
V_{DC}	DC Voltage
Vthd	Voltage total harmonic distortion
ω_0	Fundamental frequency (rad/sec)
ω_{res}	Resonance frequency (rad/sec)
Zg	Grid impedance

Acknowledgment

First and foremost, all praises is due to Allah Almighty (God), the most merciful and the most gracious, who gives me wisdom, health and patience to finish this work. The author would like to express sincere gratitude to those who have made this thesis possible.

A particular thanks to the Libyan Ministry of Higher Education and Scientific Research, and the general electricity company of Libya (GECOL), for sponsoring this research, as without their funding this work would not have been carried out.

Many thanks are given to my research supervisors Professor Volker Pickert, Dr Salaheddine Ethni, Dr Maher Al-Greer and Dr Matthew Armstrong for their support, assistance and guidance. It is such a pleasant experience to work with them and learn from their experience that helped me through all the difficulties.

I would like to thank the technical support staff within the department; Darren, Gordon Marshal, Allan Wheatley, and James Richardson, in helping with the equipment required for this project. Also, special acknowledgement must go to Gill Webber, the postgraduate research coordinator, for her support and great help.

Finally I would like to thank my Family who are helped me about the previous education in order to reach this stage and support me a lot. A special thank must go to my wife for her quiet patience, daily devotion and moral support. I would like to thank my lovely kids for their warm hugs and lovely smile.

INTRODUCTION

1.1 Background

Despite the fact that meeting world demand for electricity still depends on based fossil fuel conventional resources, the overall share of renewable energy (RE) sources has increased dramatically in recent years. Many factors have contributed to this rapid change including; the depletion of primary energy sources, the liberalization of electricity markets, and climate change concerns [1]. Among others, these trends have led to the dramatic development and lowering of costs of several RE technologies. Renewable energy sources such as wind and solar power are potentially promising solutions that can provide clean and affordable energy. The generating capacity of RE sources has experienced the largest annual increase by the end of 2017, with more than 160 gigawatts (GW) of additional capacity. This is an increase of 9% compared to 2017 [2]. Figure 1-1 reveals the generating capacity of global RE sources in the six leading countries.

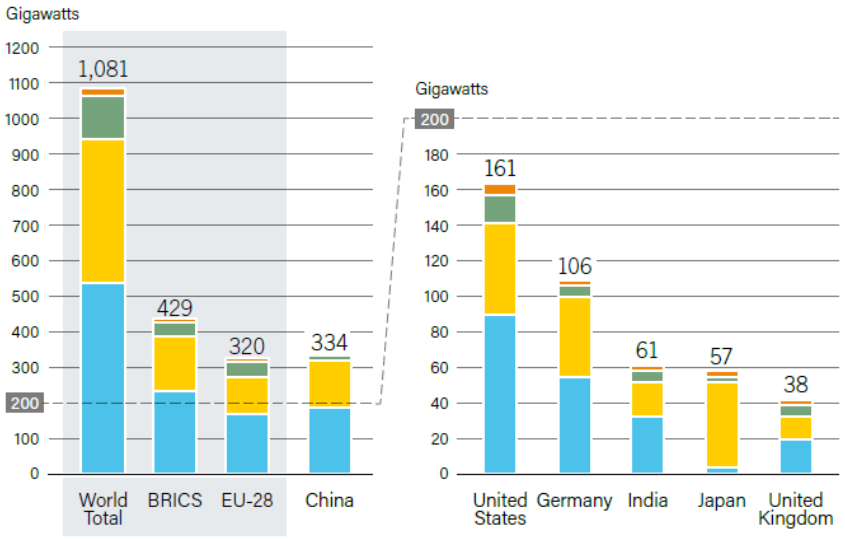

Figure 1-1 Renewable energy capacities in the world and top six countries, 2018 [2]

According to this figure, China, the United States, and Germany are the top three countries in terms of the total installed capacity of RE sources.

According to a global report published in 2018, the year 2017 was another record-breaking period for the RE sector. The statistics in the report indicate that renewable power capacity showed the largest ever increase accompanied by a remarkable fall in costs. It was also claimed that the number of cities powered by at least 70% of electricity generated from renewable energy sources have had more than doubled between the years 2015 and 2017, to a total of 101 cities [3].

1.2 Photovoltaic systems

In particular, photovoltaic PV systems which utilize solar power to generate electricity, have shown significant growth in recent years, with an average annual rate of increase of 60%. This has been driven by the increasing efficiency and reductions in the cost of PV modules [4]. For instance, it has been reported that PV capacity in 2017 had increased by a factor of 43.14 from just 8 GW in 2007 to a new record figure of 400GW worldwide in 2018, as depicted in the cumulative global installation data given in Figure 1-2 [2].

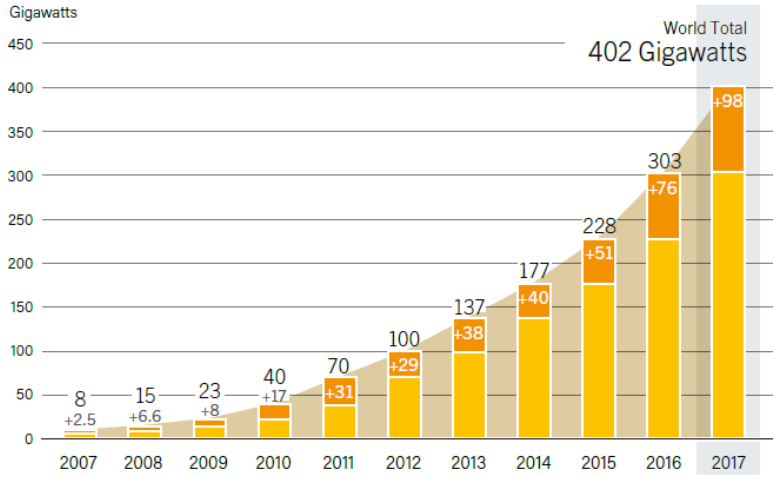

Figure 1-2 Solar PV global capacity and annual additions, 2007-2017[2]

The installation of solar PV conversion systems is expected to expand even faster, encouraged by cost reductions, and the development of technology as well as increasing efficiency. The International Energy Agency (IEA) predicts that almost 16% of global electricity will be provided by solar PV systems by the end of 2050. The proportion of

installed PV capacity involves grid-connected PV systems which account for more than 99% compared with off-grid stand-alone systems. Nevertheless, numbers of stand-alone systems are growing rapidly [4].

Another emerging promising technology that accommodates solar power is concentrating solar power (CSP), which uses solar thermal power to produce electricity. In principle, CSP transforms solar irradiation into heat during daylight. The collected heat power is then stored in equipped thermal energy storages and is used for electricity generation [5].

1.2.1 Grid-connected PV inverter systems

In a conventional grid-connected PV systems, a power electronic converter, usually a voltage source inverter (VSI), is placed between the PV generators and the grid. In some applications, current source inverters (CSIs) have also been proposed and implemented due to the high fault tolerance capability for high power applications and smooth output waveforms [6], [7].

Several VSI topologies exist in single-phase and three-phase PV inverter systems, depending on the level of power required. Very common topologies are include two-level and three-level voltage H-bridge inverters. Half-bridge two-level inverters are also popular, in which the switching frequency and DC-link must be doubled in order to obtain the same performance as in full bridge inverters. Although the two and three-level topologies are very common, they are associated with some drawbacks which include high switching losses and high *dv/dt* ratios, which necessitate special care in filter design and the installation of interfacing transformers [8]. The need to minimize switching frequency losses has led to the development of multi-level converters. If the individual switches in the typical inverter are replaced by a number of cascaded semiconductor switches, then the multi-level converter will be shaped [9]. Multi-level converters are preferred in high voltage applications since they provide several voltage levels at low switching frequency with minimum switching losses as well as smaller size of filter components [10].

1.2.2 Classification of grid-connected PV inverter systems

In general, PV systems can be divided into two main categories: stand-alone and grid-connected systems. The former are employed to supply local loads such as residences

without any interaction with the utility grid. Energy storage devices such as batteries are usually required in stand-alone systems, so as to satisfy demand during periods of low irradiation in the daytimes or at night. On the other hand, grid-connected PV systems which are within the scope of the present research, are connected to the distribution system as well as local loads. In this manner, grid-connected PV systems are required to operate in grid-tied mode in normal operating conditions, and in off-grid mode in cases of emergency such as system outages [11]. Switching between the two modes has to be smooth and seamless in order to provide the reliable and safe operation of the whole system [12]. Figure 1-1 shows the different classifications of PV systems.

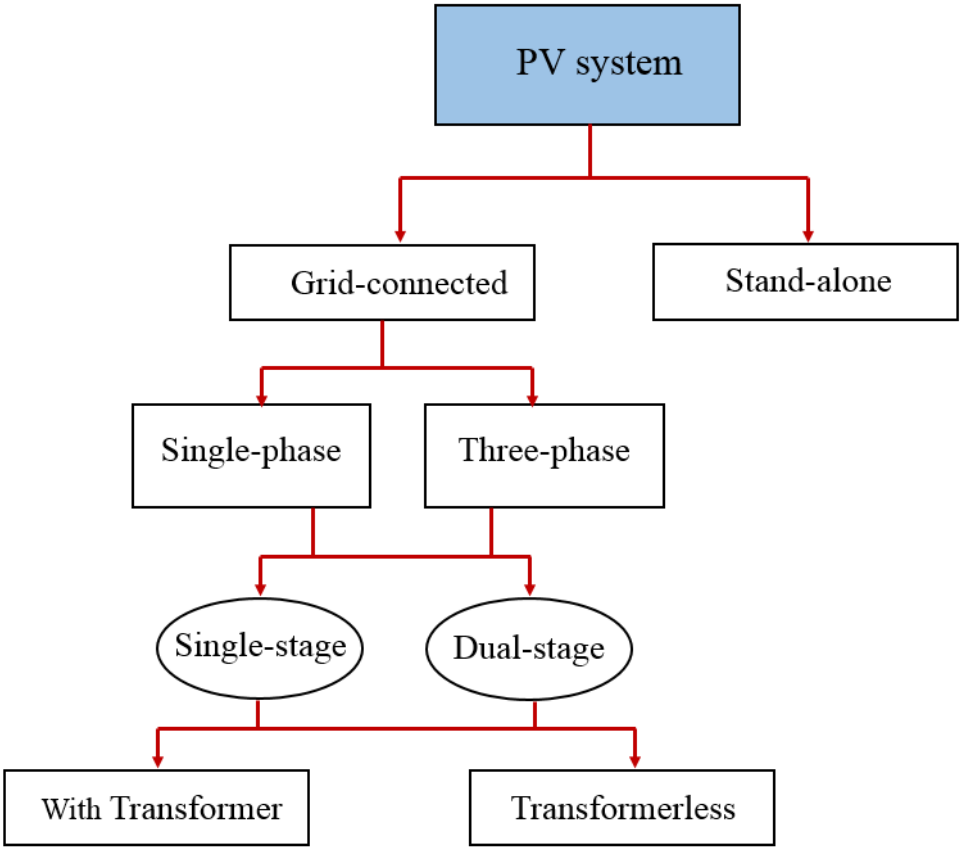

Figure 1-3 Classification of PV systems

The figure shows that grid-connected PV systems can be designed as single-phase, where the energy demand is considerably smaller, and in this case the PV system is connected to the low-voltage distribution system where the voltage is 240V.

Alternatively, three phase system are used for higher power applications, where the PV system can be connected to either a low- or medium-voltage system.

Furthermore, the topology of grid-connected PV systems can be classified as single- or dual-stage systems, based on the number of power conversion stages. In a single-stage topology, the grid- connected PV system consists of only one power inverter which converts the DC voltage into AC components [13]. This inverter is desired to be responsible for handling all tasks including extracting the maximum power from PV arrays by means of a maximum power point tracking (MPPT) algorithm, regulating the output current from the inverter, and grid synchronisation [14].

The typical arrangement of a single-stage PV inverter system is depicted in Figure 1-4 a. Its advantageous include that, this topology is considered to be highly efficient in terms of power conversion and cost effective compared with the dual-stage topology due to its simple structure and low number of counted components. However, these systems suffer from limitations in terms of power capacity, which means that more PV modules are required to provide a higher PV array voltage. Moreover, as the MPPT algorithm is an essential part of the control scheme, this means that overall control can be more complex [15], [16].

On the other hand, the dual-stage configuration shown in Figure.1-4 b is currently the most common approach in grid-connected PV inverter systems. They employ a DC/DC converter, which usually a boost or buck-boost type, as the first stage. This additional converter is placed between the PV arrays and the inverter. Includes stepping up the voltage produced by the PV arrays, the DC/DC converter performs the MPPT to extract the maximum power that can be obtained from the PV arrays [17].

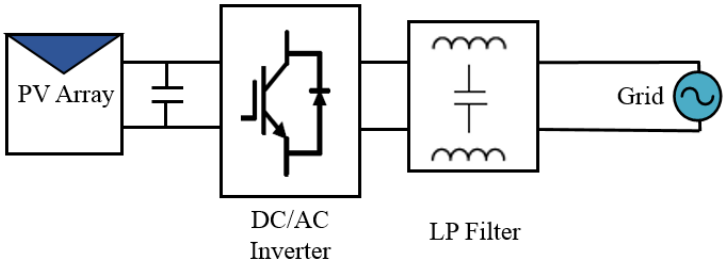

(a) Single-stage PV Inverter system

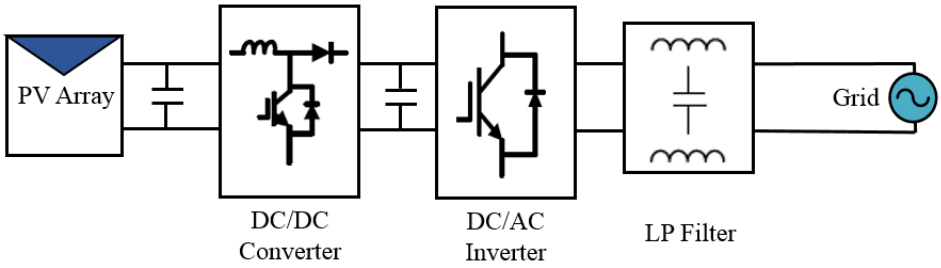

(b) Dual-stage PV Inverter system

Figure 1-4 Grid connected PV system (a) Single-stage (b) Dual-stage

Up to now, several MPPT methods have been proposed and implemented, the most popular techniques are; incremental conductance (Inc.C), perturb and observe (P&O), short-circuit, and open-circuit voltage [18], [19], [20]. The second stage of the system is the DC/AC inverter which regulates the inverter's output current. Compared with single-stage topologies, dual-stage systems are able to operate with larger power capacity as well as wide range of PV output voltages. In addition, the control function in this topology, which includes for example the MPPT, DC voltage control and reactive power compensation, can be easier as the two stages are controlled separately [21]. However, some drawbacks are linked to this topology; in particular, high power conversion losses, low efficiency, bulky size and high cost [22], [23].

Another important part of the system is the low-pass filter, which is placed at the inverter output. The task of the filter is to prevent the harmonic components which resulted from the high PWM switching frequency from being injected into the utility grid. The commonly implemented filters types are L, LC, and LCL filters, the latter type is preferred as it provides impressive harmonics attenuation even at lower switching frequency and is smaller in size compared with L and LC filters [24], [25].

1.2.3 Transformer and transformerless grid-connected PV inverter systems

The classification chart given earlier in Fig 1-3, shows that the typical grid-connected PV systems can be interfaced to the utility grid with or without an isolation transformer. If included, the isolation transformer can be either a high-frequency transformer (HF), or low-frequency transformer (LF) [26], as shown in Figure 1-5. The function of transformer is to provide a galvanic isolation for safety purposes, on the one hand, and to prevent the DC current injection from being inserted into the grid on the other hand [27]. The presence of leakage current is mainly linked to the common-mode voltages being conducted in the loop, with the parasitic capacitors between the ground and the solar arrays. Although the implementation of the isolation transformers provide safe operation, they increase the size of the inverter and the cost, and also reduces the system efficiency. Recently, transformerless inverters have become more attractive due to the associated higher efficiency and performance, lower cost, and smaller size [28, 29].

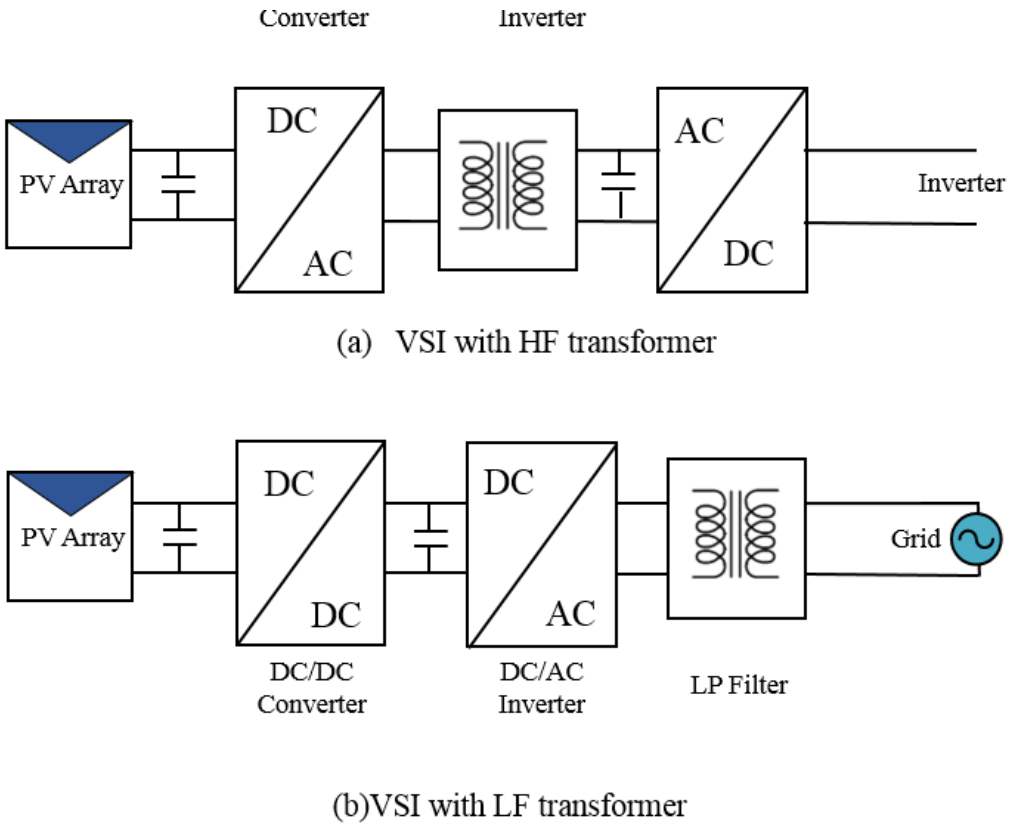

Figure 1-5 Transformers in grid connected PV inverter

In some countries, the implementation of isolation transformers is not mandatory, based on their local regulations. In this case, several power converter topologies combined with specific control scheme have been designed, in order to minimise the effects of leakage current in transformerless topologies. For example, the grid neutral may be connected to the mid-point of the DC link capacitor, and this is supposed to prevent voltage fluctuation by continuously clamping the grid neutral with PV arrays [30].

1.3 Operation requirements of PV grid-connected inverter systems

The proliferation of grid connected PV inverter systems has become a substantial part of distribution generation systems in many countries. The high penetration of such intermittent systems might influence the operation of the power grid. In general. PV systems are required to be reliable, safe, and efficient in order to meet performance requirements and to fulfil legal regulations. To achieve this, protective equipment and suitable preventative measures must be developed [31]. Apart from system efficiency, performance requirements can be linked to the control functions of the system in different respects while legal requirements are linked to the security of system operations. According to a previous review [32], there are various challenges associated with the operation of the PV system, these are summarised in the following points:

- Voltage fluctuations including unbalances and voltage rise.
- Variations in reactive power flow.
- Voltage and current harmonic distortion.
- DC current injection.
- Islanding detection.
- Power factor variations.
- Grid impedance variations.

1.3.1 Power quality requirements

The power quality requirements of PV grid-connected systems can be associated with four main issues: harmonic distortion, DC injection, voltage unbalance and flickers.

All of them are required to comply with codes and standards defined by international and national committees as well as local governments, in order to ensure high quality and normalized operation. With regards the power quality, the amendment IEEE 1547-2014 [33], and IEC 61727-2008 are international standards, in which strict limits have been defined to be considered in PV grid-connected inverter systems. Both standards emphasise that the total harmonic distortion (THD) of the injected grid current must be less than 5%. Limitation are also defined to the individual odd and even harmonics [34]. If the THD limits have been exceeded, the quality of power produced would be potentially lower, and the risk of disruption will be higher. As this research is interested in power quality, practically current and voltage total harmonic distortion, the harmonic injection is highlighted as follow.

1.3.2 Anti-islanding detection

In grid-connected PV systems, the islanding phenomenon occurs when the grid has tripped but the PV inverter continues to supply power to the local load. This undesirable phenomenon can result from interruptions or abnormalities in the network, such as the opening of protection devices due to faults or voltage shut-down. If the PV system stays connected in this case, equipment and staff will be at risk and several hazards can be highlighted [35]. To avoid the islanding of PV inverter systems, different anti-islanding detection techniques have been proposed and implemented. They are usually classified as passive or active methods [36]. Passive methods employs the already existing measurement devices for voltage, current and frequency at the point of common coupling, in order to detect the islanding. Meanwhile, active methods are carried out by introducing small signals as a disturbance to the system. Based on the system response the islanding events can then be detected.

1.4 Objective and scopes of the research

The presence of grid-connected PV inverter systems can affect the distribution network in different ways. For instance, power quality issues like THD might arise when high numbers of such systems being tied to the grid. In addition, the interaction between PV inverters and the grid can have a significant impact on system reliability and controllability. The system's power quality can be improved by means of a

superior control scheme, taking into account those factors which contribute to unreliable performance and abnormal operation.

The main aim of this research is to improve the power quality of single-phase grid-connected PV inverter systems. The research objectives are summarised as follow:

- To review the control strategies implemented in grid-connected PV inverter systems.
- To study the effect of changeable grid operating conditions on system performance. These include distortion in grid voltage, grid frequency deviations and grid impedance variations.
- To develop an effective simulation model as well as an experimental test rig for the system under consideration in order to validate the proposed techniques.

1.5 Contribution

The contributions of the research are summarised as follows:

- The interaction between the PV inverter system and the distribution grid has been investigated. This includes an investigation of the influence of changeable grid operating conditions.
- A novel grid impedance estimation technique is developed to predict changes in grid impedance. The proposed method is simple and requires no additional hardware. Moreover, it can be easily implemented.
- An adaptive control scheme based on digital PR controller has been developed, and full details of the design process are presented. The implementation of the proposed controller validates the robust performance of the system under a wide range of grid impedance variations.

1.6 Publications

The course of this research has resulted in the following published papers and posters:

- **H. Khalfalla**, S. Ethni, Maher Al-Greer, V. Pickert, M. Armstrong, and Van Thang Phan "An adaptive proportional resonant controller for single-phase grid connected inverter based on bandpass filter techniques", *11th IEEE*

International Conference on Compatibility, Power Electronics and Power Engineering (CPE-POWERENG) 2017. Cadiz-Spain

- **H. Khalfalla**, S. Ethni, M. Shiref, Maher Al-Greer, V. Pickert, M. Armstrong " Grid impedance estimation based on digitalized band-pass filter for single phase PV grid connected inverter" *,53rd IEEE International Universities Power Engineering Conference UPEC, 2018, Glasgow, UK.*
- S. Ethni, A. Smith, **H. Khalfalla**, M Shiref " Open circuit stator winding fault detection of induction machine from transient data using nature inspired optimization" *53rd IEEE International Universities Power Engineering Conference UPEC, 2018, Glasgow, UK.*
- **H. Khalfalla**, S. Ethni, N. B. Kadandani, V. Pickert " Resonance Frequency Detection Technique in Grid-connected Inverter Systems Based on Double-order Digitalized Filter" *10th International Renewable Energy Congress, 2019 Sousse-Tunisia*
- Chenming Zhang, Weichi Zhang, Salaheddine Ethni, Mohamed Dahidah, and Volker Pickert, **Hamza Khalfalla** " Online Condition Monitoring of Sub-module Capacitors in MMC Enabled by Reduced Switching Frequency Sorting Scheme" *10th International Renewable Energy Congress, 2019 Sousse-Tunisia*
- Nasiru B. Kadandani, Salaheddine Ethni, Mohamed Dahidah and **Hamza Khalfalla** "Modelling, Design and Control of Cascaded H-Bridge Single Phase Rectifier" *10th International Renewable Energy Congress, 2019 Sousse-Tunisia*
- The award of best poster presented in the annual research conference, ARC2016, Newcastle University 2016 Newcastle upon Tyne 2016.
- Poster presented at Centre for Power Electronics Postgraduate Summer School, 2017 Loughborough University, Loughborough UK

1.7 Thesis overview

This thesis is divided into seven chapters. This chapter briefly describes the development of renewable energy systems with attention paid to PV systems. Moreover, a classification of grid-connected PV inverter systems is provided, including a brief overview of its operating requirements. In chapter two, a review of conventional current control method has been presented along with their classification, mathematical derivation of the proportional and resonance PR controller is provided and integrated with previous research on PR controller. In order to tackle issues related

to the time-varying grid operating conditions, advanced control strategies based on the concept of resonance controllers are discussed. In addition, grid impedance estimation techniques that can be utilized for adaptive control are also presented.

In chapter three, the modelling and design of single-phase grid-connected PV inverter is demonstrated, firstly the modelling of an H-bridge inverter with PWM techniques followed by the modelling of a low-pass LCL filter. Furthermore, this chapter presents the modelling of PI and PR controllers. As the control scheme in this research is based on the PR controller, the selection criteria for its parameters are also highlighted. The overall modelled system is built using Matlab/Simulink software and is used throughout the thesis to demonstrate the interaction between the distribution grid and the PV inverter. Finally, a stability analysis of the modelled system is provided.

The fourth chapter introduces the Simulink model the single-phase grid-connected PV inverter system, which includes the Simulink model of a distorted grid voltage and the synchronisation algorithm. In order to understand the interaction between the distribution system and the PV inverter system, an extensive study of the influence of grid operating conditions on the PV inverter systems is provided. This study includes the effects of distorted grid voltage, and variation grid impedance, and grid frequency.

Chapter five starts with a brief overview of the grid impedance estimation method. This is followed by introducing the proposed adaptive PR controller. The design process of the analogue and digital band-pass along with statistical signal processing is also presented. In addition, the chapter provides the simulation results for the online adaptation of the look-up table for the tuning of the PR controller using a particle swarm optimisation algorithm.

1.8 Chapter summary

In this chapter, a general discussion of grid-connected PV inverter systems is provided. The rapid increase in the numbers of such systems in distribution generation system is also highlighted, including their classification and operational challenges. The objective and scope of the present research have also been defined as well as the contribution of the research and publications. The next chapter focuses on the control strategies that are applied to regulate the injected grid currents and especially on the implementation of adaptive control.

CHAPTER 2

LITERATURE REVIEW

2.1 Introduction

One of the most important aspects of the integration of PV systems is their control design. As the power produced from PV arrays mainly depends on atmospheric conditions, such as irradiation and temperature, a robust control scheme is required to ensure that the PV system is working at its maximum efficiency irrespective of these conditions. The control scheme is also required to inject high quality power into the grid according to the precisely defined standards and regulations associated with the interconnection of PV systems.

2.2 Review of conventional current control methods

A typical structure for a dual-stage grid-connected PV system with its general control functions is shown in Figure 2-1. As can be seen, the control functions are divided into two main parts: input-side control and grid- side control

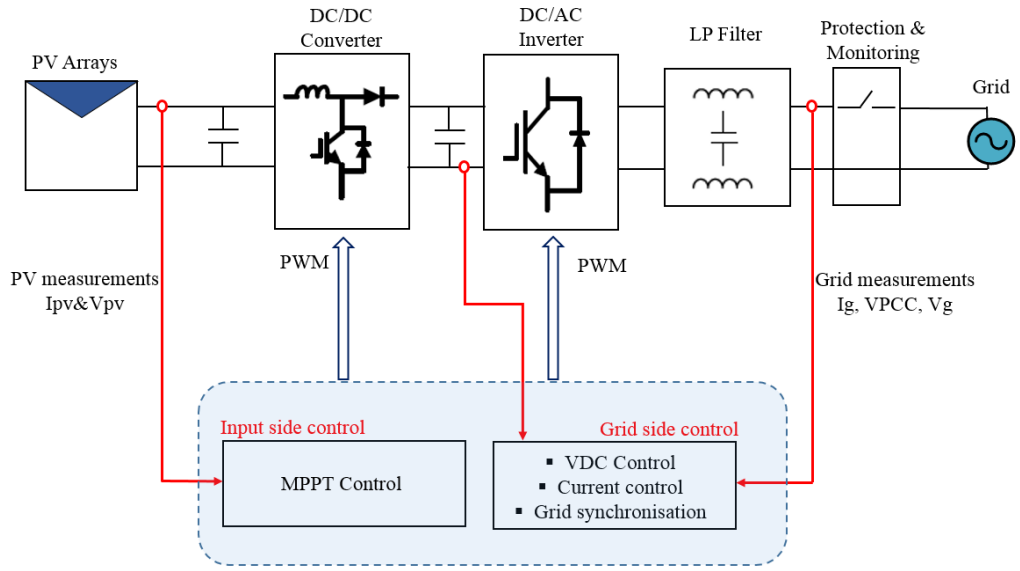

Figure 2-1 General structure of grid-connected PV system with control functions

The input-side control is responsible for obtaining the maximum power from the PV source. DC to DC buck boost converters and highly efficient MPPT algorithms are typically employed to accomplish this task. The converter task is to meet the requirements of the voltage levels whereas the MPPT algorithm forces the input source toward its maximum power. In addition, the protection of DC/DC converters is also considered in this part. It is worth mentioning that input-side control is beyond the scope of the present research, and thus is not discussed further. Meanwhile, grid-side control is responsible for injecting high quality sinusoidal current into the grid. The injected current must be in phase with respect to the grid voltage. Moreover, this part is responsible for controlling the active power injected to the grid and controlling the transferred reactive power between the PV inverter system and the grid. It also control the DC-link voltage. These responsibilities are the basic features that a grid-connected PV inverter system should fulfil. Other ancillary services such as voltage and frequency regulation and active filtering might be also required. In this research focuses on grid-side control in particular, the control of the current injected into the grid. The next section provides a discussion of the control strategies applied for the grid-side converter.

2.3 Classification of current controllers

The generic strategy applied to control grid-side inverters consists of two cascaded control loops, an inner control loop and an outer control loop. The former is the faster loop which regulates the injected grid current. It also responsible for power quality issues and current protection, while the latter loop is responsible for controlling the DC-link voltage and for balancing the power flow in the system [37], [38]. Figure 2-2 shows a classification of current controllers in regards to the implemented reference frame. In the context of this review, the main properties of each class are highlighted.

2.3.1 Natural reference frame control

Natural reference frame control uses non-linear controllers such as dead-beat [39], [40], or hysteresis [41], [42] controller, to control the grid current. In hysteresis control, the output current of the inverter is compared with the desired reference current. The resulting error signal which is restricted within a fixed hysteresis band is fed to a hysteresis comparator to generate the switching signal. This controller is preferred due

to its high dynamic response, ease of implementation and robustness to load change [43]. However, it suffers from the presence of a variable switching frequency in the output voltage and ripple current in the output current from the VSI, which requires special consideration in the design process of the LCL filter [44].

2.3.2 Synchronous reference frame control

Synchronous reference frame is a linear control design which uses an *abc-dq* module for the transformation of the reference frame to determine the *dq* components. The grid current and voltage signals are transformed into a reference frame that rotates synchronously with respect to the grid voltage. In this way, the control variables are changed to DC components so that the control actions can be easily achieved. A proportional integral PI controller is usually adopted in the synchronous reference frame, because of its superior performance in the regulation of DC variables [45]. However, the major drawbacks of PI controller are poor compensation capability for low order harmonics and the presence of steady-state error in single-phase applications.

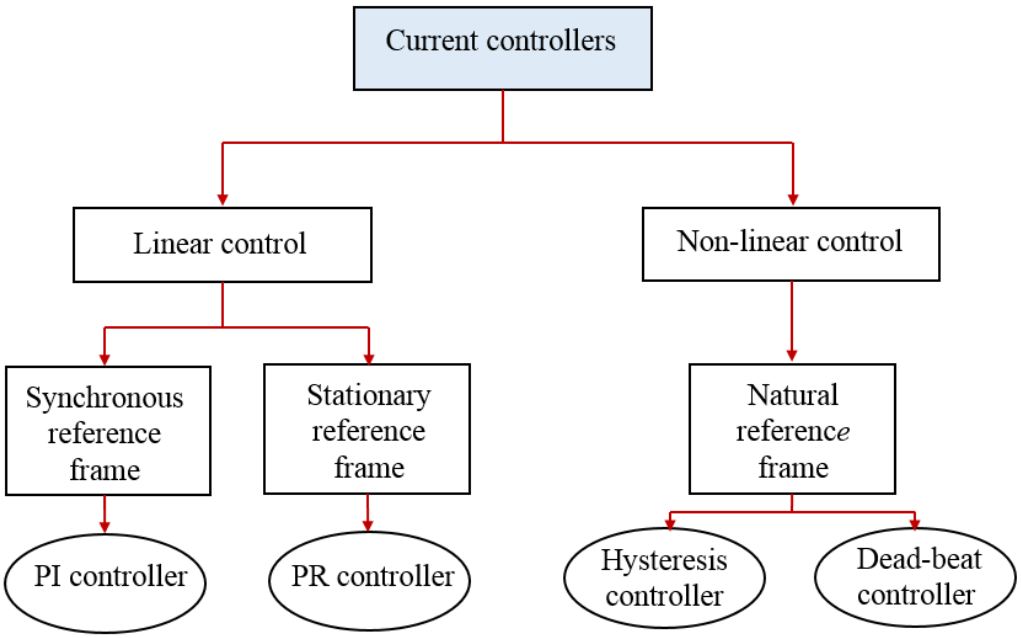

Figure 2-2 Classification of current control methods

2.3.3 Stationary reference frame control

Stationary reference frame control uses an *abc-αβ* module to transform the grid current into *αβ* components. The control variables in this case are sinusoidal waveforms, and thus a PI controller is not suitable. Alternatively, a proportional resonance PR controller may be employed [46]. The main advantageous of PR controllers are that they can achieve infinite gain around the resonance frequency, and thus the steady state error will be eliminated. Also the complexity of the controller is lower as they already implemented in the stationary frame, and selective harmonic compensators can be added to the control structure for the further elimination of low-order harmonics [47].

Synchronous and stationary reference frames are suitable for three-phase systems. This is not the case for single-phase systems as the circuit has one conductor with a neutral return. To extend the control strategy of these frames to single-phase systems, an additional orthogonal signal has to be generated to create a single-phase circuit with an equivalent two-phase circuit [48]. Several methods have been reported in the literature for generating orthogonal signals from the original single-phase signal including the Hilbert transform [49], all-pass filter [50] and transport delay [51].

2.4 Review of stationary frame PR controllers

The suitability of PR controllers for current control in grid-connected PV inverter systems relies on the enhancement of the performance of reference tracking. This is particularly important in the alleviation of the major drawbacks associated with conventional PI controllers. For single-phase systems, these major drawbacks includes the presence of steady-state error, poor disturbance rejection capability and the complexity of implementing selective harmonics compensators. These drawbacks can be easily avoided by using stationary reference frame PR controllers while still achieving the same frequency response characteristics as with a synchronous reference frame PI controller. The PR controller introduces infinite gain at a selected resonant frequency and almost no gains outside of this frequency therefore providing zero steady-state error at this particular frequency. This functionality is conceptually similar to that of an integrator whose infinite DC gain pushes the DC steady-state error to zero. In fact, the use of PR controllers offers many other advantages compared to PI

controllers, such as the saving of computational time and avoiding the complexity associated with multiple frame transformation in three-phase systems. Direct implementation is also possible in single-phase systems, along with less sensitivity to noise and error in synchronisation.

2.4.1 Derivation of the PR controller transfer function

The equivalent transfer function of the PR controller can be derived using a frequency domain approach because it clearly demonstrates similarities between the stationary frame PR controller and their equivalent in the synchronous reference frame [52], [53]. The relationship between the *dq*-components in the synchronous reference frame and in the *αβ*-components in stationary reference frame are given in equations 2.1 and 2.2:

$$i_d = i_\alpha \cos(\omega_0 t) + j i_\alpha \sin(\omega_0 t) = i_\alpha e^{j\omega_1 t} \tag{2.1}$$

$$i_q = i_\beta \cos(\omega_0 t) - j i_\beta \sin(\omega_0 t) = i_\beta e^{-j\omega_1 t} \tag{2.2}$$

The transfer function of the PR controller can be obtained by applying a frequency shift of ± ω1 at all frequencies in the frequency domain of the equivalent transfer function in the stationary frame PI controller implemented in positive and negative sequences of the synchronous reference frame:

$$G_{PI}(s) = K_P + \frac{K_I}{s} \tag{2.3}$$

$$G_{PR}(s) = G_{PI}^{+}(s) + G_{PI}^{-}(s) \tag{2.4}$$

$$G_{PR}(s) = G_{PI}^{+}(s - j\omega_1) + G_{PI}^{-}(s + j\omega_1) \tag{2.5}$$

$$G_{PR}(s) = k_P + k_I \frac{s}{s + \omega_1} + k_P + k_I \frac{s}{s - \omega_1} \tag{2.6}$$

$$G_{PR}(s) = 2k_P + 2k_I \frac{s}{s^2 + \omega_1^2} \tag{2.7}$$

Equation 2.7 can be simplified to form the transfer function of the ideal PR controller as follows:

$$G_{PR}(s) = K_P + K_I \frac{s}{s^2 + \omega_1^2} \tag{2.8}$$

The last equation shows that $G_{PR}(s)$ consists of proportional and resonant terms. The resonant term has a direct effect at the resonant frequency and almost no contribution outside this frequency, thus the frequency response is shaped by the proportional gain [54].

The ideal form of the PR controller given in equation 2.8 cannot be implemented in practices because of the infinite gain, alternatively, the non-ideal PR controller is adopted. The non-ideal PR controller can be obtained using the same previous steps and employing the non-ideal integrator of $G_{PI}(s)$ given in equation 2.9

$$G_{PI}(s) = K_P + \frac{K_I}{1 + s/\omega_c} \tag{2.9}$$

Substitution this in equation (2.6) yields:

$$G_{PR}(s) = K_P + K_I \frac{K_I \omega_c s}{s^2 + 2\omega_c s + \omega_1^2} \tag{2.10}$$

Which is the equivalent transfer function of the PR controller, where ω_c is the cut-off frequency and ω_1 is the fundamental frequency.

2.5 Previous research on PR controllers

Due to their advantages, resonant controllers have been widely employed in different power converter applications such as PV inverters [38], wind turbines [55], active power filters (APFs) [56], uninterruptible power supplies (UPSs) [57], induction drives [58], and double-fed induction generator DFIGs [59].

The concept of resonant current control has been primarily implemented in three-phase active filter applications, where the concept of generalized integrators for sinusoidal signals was proposed [60]. A comprehensive review of PR controllers has been

published in [47] in which the relevant theory has been revised in detail along with previous practical implementations.

In another study [61], the P+Resonant controller has been presented as a new type of stationary reference frame regulator for a DC servo control system. Using this approach, the performance of the new controller was found to be virtually the same as that of a synchronous reference frame PI controller in terms of transient and steady-state operations. A significant advantage of the P+Resonant controller is its suitability for both single- and three-phase systems.

A new control structure for grid-connected PV inverters based on PR controller was subsequently developed [38], where in addition to the PR controller which tuned at the fundamental frequency, several harmonic compensators (HCs) were combined within the control strategy to compensate for the 3rd, 5th and 7th order harmonics. The control strategy of the PR controller with parallel HCs is depicted in Figure 2-3. A comparison was carried out between this approach and that using a conventional PI controller based on the experimental results of a DSP-controlled 3 kW PV inverter system. The main outcomes from this approach are that the steady-state error was eliminated, the use of HCs did not influence the controller's dynamics, and a considerably lower current THD was obtained compared to that with the PI controller.

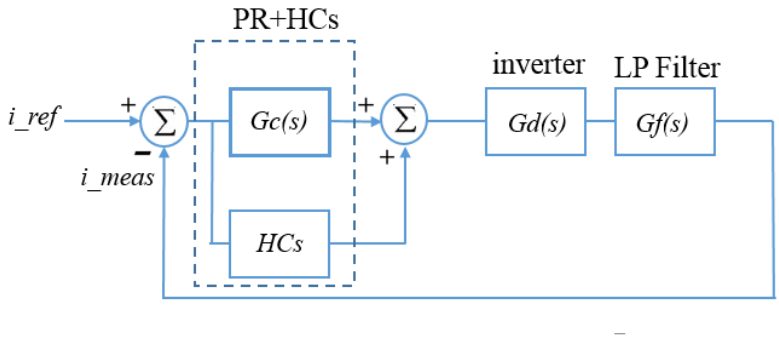

Figure 2-3 Control strategy of PV inverter based on PR controller with parallel HCs

In another approach [62], the HCs were implemented in series with the tracking regulator instead of using parallel implementation. This arrangement was applied in an experimental system with a single-phase grid-connected PV inverter. Although the main aim of adding the HCs is to compensate for selected harmonics, the finding from this study validated other important features such as the efficient attenuation of the

grid voltage background distortion which resulted in lower levels of current THD, accurate synchronisation with grid voltage without the need for a phase-locked loop PLL, and less computational time compared to that of parallel implementation. Figure 2-4 shows the proposed control strategy in which the proportional and resonant parts of the PR controller are denoted by K_P and P_R respectively and the HCs represent the selected harmonics to be compensated for.

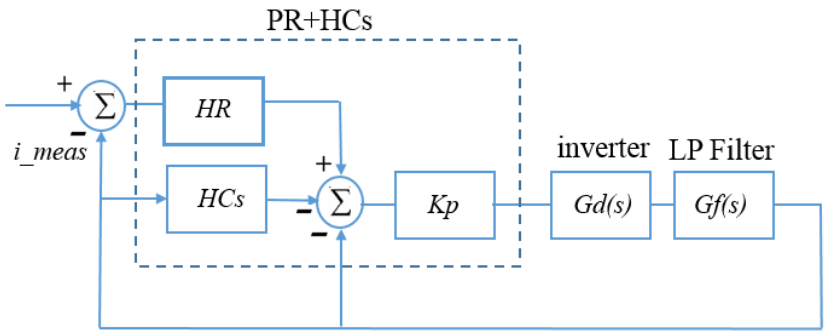

Figure 2-4 Control strategy of PV inverter based on PR controller with series HCs

In a study of the suitability of implementing PR current controllers for a VSI with LCL filters taking into account voltage sensor-less operation [63], the grid current was synchronised with the grid voltage using a virtual flux (VF) estimation method. The successful implementation in this study was supported by an extensive stability analysis based on simulation results which showed that the current controller worked at optimal performance within the region of stability. A new current feedback method and PR control strategy for grid-connected inverters was then proposed [62]. Unlike in the usual cases, now the grid-side and inverter-side currents which flowing through the LCL filter inductors are sensed and then the weighted average value of these currents are used in the feedback control loop to the PR controller. In this way the overall control system can be treated as a first-order system instead of third-order so that ensuring the stability of the system will be easier. It has been also demonstrated that large values of proportional and resonant gains can be selected to increase the bandwidth of the system. This is particularly important for the implementation of HCs, as more frequencies can be added which is not the case for the standard feedback topology. Consequently, minimum levels of current THD can be achieved. In fact, it

has been proven in previous work [64], [61] that the adoption of higher resonant gains leads to very fast current reference tracking. However, this is achieved at the cost of a considerably longer transient response in the case of disturbances [65]. Meanwhile another study has proposed a detailed systematic design process for an optimum selection of the HCs parameters [66]. The design process in the study has considered important factors that include grid synchronisation and transient response.

2.5.1 Adaptive PR controllers

Although the PR controllers have been successfully implemented in grid-connected inverter systems due to their advantages, their performance might be decline due to changes in operation conditions of the distribution system. In fact, the typical distribution network is well-known of its related unavoidable disturbances and uncertainties that can challenge the control and stability of grid-connected inverter systems. The time-varying grid operating conditions include: grid voltage distortion, grid frequency deviation and grid impedance variation. If these conditions have not been considered in the design of such systems, the control function will be degraded leading to negative impacts on power quality. The effect of grid operating conditions on the current controller performance of grid-connected PV inverter systems has been investigated in [67]. It has been shown in the investigation that the performance of the current controller is sensitive to these conditions because they are varying continuously and in this case the optimum performance of a fixed tuned system cannot be ensured for long period of time. The conclusion drawn from this investigation proved that grid impedance variation and distorted grid voltage can result in large increases in current THD where the power quality standards can be exceeded. Hence, most of recent researches are focusing on enhancing the performance of the control system taking into account these variations.

Frequency-adaptive PR controllers are also a subject for several researches in the literature [68], [69], [70], which are primarily focused on enhancing the PLL algorithm and applying its frequency to the current controller. The most recent study presented in [71], argued that since the conventional PR controllers are tuned at pre-set frequencies in their internal model, then instantaneous tracking capability for ac signals cannot be ensured during grid frequency disturbances. To address this issue the author proposed a solution based on tuning the controller parameters for

synchronisation of the grid-connected inverter. The proposed method entitles a frequency locked loop (FLL) mechanism that consist of a perturbation algorithm and a resonant adaptive filter. The FLL function is to provide the PR controller with estimated grid frequency. In this way the resonant frequency of the PR controller will follow the grid frequency variation. The included experimental results demonstrate the proposed adaptive scheme is effective in extracting the grid frequency during disturbances. Moreover, adapting the PR controller in this way makes the injected grid current immune to high-order grid harmonic disturbances.

In a similar approach [72], a frequency-adaptive PR controller based on the concept of FLL and multi-resonant control structure has been proposed. In this technique the FLL unit was connected to the main resonance controller in order to deliver the estimated grid frequency and adapt the PR controller to any variation in the grid frequency. The included experimental results validated the effectiveness of the proposed control structure which in addition has offered a high harmonic rejection capability and self-synchronisation with grid voltage without the need for a dedicated synchronisation units like the PLL.

Another important factor that can affect the stability and control of grid-connected inverter systems is the variation in grid impedance [73], [55]. The changes in the interfacing grid impedance seen by the inverter can be linked to several reasons include long overloaded cables, saturation, and temperature effects. In fact grid-connected inverter systems are commonly installed in typical weak grids with long distribution cables where a large set of grid impedance is presented. The inductance of this impedance will interact with the inductance of the low-pass filter resulting in a decrease in the bandwidth of the current controller as depicted in Figure 2-5.

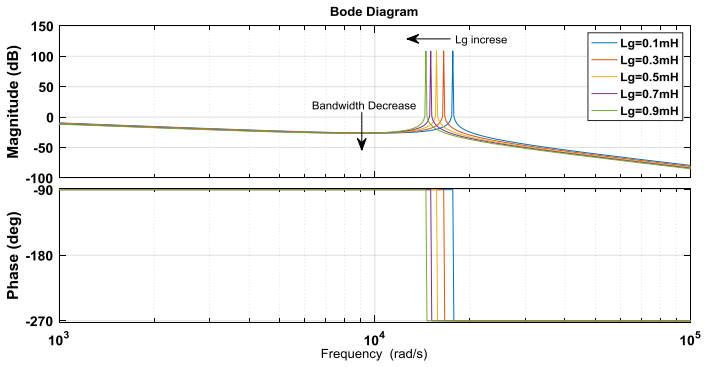

Figure 2-5 effects of gird impedance variation on resonant frequency

From this prospective more emphasise has been given to propose an advanced control scheme in order to mitigate of such variations in the grid impedance.

An innovative and effective control scheme for grid-connected converter with LCL filter has been proposed in [74], where the impact of grid impedance variation are considered. The proposed control scheme is based on a PR controller with the use of voltage signal of filter capacitor as feedforward signal in its structure. It also utilizes an opportune filter to process the feedforward signal to eliminate the resonance effects associated with LCL filter. The LCL filters have a particular resonant peak which can be excited by the change in grid impedance values. The study is supported by a detailed mathematical analysis and the proposed control scheme is validated by experimental results which showed that the impact of grid impedance variation on the performance of the system has been reduced and the resonance effects of the LCL filter have been cancelled. However, the proposed techniques required extra current and voltage sensors which might not be preferred from a cost point of view.

The previous work [75]has proposed an adaptive control scheme that can deal with the diversity in source impedance and solar irradiation based on a self-tuning PR controller. It employs a simple one-dimensional optimization algorithm (ODO) in order to determine an optimum updated control gains for the PR controller for further enhancement of power quality as shown in Figure 2-6.

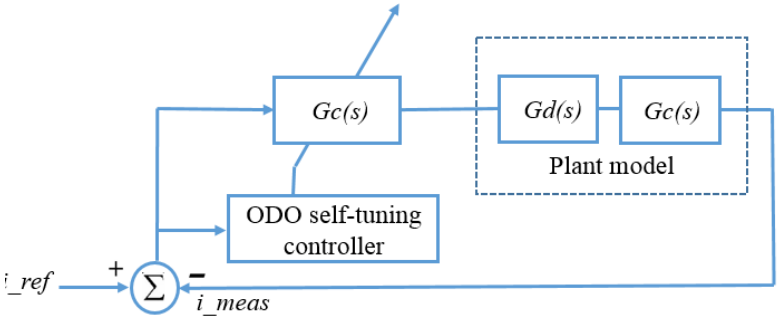

Figure 2-6 Control structure of ODO-based PR controller

.

Another study considered the change in grid impedances in the control scheme based on a PR controller is presented in [76]. The proposed scheme consists of an outer infinite voltage control loop and an inner current control loop. The outer loop exhibited significant gains in the surrounding area of positive and negative sequences components of the fundamental frequency through a simple selection of weighting

function. The included experimental results demonstrated the robustness of the controller against system parameter variation such as load disturbances.

PR controllers were also the subject of a successful advanced control scheme when combining with other control strategies such as repetitive control (RC) [77], [78]. Although the RC controller itself can track or reject all harmonics bellow the Nyquist frequency, it has a much slow dynamic performance compared with that of a PR controller. In the light of this, the work in [34], has developed a new hybrid control strategy that combines the PR+HCs with the RC controllers for a single-phase grid-connected inverter as shown in Figure 2-7. By using this combination the advantages of a fast tracking capability owned by the PR controllers and complete harmonic mitigation of RC controller, high performance control strategy can be ensured under different conditions. According to the included experimental results, the proposed controller achieved a relatively high control accuracy with less complexity in terms of harmonics suppression irrespective of changeable operating conditions.

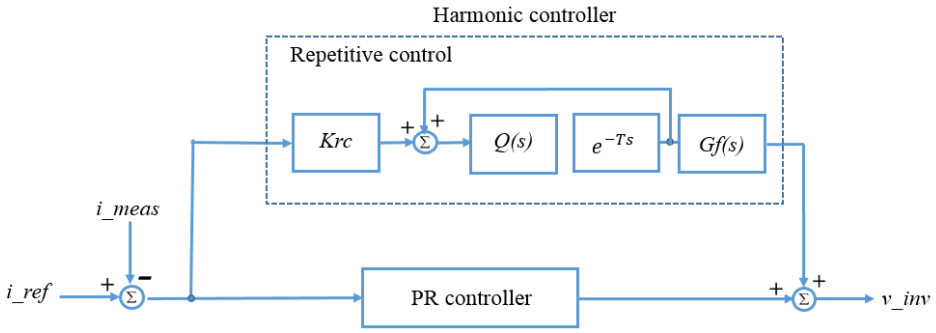

Figure 2-7 PR controller with repetitive-based harmonic controller

2.6 Grid impedance estimation methods

In general, the grid impedance prediction and estimation techniques can be divided into two main categories [79], [80]: invasive methods, where one or more disturbances of harmonic signals are injected into the system in random or periodical way. These disturbances can be in the low frequency rage as reported in previous studies [81], [82] or in the high frequency range as presented in [83] to excite the system response. Based on the system's response, grid impedance can be estimated from current and voltage

measurements. In contrast, non-invasive methods depends on the measured excitation of the natural variations in load to determine the impedance value[84], [85]. Both categories have their own drawbacks which make it difficult to implement in undedicated platform such as PV inverter systems.

For the on-line estimation of the grid impedance, the work in [86] presented a classical Kalman filter based on the inherent disturbances at the PCC and on the utilisation of an observer-based parameters identification. This method suffers from complicated tuning processing. An alternative technique has been proposed in [87] which produces a small perturbation in the form of periodical active and reactive power variations. Other various relevant studies have been published [88-91].

2.7 Chapter summary

This chapter presents the classification of current control strategies for grid-connected PV inverter system. A special attention has been paid for the proportional resonant controller. A literature review on previous research on the PR controller is also provided. Since grid operating condition can affect the performance of current controller, a review on adaptive PR controller is also presented. Finally grid impedance estimation techniques are discussed.

CHAPTER 3

MODELLING AND DESIGN OF SINGLE-PHASE GRID-CONNECTED PV INVERTER

3.1 Introduction

This chapter presents the design and modelling of a 2 kW single-phase PV grid-connected inverter based on MATLAB/Simulink. The design is used throughout the thesis for analysis and detailed studies. In this chapter, the entire model of the voltage source inverter (VSI) with system parameters and description is presented in the first section. The second section presents the design of the LCL low-pass filter and its advantages compared to other low pass L and LC filters. The final section introduces the design of proportional resonant (PR) and proportional integral (PI) controller along with a comparison of their performance. Finally, stability analysis of the system including damping effects, is presented.

3.2 Modelling of single-phase grid-connected PV H-bridge inverter

The modelling and analysis of grid-connected PV inverter systems can be configured using different techniques, generally in the time domain or in the frequency domain. In the time domain, the system can be modelled using linear differential equations with constant coefficients, whereas in the frequency domain a Laplace transform must be derived. Other techniques that can be used include the Z-transform and state space modulation, as reported elsewhere [92]. In this research, the model of the single-phase grid-connected PV inverter is developed via differential equations and a Laplace transform. In this way, the behaviour of the system as well as its responses can be analysed. The typical arrangement of a single-phase grid-connected PV inverter is shown in Figure 3-1. It consists of continuous time current and voltage signals. As can be seen from the figure, the PV model is represented by a DC voltage source, $V_{DC,}$ connected to the H-bridge inverter. The H-bridge inverter is connected to the distribution grid at the point of common coupling (PCC) via a low-pass LCL filter. The distribution generation system (DG) is represented by the grid voltage V_g and grid impedance Z_{Lg}, which is in series with the filter inductor L_2. In addition, the figure

shows current and voltage sensors used to send measurement data to the current controller platform. According to the figure, the modelling of the whole system can be divided into three main parts. First, the pulse width modulation (PWM) is modelled, followed by the low-pass LCL filter along with the series grid impedance, while the final part involves the modelling of the current controller.

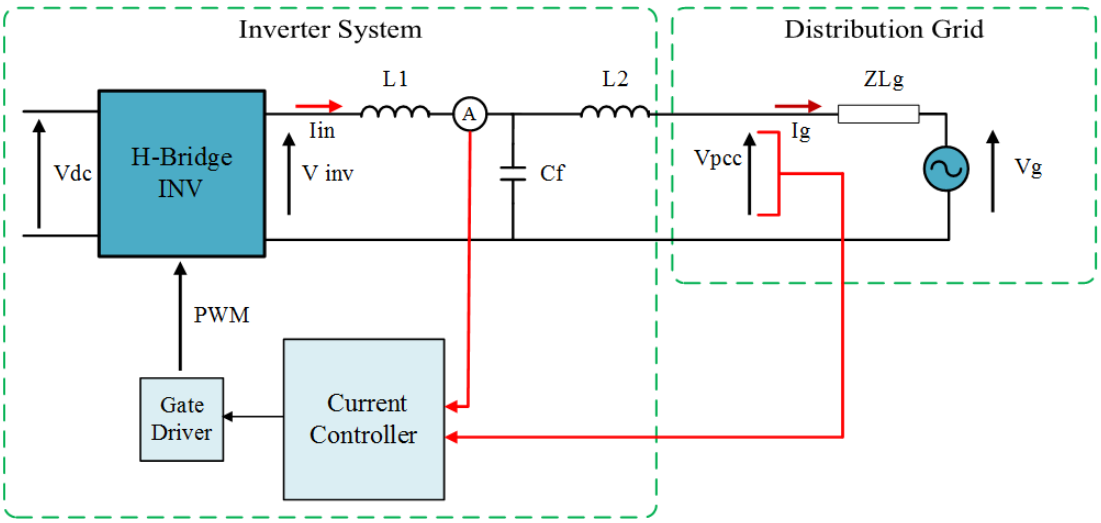

Figure 3-1 Typical circuit diagram of a single-phase grid-connected PV inverter

3.2.1 Modelling of H-bridge and PWM model

Figure 3-2 shows a Simulink model of an H-bridge inverter, which is modelled using four isolated gate bipolar transistors (IGBT). The inverter's task is to convert the DC voltage produced by the PV modules into AC voltage with the help of the PWM technique. PWM is a switching technique used to drive the gates of the inverter. Two well-known methods are widely used in power electronic applications: bipolar PWM and unipolar PWM techniques. A brief description of the differences between the two methods is provided next.

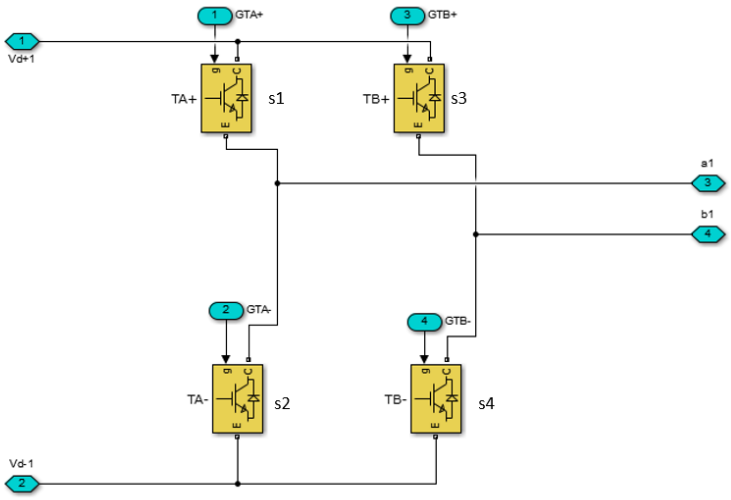

Figure 3-2 IGBT H-bridge inverter

3.2.2 Bipolar PWM

Bipolar PWM works by comparing a single sine waveform as a reference signal with a carrier signal (normally in a rectangular form) to produce the control signal. The inverter switches are turned on and off according to the control signal, which shapes the output voltage waveform in such a way so that the output changes from *+Vdc* where the sinewave is bigger than the carrier signal to *–Vdc* so that sine wave is smaller than the carrier signal, as shown in Figure 3.3.

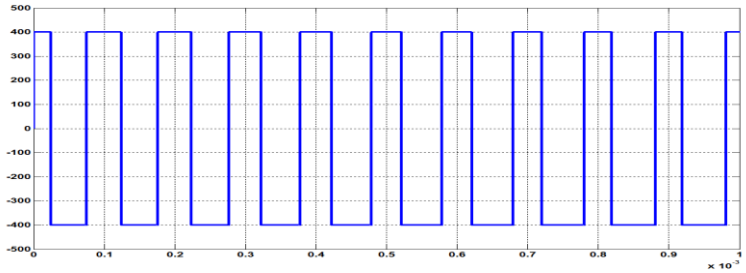

Figure 3-3 Inverter output voltage using bipolar PWM

3.2.3 Unipolar PWM

The unipolar switching scheme involves a comparison of a carrier signal (V_{tri}) with two sinewaves (V_{sin}) shifted from each other by 180 degree as shown in Table.1 and Figure 3-4. The positive comparison of the first sinewave and the triangular carrier

generates the gate signal for switch s_1. On the other hand, the gate signal of switch s_3 is generated from the negative comparison.

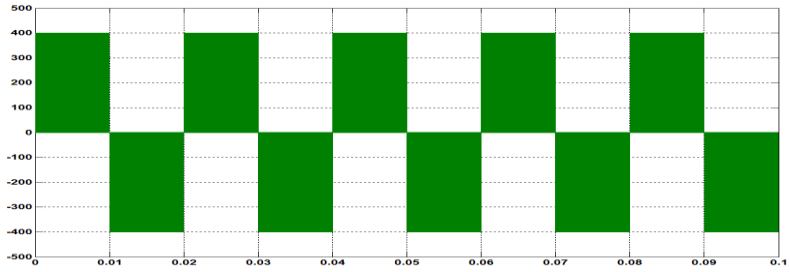

Figure 3-4 Inverter output voltage using unipolar PWM.

The other two switches, s_2 and s_4, have a complementary switching pattern compared to s_1 and s_3 respectively. The ratio of carrier to reference signal determines the output of the inverter, as shown in Figure 3.4. One important advantage of unipolar PWM techniques is that they offer higher efficiency and higher output power compared with bipolar techniques [93]. In addition, it has been reported in [94] that lower dv/dt stress ratios in the case of unipolar PWM. Moreover, from a cost effectiveness point of view, smaller DC-link capacitor can be employed when unipolar PWM is selected, as the DC voltage ripple is significantly reduced. However, during its operation, electromagnetic interface (EMI) issues can be presented due to the consequences of the high leakage current [29]. Due to the aforementioned advantages, unipolar PWM scheme is used to drive the gates of the H-bridge inverter in this project for both simulation and practical work. The modelling representation for the inverter and the unipolar PWM is given as a unity gain of K_{PWM}=1.

Table 1. Output voltage of the inverter

Signals Comparison	***IGBT Switches***			
	1	*2*	*3*	*4*
Vsin > Vtri	*ON*	*OFF*	*OFF*	*OFF*
Vsin < Vtri	*OFF*	*ON*	*OFF*	*OFF*
-Vsin > Vtri	*OFF*	*OFF*	*ON*	*OFF*
-Vsin < Vtri	*OFF*	*OFF*	*OFF*	*ON*

3.2.4 Modelling of the delay effect

Since the current control scheme is implemented in a digital platform, the effect of the delay time has to be considered. Two kinds of delay are generally exist; the computation and PWM delay. The former is resulted from the time duration from the sampling instance and the updating instant of the modulating reference, while the latter in caused by the effect of the zero-order-hold ZOH which keep the PWM constant once it has been updated [95]. The transfer function that represent the delay effect can be expressed as follow.

$$G_d(s) = \frac{1}{1.5T_s s + 1} \tag{3.1}$$

where T_s is the sampling frequency.

3.3 Design and modelling of the LCL filter and grid impedance

In this section, the design and the modelling of the LCL filter is presented, first the design processes of selecting the parameters of the filter are given then followed by the mathematical model.

3.3.1 Design of the LCL filters

In order to comply with power quality standards, the voltage source inverter (VSI) is interfaced with the utility grid via low-pass filters to filter out the high harmonic components produced by the high switched VSI frequency. The filters are also required to guarantee energy decoupling between the grid voltage and the VSI in order to reduce the dependency on grid parameters such as grid impedance. Moreover, they have to filter the noise associated with differential and common mode switching [96]. Among all of the filtering choices available, LCL filters are preferable because they have a superior filtering performance compared to other L and LC types, as they can provide; a better attenuation of switching harmonics, a lower ripple current stress across the grid-side inductor and a reduced dependency on grid parameters. In addition, dividing the filter inductance between the inverter and grid-side offers a further design flexibility with reduced overall size and cost [97]. However, the use of LCL filter can lead to an instability issues due to the relevant introduced resonance

frequency. To tackle these issues, many active and passive damping solutions have been proposed to be implemented within the system [98], [99], [100],[101]. Passive damping methods use a resistance in series with the filter capacitor, while active methods are accomplished by modifying the control algorithm [102].

An equivalent circuit of the filter taking into account the grid impedance is depicted in Figure 3-5. The grid impedance is represented by a grid inductor L_g and an equivalent series resistance (ESR) R_g, while the LCL filter parameters are represented by an inverter side inductor (L_{in}) in series with an equivalent resistor (R_{L1}), a grid side inductor (L_2) in series with an equivalent resistor (R_{L2}), and a filter capacitor (C_f) in series with a resistor (R_d), which represent the damping and the equivalent series resistance of filter capacitor respectively.

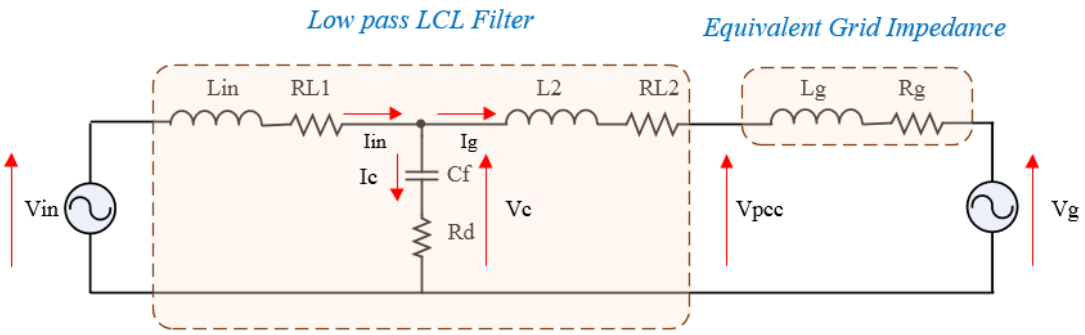

Figure 3-5 Equivalent circuit of the LCL filter impedance and grid impedance

The design process of LCL filter parameters depends on several factors which include the power rating of the system, the line frequency and the switching frequency. In accordance to the step by step design process given in [103], the LCL filter in this project has been designed as follow:

- The inverter-side inductor is selected to limit the current ripple to less than 20%.
- The capacitor value is limited by the power factor variation which should be less than 5% at the rated power.
- The damping solution must be sufficient to avoid instability.
- The resonance frequency should be more than ten times of the line frequency and less than one-half of the switching frequency.

The mathematical equation are as follow:

The base impedance as a function of the grid voltage and the rated power is calculated from equation 3.2.

$$Z_{base} = \frac{V_g^2}{P_0} \tag{3.2}$$

The filter capacitor is then determined for a 5% of maximum power factor variation as:

$$C_f = 0.05 * \frac{1}{\omega_0 Z_{base}} \tag{3.3}$$

The grid-side inductor is selected for a maximum ripple current of 10% and its value is calculated from the next equation:

$$L_1 = \frac{V_{DC}}{6 f_{sw} \Delta I_{rated}} \tag{3.4}$$

Where V_{DC} is the DC-link voltage, ΔI_{rated} is the ripple factor, and f_{sw} is the switching frequency.

The grid-side inductor is a friction of the inverter-side inductor as given in equation 3.5:

$$L_2 = r L_1 \tag{3.5}$$

Where r is a constant that represent the desired ripple attenuation.

After determined the filter components the resulted resonance frequency can be calculated as follow.

$$f_{res} = \frac{1}{2\pi} \sqrt{\frac{L_1 + L_2}{L_1 L_2 C_f}} \tag{3.6}$$

Passive damping solution as a resistor in series with the filter capacitor is adopted due to the simplicity. The value of damping resistance is given in equation 3.7 in accordance to the resonance frequency as follow.

$$R_d = 0.05 * \frac{1}{3\omega_{res} C_f} \tag{3.7}$$

3.3.2 Modelling of the LCL filter and grid impedance

The LCL filter and grid impedance can be modelled based on the relationship between the currents and voltages in the time domain by means of differential equations. The time domain relationship between the voltage across the inverter side inductor (V_{in}) and the inverter output current (I_{in}) can be expressed as follows:

$$V_{in}(t) - V_c(t) = L_1 \frac{dI_{in}(t)}{dT} + RL_1 I_{in}(t) \tag{3.8}$$

The same approach can be applied to the grid-side inductor and filter capacitor, yielding equations 3.9 and 3.10, respectively.

$$V_c(t) - V_g(t) = L_{gT} \frac{dI_g(t)}{dT} + RL_{gT} I_g(t) \tag{3.9}$$

Note that L_{gT} and R_{gT} are the series equivalent impedance of the grid side inductor of the inverter and the grid impedance, respectively.

$$V_c(t) = I_c R_{Cf} + \frac{1}{C_f} \int I_c \, dt \tag{3.10}$$

The frequency domain representation using the Laplace transform for equations 3.8 to 3.10 is given in equations from 3.11 to 3.13:

$$H_{L1}(s) = \frac{I_{in}(s)}{V_{in}(s) - V_c(s)} = \frac{1}{sL_1 + R_{L1}} = Y_{in}(s) \tag{3.11}$$

$$H_{Lg}(s) = \frac{I_g(s)}{V_{in}(s) - V_g(s)} = \frac{1}{sL_{gT} + R_{gT}} = Y_g(s) \tag{3.12}$$

$$H_{Cf}(s) = \frac{V_c(s)}{I_{in}(s) - I_g(s)} = \frac{1}{sC_f} + Rd = Z_c(s) \tag{3.13}$$

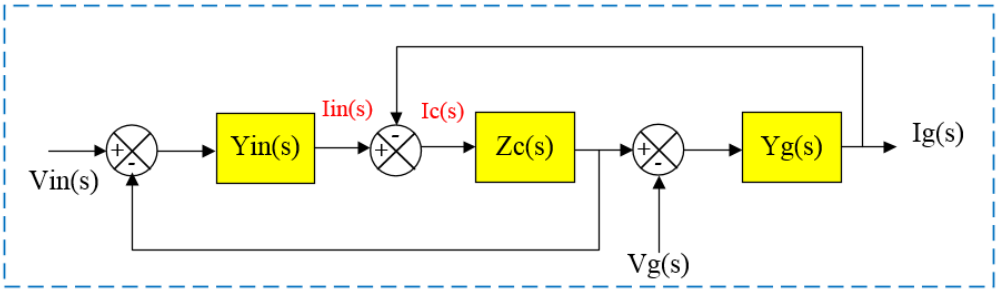

Figure 3-6 Block diagram of the LCL filter transfer function

Figure 3-7 shows the three possible transfer functions of the LCL filter's components; namely the transfer function of the inverter-side inductor ($H_{L1}(s)$), the grid-side inductor (including the grid impedance) ($H_{Lg}(s)$), and the inverter capacitor ($H_{Cf}(s)$). A single Laplace transfer function can be derived by combining the aforementioned three transfer functions to represent the output/input characteristics of the whole system, as given by equation 3.14

$$H_{LCL}(s) = \frac{C_f R_d S + 1}{L_{in}L_{gT}C_f s^3 + [L_{gT}(R_d + R_{L1})L_{in}(R_d + R_{L1})]C_f s^2 + [L_{in} + L_{gT} + C_f(R_{L2}R_d + R_{LgT}R_d + R_{L1}R_{LgT})s + (R_{L1} + R_{LgT})} \tag{3.14}$$

Equation 3.8 can be further simplified by neglecting the effects of the equivalent series resistances, yielding equation 3.15:

$$H_{LCL}(s) = \frac{C_f R_d S + 1}{L_{in}L_{gT}C_f s^3 + (L_{gT} + L_{in})R_d C_f s^2 + (L_{in} + L_{gT})s} \tag{3.15}$$

The Bode plots of the LCL filter are shown in Figure 3-8. There are two interesting features; namely, the fundamental at the low frequency range, and the resonance frequency at the high frequency range. The figure also illustrates the features of the third order transfer function, where the slope is equal to -60dB per decade.

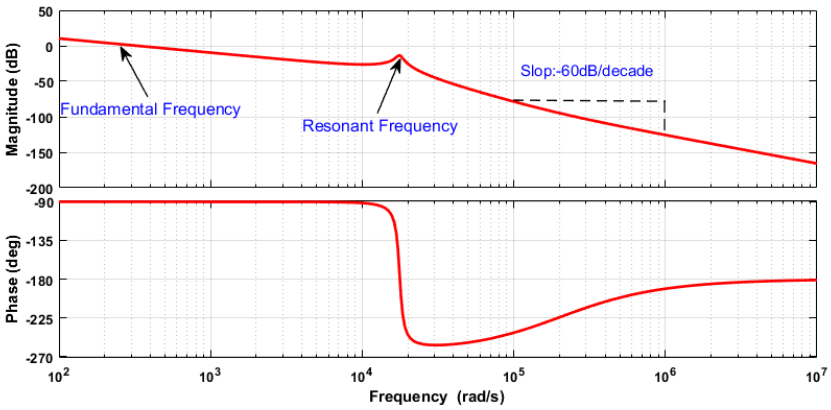

Figure 3-7 Bode plots of the designed LCL filter, L_1=2.12 mH, L_2=0.45 mH, C_f=2.35 µF.

3.4 Modelling of the current controllers

Two types of current controllers are separately implemented for the regulation of the injected grid current which are the PR and the PI controller. The modelling of both controllers is discussed as follow.

3.4.1 Modelling of the PR controller

The current regulation scheme in this research is based on a proportional resonant (PR) controller. The general formula of the Laplace transfer function of an ideal PR controller is given in equation 3.16 below, where K_P and K_R are the proportional and resonant gains respectively, h is the harmonic order, n is the upper limit of the harmonic order, and ω_{hn} is the resonant angular frequency which is set to the nominal fundamental frequency [104-106]. The block diagram of the PR controller is depicted in Figure 3-9.

$$G_{PR}(s) = \frac{m_c(s)}{\varepsilon(s)} = K_P + \sum_{n=1}^{n} \frac{2K_{Rh}s}{s^2 + \omega_{hn}^2} \tag{3.16}$$

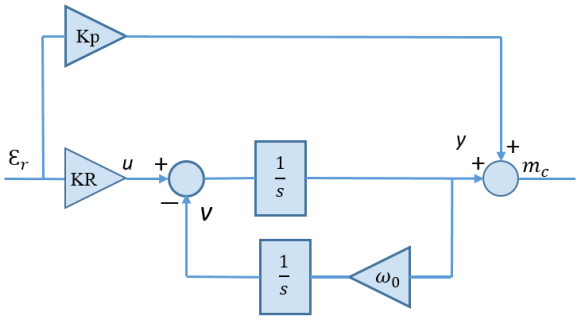

Figure 3-8 Block diagram of the PR controller

For the resonant controller to be set at the fundamental frequency, equation 3.16 can be re-written as follows:

$$G_{PR}(s) = K_P + \frac{2K_R s}{s^2 + \omega_0^2} \tag{3.17}$$

where ω_0 is the operational frequency (*f=50Hz)*. Furthermore, equation 3.17 can be re-arranged to give:

$$G_{PR}(s) = \frac{K_P s^2 + 2K_R s + K_P\,\omega_0^2}{s^2 + \omega_0^2} \tag{3.18}$$

The PR controller given by equation 3.17 acts as a generalized PI controller which is composed of a second order band-pass filter tuned at the desirable frequency [62]. The transfer function can be derived from the synchronous reference frame PI controller as explained in [10]. Transforming this frame into the stationary reference frame means that the DC compensation network is transformed into an AC network, providing an infinite gain at the resonant frequency and an infinite quality factor, as shown in Figure.3-9. For the remaining frequencies, there is almost no gain outside the controller bandwidth [107],[108]. As a result, the steady state error is forced to zero at the resonant frequency, allowing the perfect tracking behaviour for AC signals. The ideal PR controller defined in equation 3.17 acts as a network with an infinite quality factor. In practice, an ideal controller is difficult to implement because the infinite quality factor cannot be achieved in either analogue or digital implementation [104], [109].

The non-ideal PR controller has been introduced in previous studies [10], [18]. The Laplace transfer function of the non-ideal PR controller is given by:

$$G_{PR}(s) = K_P + \frac{2\omega_c K_R s}{s^2 + 2\omega_c s + \omega_0^2} \tag{3.19}$$

In this case the gain of the controller is not infinite, but is still high enough to eliminate the steady-state error. A comparison has been carried out between the ideal and non-ideal PR controllers using MATLAB/Simulink, as shown in Figure 3-9. As can be seen from the open loop Bode plot, the gain of the non-ideal PR controller is not infinite but is significantly high, providing superior control action in the elimination of steady-state error. The figure also illustrates that the cut-off frequency introduced ω_c, widens the controller's bandwidth, offering a better rejection of disturbances in terms of variations in grid frequency [110].

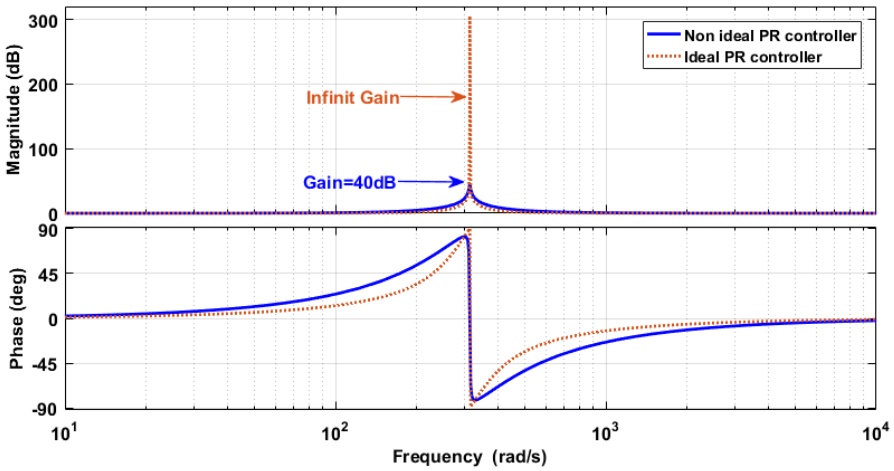

Figure 3-9 Simulation-based comparison of the frequency responses of the ideal and non-ideal PR controller, with Kp = 1, KR = 100, and ω_c= 5 rad/sec

3.4.2 Parameter selection criteria for the PR controller

In this section, the effect of manipulating the parameters of the PR controller on the controller's behaviour are discussed with the aid of MATLAB simulations. At first, the effect of the proportional part (K_P=1) and the introduced cut-off frequency (ω_c = 5) are fixed while varying the resonant part (K_R). It was proven in MATLAB that the variations of K_R have a significant impact on the controller's gain, but no effect

on the bandwidth of the controller. As can be seen from Figure 3-10, the magnitude of the controller gain increases by adding the resonant part.

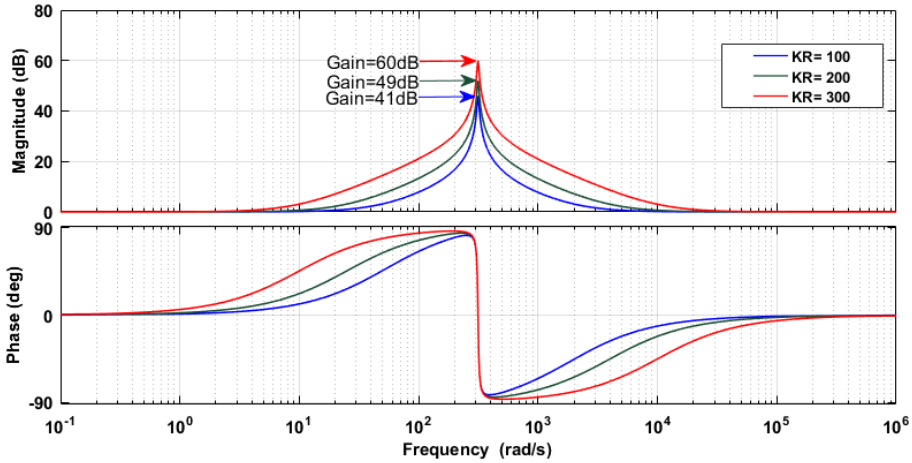

Figure 3-10 Frequency response of the PR controller with varied K_R and fixed KP =1 and ω_c = 5rad/sec

Secondly, by neglecting the proportional action again and fixing K_R=1, the effect of changing the cut-off frequency, ω_c, can be clarified. Figure 3-11 shows that changes in ω_c can affect both the magnitude and phase of the controller. According to the simulation results in Figure 3-11, increments in the phase and the magnitude of the controller occurs as ω_c increases. Moreover, no change in the controller's gain takes place at the resonant frequency of the PR controller.

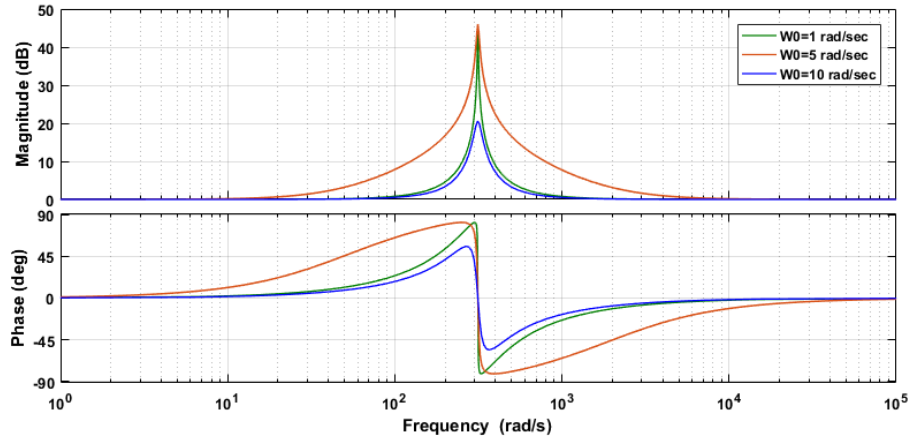

Figure 3-11 Frequency response of the PR controller with a varied ω_c= 5, 10, and 15rad/sec And fixed K_P =1 and K_R =100

Finally, Figure 3-12 illustrates that the presence of the proportional part results in an increase in the magnitude of the controller and a decrease in phase.

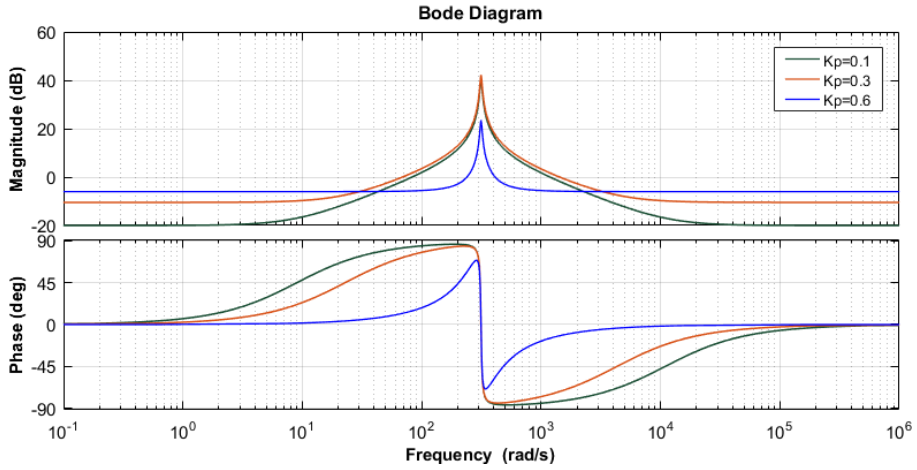

Figure 3-12 Frequency response of the PR controller with varied K_P (0.1, 0.3, and 0.6), and fixed K_R =100 and ω_c =5rad/sec

It can therefore be concluded that the proportional controller, K_P, determines the bandwidth and stability margins of the system, whereas the resonant gain, K_R, eliminates the steady-state error and determines the bandwidth centred at the resonant frequency [108]. Value of the third parameter, ω_c, can be chosen between 5 and 15 (rad/s), which provide good performance in practical [111, 112].

In addition to the elimination of steady state error and of disturbances rejection, one of the most significant advantages of using the PR controller compared to other controllers is the ability of adding selective harmonic compensations (HCs) [62, 66, 113, 114]. The transfer function of the PR controller, including the HCs, is provided in equation 3.20. The new controller structure (PR+HCs) does not affect the dynamics of the system in terms of bandwidth and phase margins. In this equation the harmonics to be compensated for are the third, fifth and seventh:

$$G_{PR+HC}(s) = K_P + \frac{2\omega_c K_R s}{s^2 + 2\omega_c s + \omega_0^2} + \frac{2\omega_c K_R s}{s^2 + 2\omega_c s + \omega_{h_3}^2} + \frac{2\omega_c K_R s}{s^2 + 2\omega_c s + \omega_{h_5}^2} + \frac{2\omega_c K_R s}{s^2 + 2\omega_c s + \omega_{h_7}^2} \quad (3.20)$$

Moreover, the introduced harmonic compensator has a negligible effect on noise and stability, as reported elsewhere [62]. Figure 3-13 below shows the results obtained for the open-loop Bode diagram using MATLAB/Simulink when adding HC that resonates at the 3th, 5th and 7th harmonics.

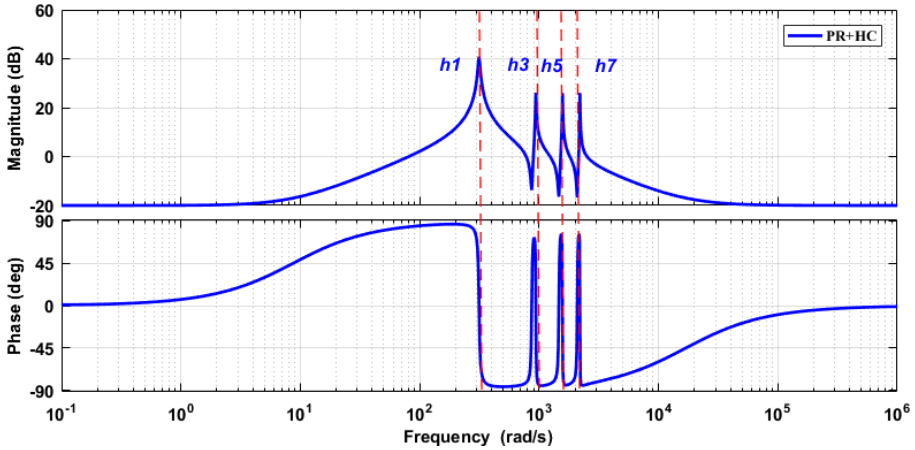

Figure 3-13 Frequency response of the PR controller with harmonic compensators for the 3th, 5th and 7th harmonics

The figure clearly shows that the addition of resonant peaks at the selected frequencies of 150, 250 and 350Hz is an important consideration in the inner control loop. This means that the contribution of these harmonics to the total harmonic distortion is greatly reduced, resulting in an enhancement in power quality as reported in [72].

3.4.3 Modelling of the PI controller

Although a PR controller is used in this research, a PI controller is briefly introduced for comparison purposes. A typical block diagram of a PI controller is shown in Figure 3-14, which consists of a proportional gain, K_P and integral gain, K_i, while (m_c) and (ε_r) are the control and error signals respectively.

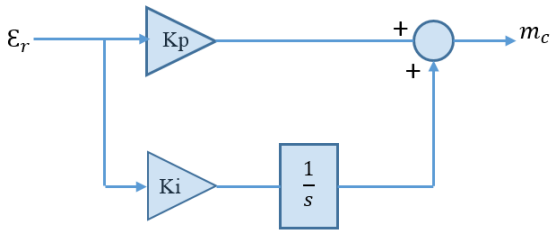

Figure 3-14 Block diagram of a typical PI controller

The Laplace transform of the PI controller is expressed by the transfer function given in equation 3.21 based on its block diagram:

$$G_{PI}(s) = \frac{m_c(s)}{\varepsilon_r(s)} = K_P + \frac{K_i}{s} = \frac{K_P\, s + K_i}{s} \tag{3.21}$$

The frequency response of the PI controller can be obtained by investigating the open-loop Bode plot given in Figure 3-15 below.

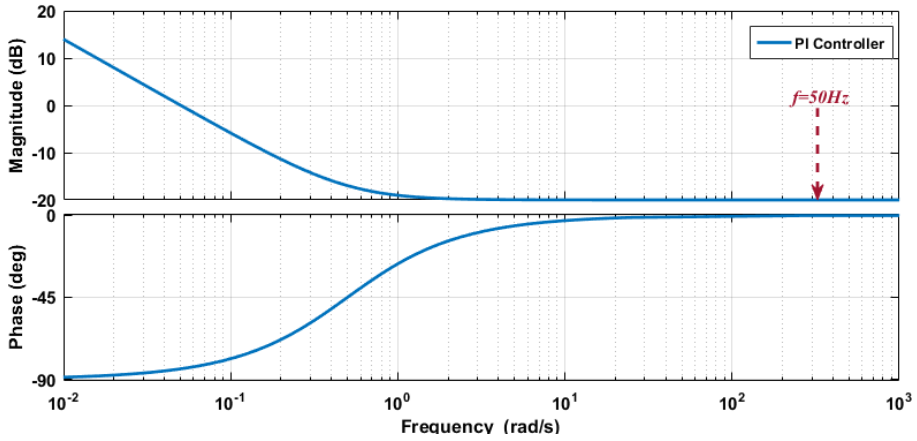

Figure 3-15 Frequency response of the PI controller KP=0.1 and Ki=0.05

A comparison of the PR and PI controllers have been carried out in regards to their frequency response and based on their mathematical models developed in MATLAB. Figure 3-16 shows that the open-loop Bode diagrams clearly illustrate that the PI controller resembles a low-pass filter with a flat response at higher frequencies. Hence, the harmonic rejection at the frequencies of interest, as well as the elimination of steady-state error, cannot be guaranteed. On the other hand, the PR controller acts with similar behaviour to that of a band-pass filter, with a central frequency identical to the frequency of interest. Moreover, the diagram also shows that the PR controller maintains its stability.

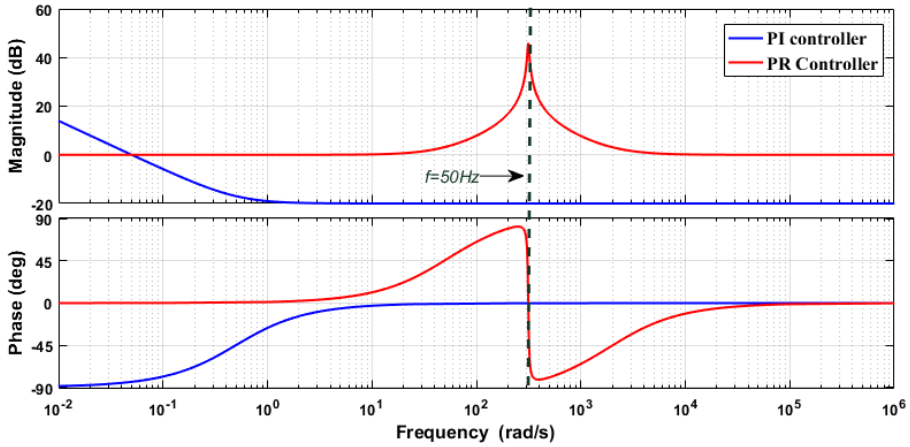

Figure 3-16 Open-loop Bode diagrams of the PR and PI controllers.

3.5 Stability analysis of the modelled system

Different scenarios must be considered in terms of circuit configuration when performing an analysis of the stability of a grid-connected inverter. The filter pattern and associated adopted damping techniques (typically passive or active) are among the factors considered [115]. Another aspect is the position of the sensors which measure currents and voltages. For the voltage sensor, the target is always to track the grid voltage for unity power factor operation; hence, the sensor is placed at the point of common coupling (PCC). On the other hand, the current sensors can be placed either in the grid-side or the inverter-side [116]. In this research, the inverter-side position was selected rather than the grid-side, as the current loop is more closed to the stability [117]. In addition, since the typical grid-side inductor is a fraction of the inverter-side inductor, the system will be more stable if this choice is adopted. The stability analysis of the current control loop is then performed for the designed system. The open- and close-loop transfer functions are derived in the s-domain and then converted into the z-domain. It is worth pointing out that only the AC power stage was considered in the analysis. As such, the dynamics of the DC link capacitor are not included. Moreover, the system's equivalent series resistances that are associated with the system's inductors are neglected, along with the dead time of the PWM inverter. A block diagram of the current control loop is shown in Figure 3-17. It consists of the

transfer functions of: the PR+HC controller, $G_{PR}(s)$, the inverter block which consists of the delay effect $G_d(s)$ and the PWM, KPWM, and the LCL filter, $G_f(s)$.

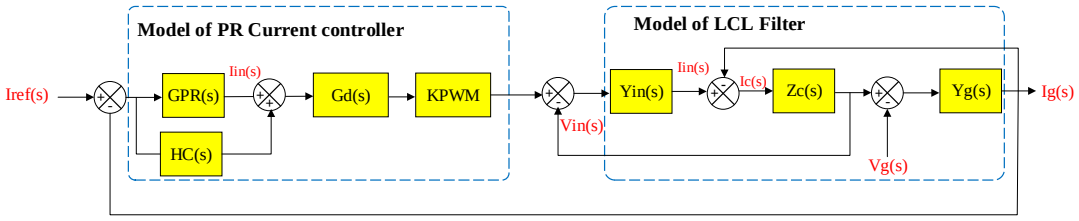

Figure 3-17 Model of the grid–connected inverter system

The measured current is compared to the reference current and the error signal is supplied to the PR+HC controller. The transfer functions of the LCL filter and the controller have been given earlier in equations 3.15 and 3.19 respectively. The inverter model consists of the VSI represented by K_{PWM} and the sampling time delay transfer function $G_d(s)$.

Considering the block diagram shown in Figure 3-17, the relationship between the input and output currents can be expressed as:

$$I_g = H_1(s) + H_2(s) \tag{3.22}$$

where $H_1(s)$ is the relationship between the reference and measured grid current, and $H_2(s)$ is the relationship between the grid current and voltage.

$$H_1(s) = \frac{I_g(s)}{I_{ref}(s)} = \frac{G_{PR}(s)G_d(s)K_{PWM}G_f(s)}{1 + G_{PR}(s)G_d(s)G_f(s)} \tag{3.23}$$

For simplicity, the dynamics of the inverter (K_{PWM}) can be represented by a unity gain, as the switching frequency is relatively high.

$$H_2(s) = \frac{I_g(s)}{V_g(s)} = \frac{G_f(s)}{1 + G_{PR}(s)G_d(s)G_f(s)} \tag{3.24}$$

The second term in equation 3.22 can be eliminated in steady state analysis since a PR controller is employed. It has been shown that a PR controller introduces an infinite

gain at the resonant frequency, and thus the first term $H_1(s)$ approaches the current reference, while $H_2(s)$ approaches zero, which cannot be the case if a PI controller is used.

The open and closed-loop transfer functions of the VSI current control loop can be expressed by equations 3.25 and 3.26, respectively.

$$G_{OL}(s) = \frac{I_g(s)}{I_{ref}(s)} = G_{PR}(s)G_d(s)G_f(s) \tag{3.25}$$

$$G_{CL}(s) = \frac{I_g(s)}{I_{ref}(s)} = \frac{G_{PR}(s)G_d(s)G_f(s)}{1 + G_{PR}(s)G_d(s)G_f(s)} \tag{3.26}$$

$$G_{CL}(s) = \frac{I_g(s)}{I_{ref}(s)} = \frac{K_P R_d C_f s^3 + \left[K_P + 2(K_P + K_R)\omega_c C_f R_d\right]s^2 + \left[2(K_P + K_R)\omega_c + K_P C_f R_d \omega_0^2\right]s + K_P\omega_0^2}{D_5 s^5 + D_4 s^4 + D_3 s^3 + D_2 s^2} \tag{3.27}$$

$$D_5 = L_{in}L_g C_f \tag{3.28}$$

$$D_4 = (L_{in}+L_g)C_f R_d + 2L_{in}L_g C_f \omega_c \tag{3.29}$$

$$D_3 = (L_{in}+L_g)\left(1 + 2\omega_c C_f R_d\right) + L_{in}L_g C_f \omega_0^2 + K_P C_f R_d \tag{3.30}$$

$$D_2 = (L_{in}+L_g)\left(2\omega_c + C_f R_d \omega_0^2\right) + K_P + 2(K_P + K_R)\, C_f R_d \omega_c \tag{3.31}$$

$$D_1 = (L_{in}+L_g)\omega_0^2 + K_P C_f R_d \omega_0^2 + 2(K_P + K_R)\, \omega_c \tag{3.32}$$

$$D_1 = K_P \omega_0^2 \tag{3.33}$$

In order to perform the stability analysis, a MATLAB code was developed for all possible transfer functions in the *s*- and *z*-domains. The development of the stability analysis starts by examining the loop gain of the open loop transfer function $G_{OL}(s)$ given in equation 3.25. Figure 3-18 shows the Bode diagram of $G_{OL}(s)$ with and without the damping resistance. According to the figure, there are five resonant peaks in the frequency response, four of which occur in the low frequency range and are

caused by the PR+HC controller, and the other occurs at the high frequency range due to the LCL resonance. The former peaks serve to eliminate the steady state error, while the latter peak denoted by red dashes is not preferable as it can lead to instabilities if not properly treated.

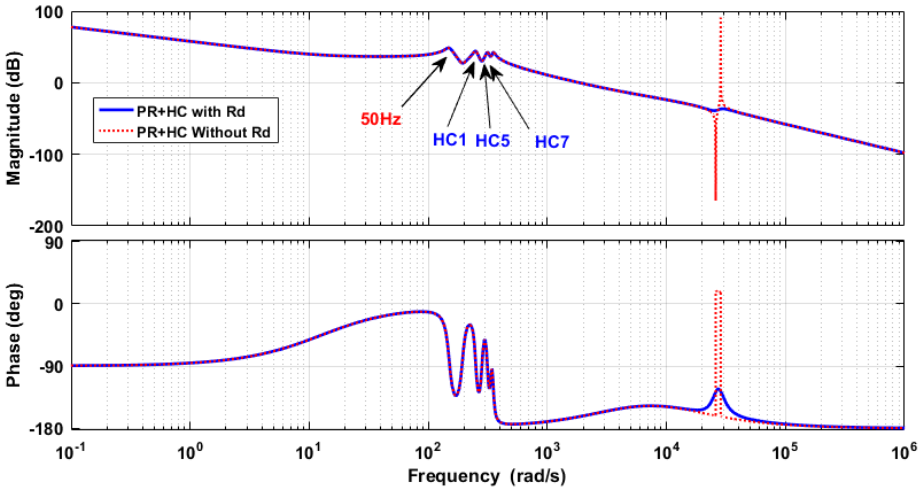

Figure 3-18 Bode diagram of the open loop transfer function with and without Rd under PR controller K_P=2, K_R=100W, and ωc =5

Two damping methods, passive and active can be utilized to eliminate the resonance peak of the LCL filter [101, 118-120], and both techniques ensure stable operation and improve overall system performance.

The stability analysis of the closed-loop transfer function is performed by converting the closed-loop transfer function given in equation 3.27 to its discrete form. This can be accomplished in MATLAB using the 'c2z' function. However, special attention must be given to the discretization method selected in order to avoid mismatching the in frequency response [64]. Examples of discretization methods includes Zero order hold (ZOH), forward Euler, back Euler, Tustin bilinear and impulse invariant. Among these, the Tustin approximation is found to produce a good match between the continuous and discrete models in terms of frequency response. The Tustin discretization formula is given by:

$$G_{CL}(z) = G_{OL}(s)_{s=\frac{z-1}{z+1}\frac{2}{T_s}} \tag{3.29}$$

Figure 3-19 shows the pole-zero plot of the closed-loop discrete transfer function for the designed VSI system. In the figure, there is a pair of complex poles close to the

boundary of the unit circle, a pair of complex poles inside the unit circle, and another pole inside the circle. It can thus be concluded that the designed 2 kW system is stable.

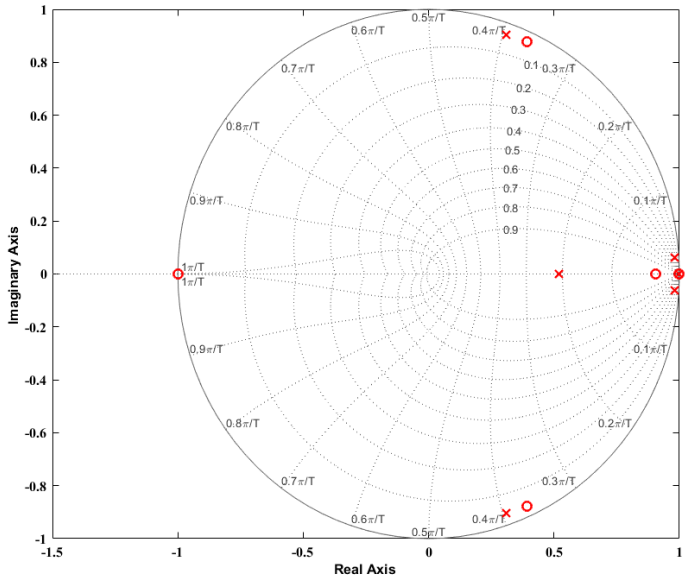

Figure 3-19 Pole-zero map for the current control loop with a passively damped LCL filter

3.6 Chapter summary

This chapter presented mathematical models for the single-phase PV grid inverter system. The modelling of the LCL filter with grid impedance was first developed, after which the models of the PI and PR controllers were provided. For the PR controller, the continues-time domain closed-loop transfer function of the current control loop was derived and then converted into the discrete-time domain. Furthermore, the stability analysis of the VSI system was performed in the z-plane. The findings of the chapter are summarised below:

- The use of a PR controller in single-phase PV grid-connected inverter systems is better than the use of a PI controller in terms of the elimination of steady state error and the minimisation of THD.
- The use of HC with the PR controller can enhance the power quality in terms of THD by compensating for the low-order harmonics.
- The stability of the system can be negatively affected if the system is not probably damped.

- The stability analysis in the z-plane showed that, when the current sensors were placed on the inverter side, the system was stable for the selected gain values.

CHAPTER 4

INFLUENCE OF VARIABLE GRID OPERATING CONDITIONS

4.1 Introduction

This chapter focuses on the effects of grid operating conditions on the inverter system. In particular, it investigates the influence of the time-variant background grid voltage harmonics, the grid voltage fundamental frequency, and grid impedance. To carry out the investigation, the first part of this chapter presents the design of a Simulink model of a single-phase grid-connected PV inverter, including the background harmonic grid voltage and the LCL filter. The digital implementation of the PR controller is also presented. The second part of the chapter discusses the interaction between the grid-connected PV inverter and the distribution network. The influence of background grid voltage with non-ideal conditions is then considered, along with the effects of variations in grid impedance. Finally, the impact of grid frequency variations is presented.

4.2 Simulation of a single-phase PV grid-connected inverter system

The model of a VSI connected to DG was developed using MATLAB/Simulink's library of the Sim Power System for the power electronics blocks and Simulink's library for the control elements. The PV source was modelled with a 400V DC source, as this is the minimum desirable value for a single-phase two-wire 240V 50Hz supply. The VSI was set to a two-leg H-bridge inverter with IGBT/diode switches. The grid model was simulated using a harmonic model of the background grid voltage based on real data, with a total harmonic distortion (THD) of 2.47%. The grid impedance was modelled with a tapped inductor and its values is selected according to IEC60725 standards [121], where the UK residential consumer complex supply impedance for a single phase connection at 50 Hz can vary up to an 0.8mH in the worst-case scenario of a weak grid. The VSI was interfaced to the grid model via a passively damped low-

pass filter LCL. A zero-order hold block was used in the Simulink model for the current and voltage measurement in order to emulate the sample and hold in real-time applications.

To track the frequency and phase angle of the grid voltage signal, a phase locked loop (PLL)-based algorithm was implemented in the Simulink model of the VSI as the synchronising technique. Finally, the PR and PI controllers were modelled with a gain block for the proportional term and a user-defined function for the integral term. The Simulink model of the whole system in depicted in Figure 4-1, while its parameters and variables are presented in Table 2.

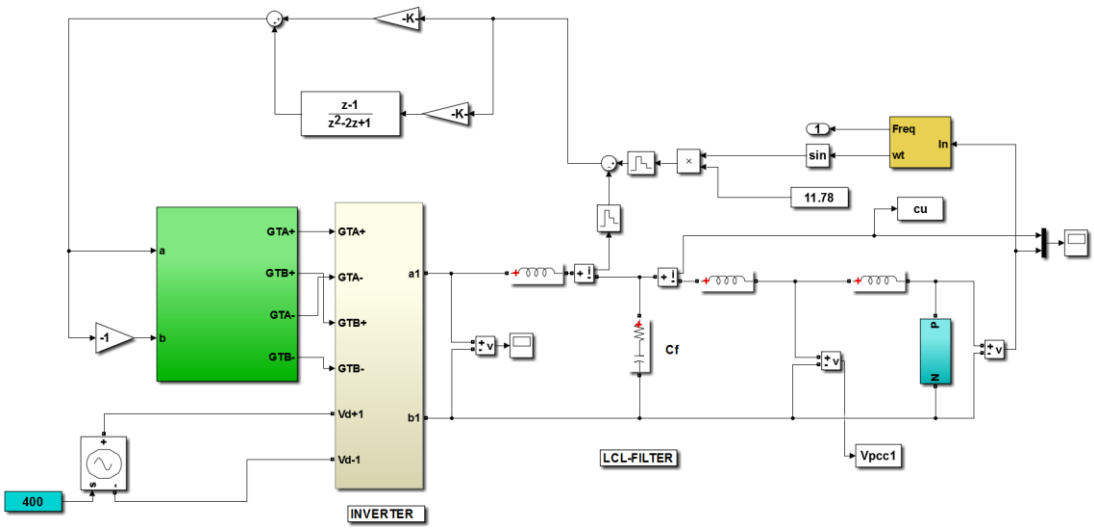

Figure 4-1 Simulink model of the single phase grid-connected system

As can be seen from the figure, the PV source is represented by a 400V DC source interfaced to the grid by an LCL filter. The grid is represented by a non-ideal voltage source as explained in the next sub-title, in series with grid inductance, while the current regulator is represented with the discrete form of the PR controller.

Table 2 Parameters and variables of the VSI

Parameters		
Abbreviation	***Nomenclature***	***Value***
P_n	*Nominal Rated Power*	*2kW*
V_{DC}	*DC link Voltage*	*400V*
V_g	*Grid Voltage*	*230V*
I_{ref}	*Reference Current*	*8.3A (RMS)*
L_1	*Inverter Side Inductor*	*2.12mH*
L_2	*Grid Side Inductor*	*0.45mH*
C_f	*Filter Capacitor*	*3.53 μF*
R_d	*Damping Resistance*	*3.2 Ω*
f_{res}	*Resonant Frequency*	*4.5 kHz*

4.2.1 Simulink model of a non-ideal grid voltage

In order to investigate the interaction between the low voltage distribution network and the grid inverter's output current, a design of a non-ideal grid was implemented in MATLAB/Simulink. The model consists of different magnitude and phase angles of up to the 40th harmonic order as the measurement devices of the THD in practical is limited by the number of the harmonic order. The 40th harmonics are summed together to form the desired grid voltage as illustrated in Figure. 4-2.

The design was based on the experimental data available for the research group in the Electrical Power Laboratory at Newcastle University, and is shown in table 3. According to the simulation results, the non-ideal grid voltage is found to have a total harmonic distortion (THD) of 2.45%. It is worth to mention that THD is a merit used to quantify the level of harmonics presented in current or voltage waveforms. The THD can be defined by comparing the harmonic content of a waveform to its fundamental [122].

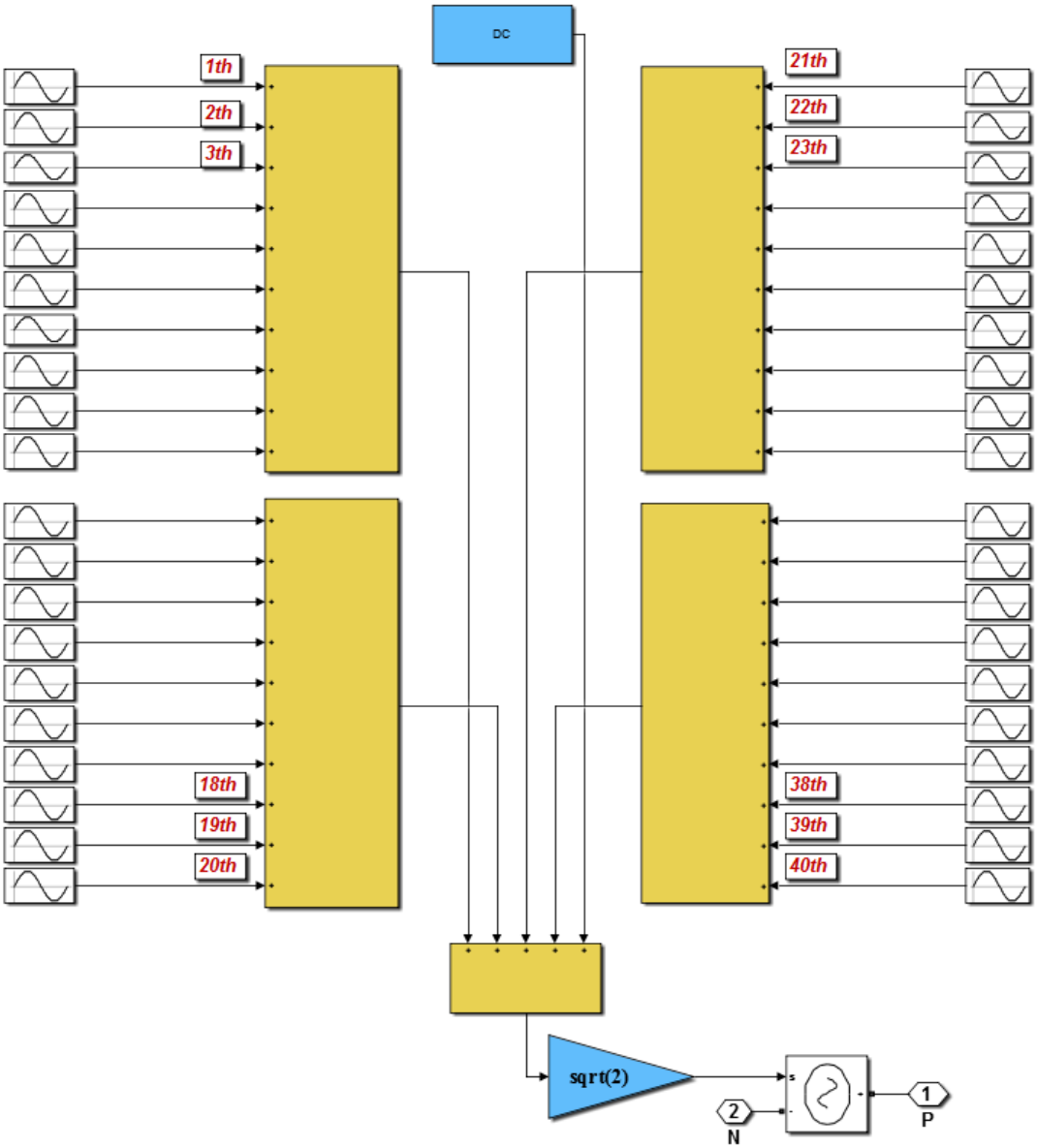

Figure 4-2 Simulink model of a non-ideal grid voltage

Table 3 Harmonics data of the grid voltage signal

Frequency Hz	*Amplitude RMS*	*Phase deg*		*Frequency Hz*	*Amplitude RMS*	*Phase deg*
50	*241.72*	*320.29*		*1050*	*0.05*	*265.06*
100	*0.07*	*340.9*		*1100*	*0.01*	*277.76*
150	*3.56*	*90.01*		*1150*	*0.12*	*281.76*
200	*0.02*	*296.59*		*1200*	*0.01*	*49.23*
250	*3.45*	*98.5*		*1250*	*0.13*	*285.01*
300	*0.01*	*33.74*		*1300*	*0.01*	*151.49*
350	*2.45*	*253.58*		*1350*	*0.15*	*105.57*
400	*0.01*	*33.74*		*1400*	*0.01*	*103.03*
450	*1.09*	*303.98*		*1450*	*0.03*	*295.9*
500	*0.01*	*14.62*		*1500*	*0.01*	*98.5*
550	*0.5*	*91.26*		*1550*	*0.08*	*157.67*
600	*0*	*168.4*		*1600*	*0.01*	*175.79*
650	*1.37*	*13.7*		*1650*	*0.02*	*147.72*
700	*0.01*	*43.99*		*1700*	*0*	*335.9*
750	*0.73*	*313.33*		*1750*	*0.07*	*310.1*
800	*0.01*	*112.09*		*1800*	*0*	*204.46*
850	*0.7*	*350.93*		*1850*	*0.01*	*283.66*
900	*0.01*	*208.84*		*1900*	*0.01*	*20.7*
950	*0.2*	*167.34*		*1950*	*0.02*	*114.62*
1000	*0.01*	*316.74*		*2000*	*0*	*272.65*

4.2.2 Simulink model of the phase locked loop

PLL-based algorithms are widely used in applications that require synchronisation, due to their effectivness, robustness and simplicity [123]. Figure 4-3 shows the Simulink model of the closed-loop feedback control of the PLL, which is composed of three main parts: the phase detector (PD), the loop filter (LF), and the voltage control

oscillator (VCO). The task of the three parts is to ensure synchronisation between the grid voltage and grid current.

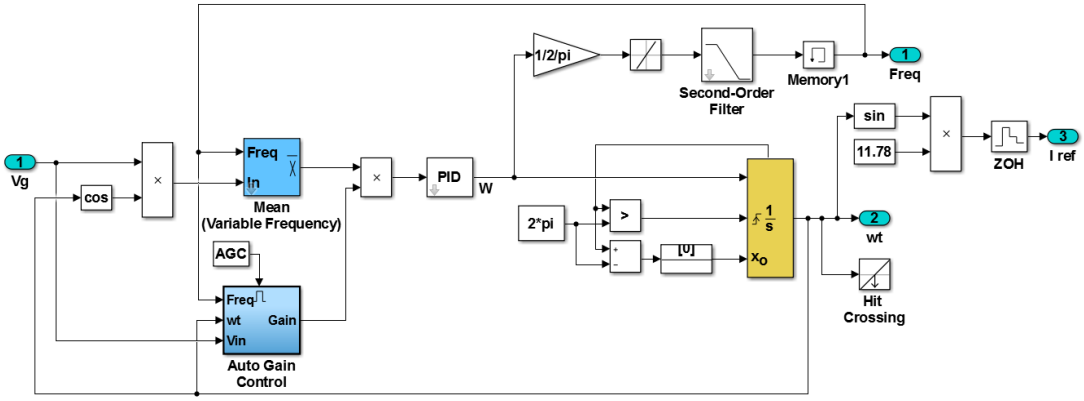

Figure 4-3 Simulink® model of the single phase PLL

4.3 Interactions of the distribution network and grid-connected PV inverter system

In order to improve the functionality of the increasing numbers of PV energy sources, PV grid-connected inverters must be designed in such a way so that they are able to deal with time-varying background grid operating conditions. Advanced grid support functions (GSFs) are increasingly implemented to provide voltage and frequency support at the point of common coupling (PCC). GSFs consist of voltage ride-through (VRT) and frequency ride-through (FRT) [124]. Since the PV system employs power electronic inverters which are controlled by PWM techniques, unwanted interactions arise in areas with high penetration of PV systems. Figure 4-4 shows the equivalent circuit of the VSI connected to the distribution network at the PCC. The VSI is modelled by a current source and the grid voltage by a voltage source, while the grid impedance is modelled by a combination of source and load impedances. The operating conditions of the electrical grid can be affected by the PV inverter systems connected to it in some circumstances. For example, the harmonic currents injected to the utility grid by the PV sources can affect power quality, leading to unwanted islanding , and causing the malfunctioning in the grid-side protection devices [125]. On the other hand, the operating conditions of the utility grid have an impact on the functionality of the power electronic inverter. It has been demonstrated in [126], that the THD of the injected current can experience an increase at the output of the inverter, which has been linked to the oscillation present in the background grid voltage

waveform, especially at low power levels. At high power levels, the total harmonic distortion of the injected current has been found to inversely vary with the level of the delivered power, due to the finite resolution and digitalisation of ADC devices used for measurements [67].

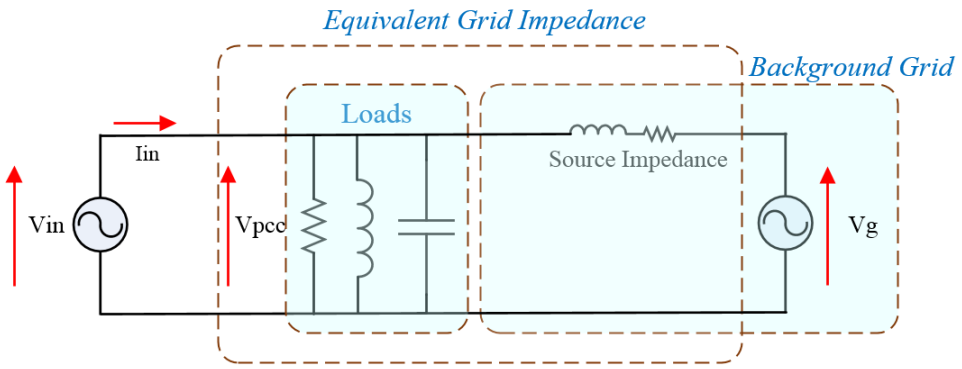

Figure 4-4 Equivalent circuit of the VSI connected to the distribution grid at the PCC

Another important factor at play is the variations in grid impedance, which changes depending on loading conditions. The control scheme of the grid-side PV inverter is strongly dependent on the identification of grid impedance, and it is recommended to measure its value on-line to avoid islanding and instability problems [127]. Moreover, resonance implications can arise due to the interfacing between grid impedance and the inverter's low-pass filter which has a typical frequency characteristic with a pre-designed resonance peak. The next sections investigate the influence of a distorted grid voltage on the inverter's performance, as well as the influence of grid impedance and frequency variations.

4.3.1 Effect of distorted grid voltage on inverter performance

In order to investigate the influence of distorted grid voltage on the performance of the inverter and on power quality, the designed non-ideal grid voltage presented earlier in section 4.2.1 is used in order to conduct a comparison with the VSI connected to an ideal grid voltage condition.

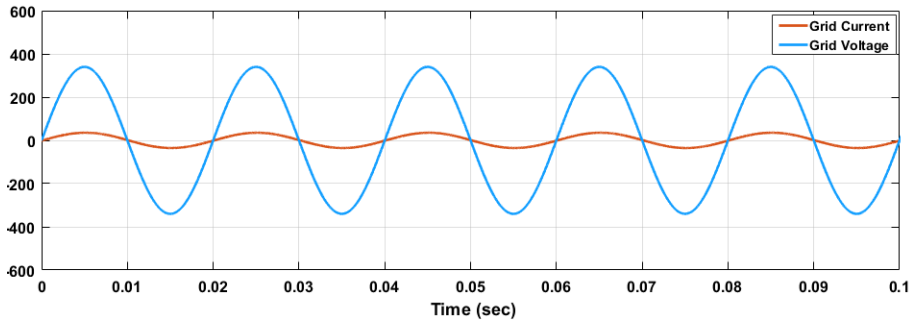

(a)

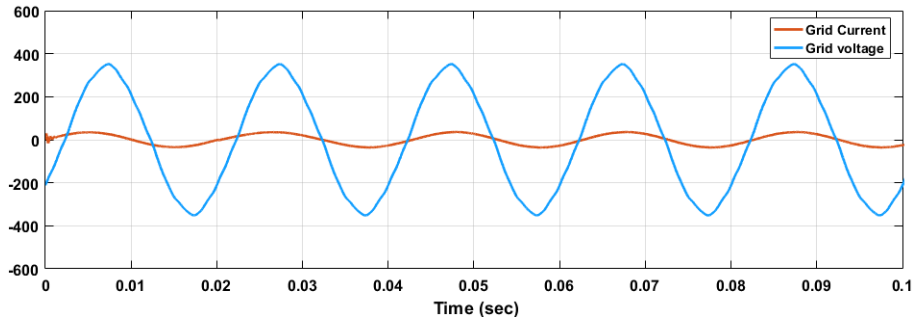

(b)

Figure 4-5 (a) Ideal grid voltage and injected grid current, (b) Distorted grid voltage and injected grid current

Figure 4-5 shows the simulation results of grid voltage and current for ideal and non-ideal grid voltage conditions. As can be noticed, when the system is under the ideal grid condition (THD=0%), the output current is synchronised with the grid voltage without delay. On the other hand, when the non-ideal grid condition is applied (THD=2.47%, Figure 4-6), there is a significant synchronisation delay between the grid voltage and current, as can be observed in Figure 5-4. Both waveforms required just over one cycle before being in phase, although this delay is eliminated in the steady state.

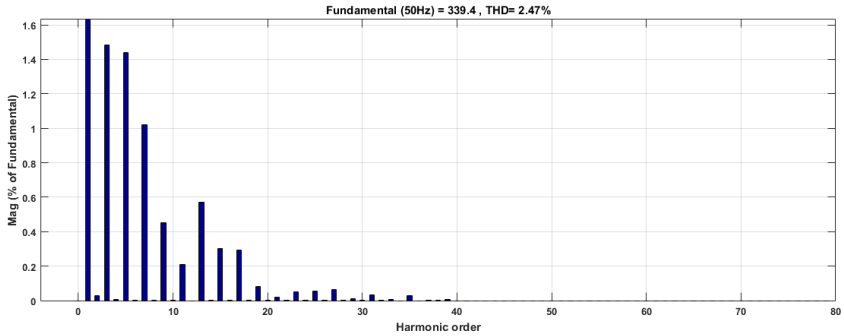

Figure 4-6 Harmonic profile of grid voltage at non-ideal conditions

The different between the PCC and Vg is illustrated in Figure 4-4. The PCC voltage can also be affected by changes in the background voltage waveform. Figure 4-7 shows that the PCC voltage waveform follows the background grid voltage. To assess the sensitivity of the PCC voltage to particular harmonics, the magnitude of the 3^{th}, 5^{th} and 7^{th} harmonics have been changed, and their effects on the PCC voltage have been recorded and are depicted in Figure 4-8.

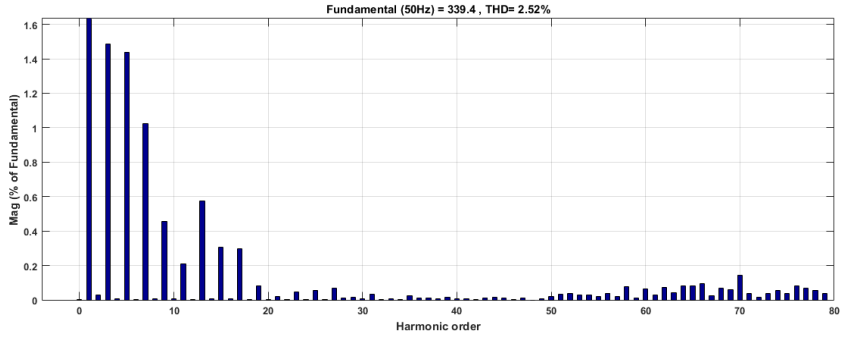

Figure 4-7 Harmonic profile of the PCC voltage at non-ideal grid voltage conditions

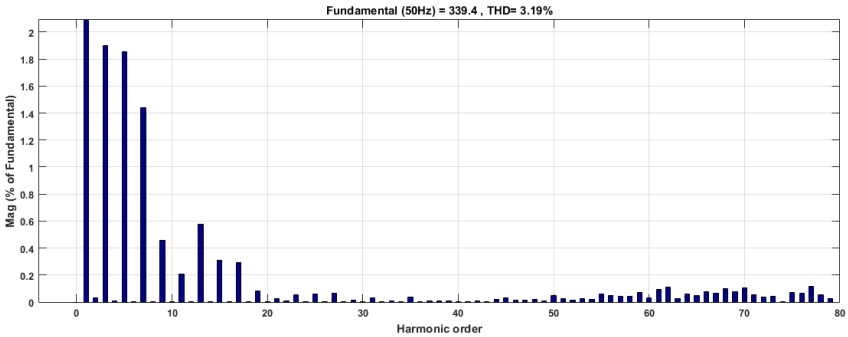

Figure 4-8 Harmonic profile of the PCC voltage under magnitude change of the 3^{th}, 5^{th}, and 7^{th} harmonic orders

It is obvious from the figures that, when the magnitudes of some harmonics in the background grid voltage change, the shape and harmonic profile of the PCC voltage changes accordingly, which means that the higher the distortion in the background grid voltage, the more distortion is present in the PCC voltage.

4.3.2 Effect of grid impedance variation on the VSI system performance

The PCC voltage depends on the stiffness of the utility network, which in turn depends on the influence of several conditions. These conditions can be vary from the loading condition at the PCC (such as the impedance of the electrical devices and the loading capacity), to the impedance of the supply transformers and cables. Hence, low grid impedance (mainly inductor) reflects the stiffness of the grid.

The Simulink model of the VSI system is shown in Figure 4-1, where the LCL filter impedance is coupled to the grid impedance. As such, the interaction between the background grid and the VSI system can be modelled by an LCL impedance, a grid impedance, a grid voltage and a voltage at the output of the inverter as shown in Figure 4-9. Note here that the effect of the control loop is neglected.

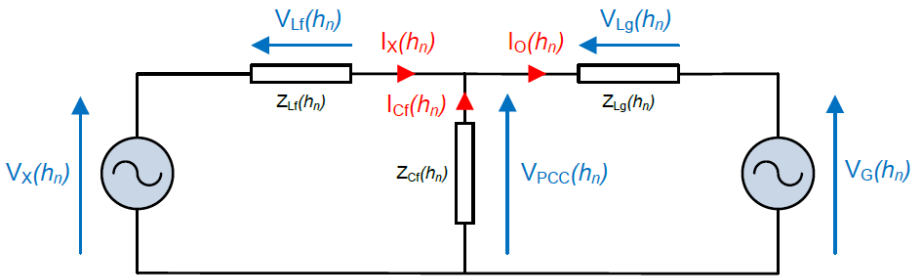

Figure 4-9 Harmonic model of the background grid voltage with the VSI connected at the PCC

Equations 4.1 to 4.3 define the impedance of the filter inductor at the inverter side (Z_{Lf}), the grid impedance (Z_{Lg}) which represents the filter grid-side inductor and the grid impedance and the filter capacitor impedance (Z_{Cf}) at a particular harmonic order respectively.

$$Z_{Lf}(h_n) = R_{Lf} + jX_{Lf}(h_n) \tag{4.1}$$

$$Z_{Lg}(h_n) = R_{Lg} + jX_{Lg}(h_n) \tag{4.2}$$

$$Z_{Cf}(h_n) = R_{Cf} - jX_{Cf}(h_n) \tag{4.3}$$

where R_{Lf} , R_{Lg} and R_{Cf} are the equivalent series resistances of the inverter-side inductor, grid-side inductor and filter capacitor, respectively, and h_n and n are the vectors of the harmonic at the corresponding harmonic order and the harmonic order respectively.

According to the circuit depicted in Figure 4-9, there are two voltage supplies connected to each end of the circuit, which are the grid voltage Vg and the inverter voltage Vin, and both voltages affect the PCC voltage. The PCC voltage (V_{PCC}) can be derived in accordance with the well-known superposition theory, yielding equation 4.4:

$$V_{PCC}(h_n) = \frac{V_{in}(h_n)Z_{Lg}(h_n) + V_g(h_n)Z_{Lf}(h_n)}{Z_{Lf}(h_n) + Z_{Lg}(h_n) + \frac{Z_{Lf}(h_n)Z_{Lg}(h_n)}{Z_{Cf}(h_n)}} \tag{4.4}$$

The PCC voltage given above is determined by a combination of effects: those of the inverter filter impedances and the grid impedance. As such, at lower frequencies, the large value of the capacitor impedance makes the term $\frac{Z_{Lf}(h_n)Z_{Lg}(h_n)}{Z_{Cf}(h_n)}$ much smaller than $Z_{Lf}(h_n) + Z_{Lg}(h_n)$, and in this case, the PCC voltage is only determined by the latter term, leading to a low magnitude of PCC voltage:

$$V_{PCC}(h_n) = \frac{V_{in}(h_n)Z_{Lg}(h_n)}{Z_{Lf}(h_n) + Z_{Lg}(h_n)} \tag{4.4}$$

In contrast, the term $\frac{Z_{Lf}(h_n)Z_{Lg}(h_n)}{Z_{Cf}(h_n)}$ is much larger than the $Z_{Lf}(h_n) + Z_{Lg}(h_n)$ term at high frequencies, and the PCC voltage can be determined as follows:

$$V_{PCC}(h_n) = \frac{V_{in}(h_n)Z_{Lg}(h_n) + V_g(h_n)Z_{Lf}(h_n)}{\frac{Z_{Lf}(h_n)Z_{Lg}(h_n)}{Z_{Cf}(h_n)}} \tag{4.5}$$

The PCC voltage given in equation 4.5 is an approximation used at low frequencies. At stiff grid conditions, the small value of grid inductance L_g means that the effect of two terms $Z_{Lg}(h_n)$ and $V_{in}(h_n)Z_{Lg}(h_n)$ can be neglected, and thus the PCC voltage is determined by the impedance of the inverter-side inductor. In contrast, the case is completely different in weak grid conditions, where the grid inductor competes with the filter inductor. In this case, the PCC voltage is determined by both the inverter-side inductor impedances and the grid-side inductor impedance, including the grid impedance. It can therefore be concluded that the voltage level at the PCC in weak grid conditions is more vulnerable to the impact of the VSI than in stiff grid conditions. As the grid inverter system is interfaced to the grid by the LCL filter, stability problems might arise due to the inherent high frequency peak of the filter resonant frequency [128]. The resonant frequency of a third order LCL filter is given in equation 4.6 below, where the grid-side inductor is added to the time varying-grid inductor in series, as shown in equation 4.7 [105].

$$\omega_{res} = \sqrt{\frac{L_1 + L_2}{L_1 L_2 C_f}} \tag{4.6}$$

$$\omega_{res} = \sqrt{\frac{L_1 + L_2 + L_g}{L_1 (L_2 + L_g) C_f}} \tag{4.7}$$

where ω_{res} is the resonant frequency (rad/sec), L_1 is the inverter-side inductance, L_2 is the grid-side inductance, L_g is the grid inductance, and C_f is the filter capacitance. The large change in the grid impedance (L_g in equation 4.7 poses a challenge in the design of the control system in terms of dynamics and stability at both low frequencies around the fundamental frequency, which is the controller's bandwidth frequency, as well as at high frequencies (around the filter's resonant frequency) [129]. This means that knowledge of the grid impedance is important in controller design, as well as for the safe operation of the grid-connected inverter system. In addition, the voltage at the PCC is distorted due to the change in the grid impedance and the other non-linear loads connected to the PCC [87].

The resonant frequency, which changes according to the grid impedance variation is calculated for a wide range of grid impedance values from 0.1 to 0.8mH in accordance with IEC 60752 standards, and the results are summarised in Table 4.

Table 4 THD% results of grid currents and voltages as a function of grid impedance

L_g (mH)	f_{res}(calculated) Hz	V_{PCC} THD %	Ig THD %	Kp
0.1	4194	2.48	1.50	0.2
0.2	3930	2.50	1.46	0.2
0.3	3724	2.53	1.45	0.2
0.4	3558	2.55	1.33	0.2
0.5	3422	2.58	1.43	0.2
0.6	3307	2.59	1.25	0.2
0.7	3210	2.61	1.17	0.2
0.8	3102	2.62	1.12	0.2

The table also includes the simulation results of the THD% of the grid current and voltage at the PCC. The impact of the grid inductance on the harmonic profile of the PCC voltage is recorded in Figure 4-10 for simulated grid inductance of 0.1mH, 0.4mH, and 0.8mH.

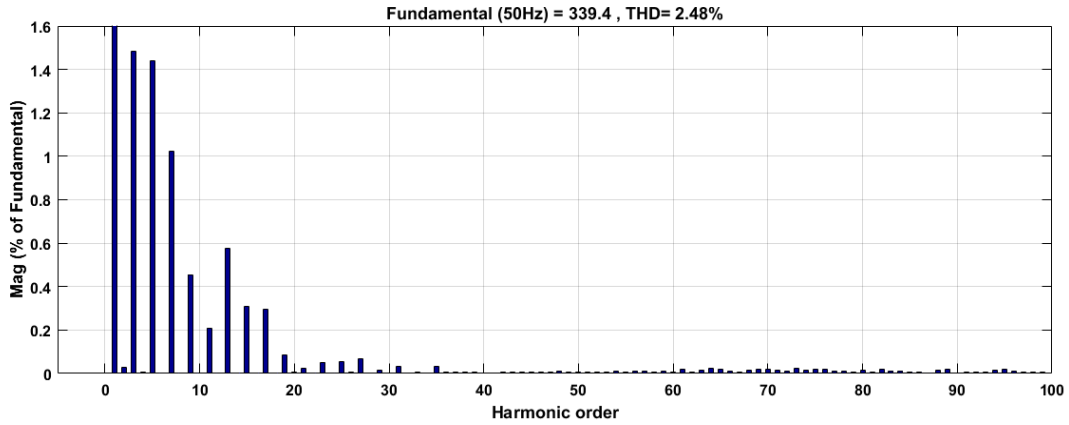

(a)

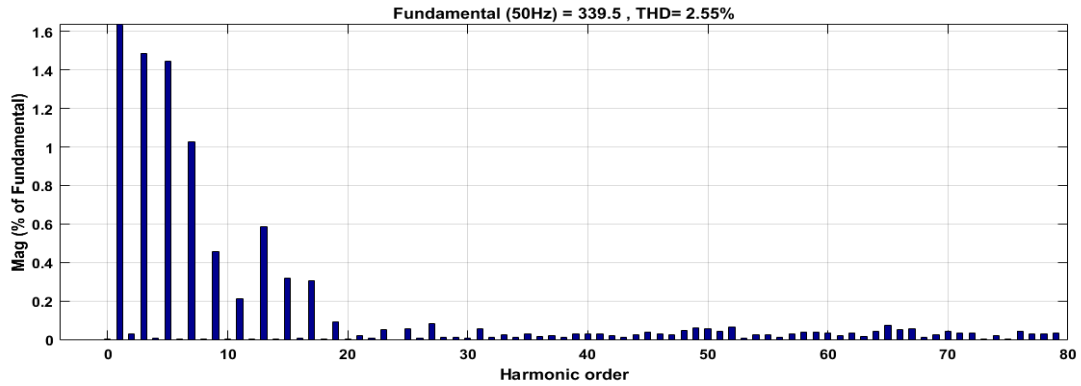

(b)

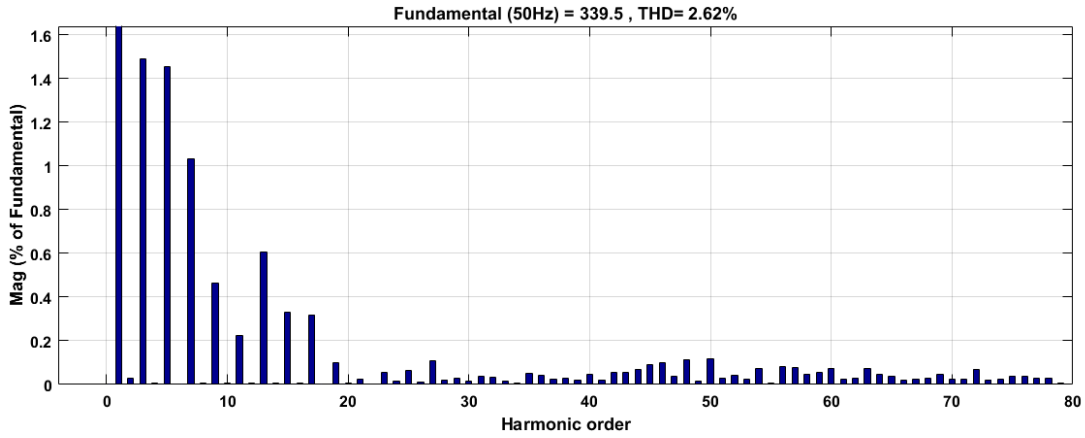

(c)

Figure 4-10 Harmonic profiles of the PCC voltage for (a) Lg=0.1mH, (b) Lg=0.4mH, and (c) Lg=0.8mH

As can be seen from the data above, the THD% of the PCC voltage has a proportional relationship with grid inductance, which means that the voltage signal at the PCC is affected by increasing grid inductance, which can also be seen in Table 4 where the THD% value increases from 2.48% in the case of Lg = 0.1mH to 2.62% in the case of Lg = 0.8mH. Moreover, the change in the grid inductor moves the harmonic order of the resonant peak towards the low-frequency range, which can be seen from Figure 4-11.

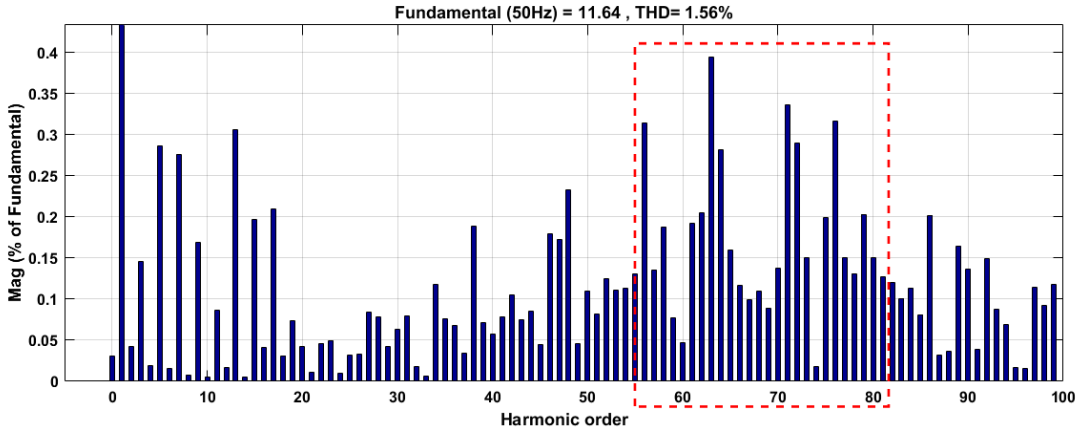

(a)

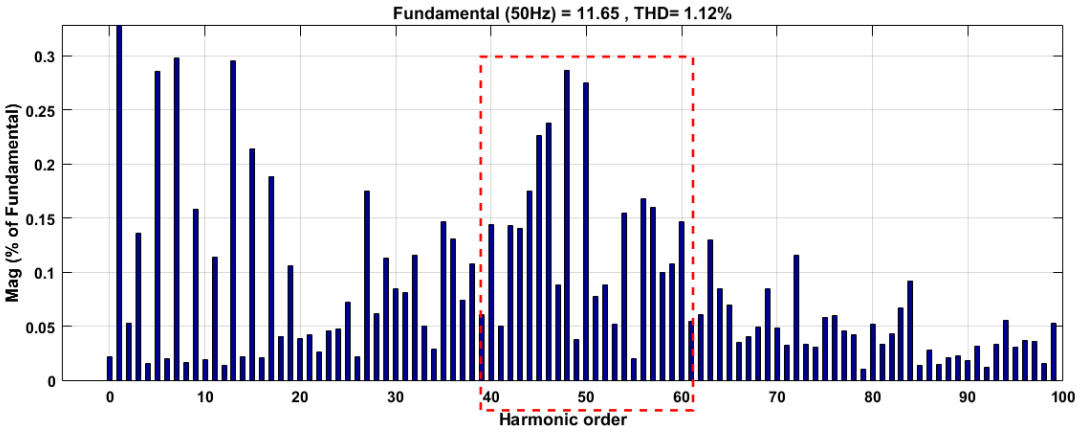

(b)

Figure 4-11 Impact of grid inductor variations on the position of the resonant peak: (a) Lg=0.1mH, (b) Lg=0.8mH.

The Bode plots of the system under a wide range of values of grid inductance are shown in Figure 4-12. As demonstrated in the figure, when the grid impedance increases, the resonant frequency and the controller bandwidth decrease, which may drive the system toward instability.

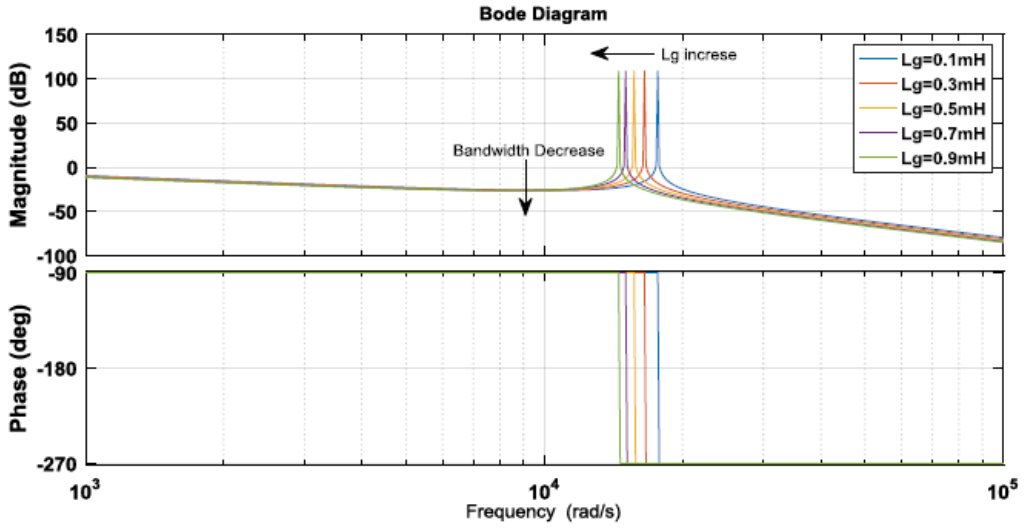

Figure 4-12 Bode diagrams of the non-damped system under a wide range of grid impedance values

It can therefore be concluded that variation in grid impedance has a significant impact on the performance of the VSI system in terms of stability and power quality. In previous study [128], these effects have been investigated based on a PI-controller-based implementation.

4.3.3 Effects of grid frequency variation

The voltage and frequency of the distribution network are affected by the coupling and decoupling of new resources, which poses risks to both power quality and stability. To guarantee system stability and satisfactory power quality, limits and standards such as IEEE1547 and IEC1727 have been established and have to be considered. In the IEEE1547 standards, the requirement is to disconnect the PV inverter system from the utility grid whenever the frequency or voltage levels exceed predefined thresholds [33]. In this section, the effect of frequency variation on VSI performance is investigated. It has been reported in [130] that the negative impact of frequency fluctuations on small scale distribution generators can vary from decreasing the power quality to complete islanding and loss of connection when exceeding the standard limitation. This scenario can be extremely challenging in term of the control design for the VSI, even when resonant controllers such as the PR controller are implemented. In the case of the PR controller, the controller structure consists of the fundamental frequency which is set to 50Hz in the internal blocks. As such, if the frequency is

subject to change, the controller might not be able to function as expected. The case can be even worse when PR+HC is used, as the degree of the HC is multiplied by the degree of the fundamental. In the literature, a number of solutions have been published [68, 70], which are based on modifying the PLL structure and feeding the controller with the frequency information.

To assess the sensitivity towards deviations in the background grid frequency, the simulated VSI was subjected to a frequency shift of ± 1Hz of the fundamental component (50 Hz). The variation of ±1 Hz was selected in accordance with the IEC grid code, which demands that the PV system should be able to ride through variations as large as ±1 Hz.

The results obtained for the impact of grid frequency variation on power quality and system stability are summarised in Table 5. The data provided show that the power quality is negatively affected in terms of THD% and DC injection. Furthermore, the grid current THD% and the PCC voltage THD% are both influenced by the ±1 Hz deviation. For example, the THD% of the grid current increases from 3.19% at a grid frequency of 50Hz (see Fig. 4-13) to 4.18% for a grid frequency of 50.4Hz (see Figure. 4-14). The impact is even more significant when the grid frequency is manually set to 51 Hz, where the THD% is found to exceed IEEE1547 standards. This is also the scenario for the THD% of PPC voltage, except in the case of -1 Hz variation where the THD% of the PCC voltage is hardly affected.

Table 5 Simulation results of the impact of frequency variations

Frequency (Hz)	*THD%_Ig*	*DC Components_Ig*	*THD% _V_{PCC}*	*DC Components_V_{PCC}*
50	*3.19*	*0.00145*	*2.47*	*0.0005*
50.4	*4.18*	*0.2559*	*3.96*	*7.668*
50.8	*4.71*	*0.1756*	*4.16*	*5.355*
51	*5.41*	*0.1753*	*4.16*	*3.349*
49.8	*4.27*	*0.0369*	*2.47*	*1.095*
49.4	*4.01*	*0.1345*	*2.47*	*4.068*
49	*4.53*	*0.2132*	*2.78*	*6.577*

Another important factor that weakens the power quality of the PV inverter system is the DC injection. According to IEEE standars1547, the maximum allowed DC injection has to be less than 5% of the full rated current [131]. The data in Table 5, show that as the grid frequency deviates from its normal fundamental value, the DC components in both the grid current and PCC voltage signals become larger. In the grid's normal operating condition (f =50 Hz), the DC component in the grid current signal is 0.00145, which is far smaller than the limitation in the standard. However, when the frequency starts to increase or decrease, the presence of the DC component grows larger. In fact, the proportion of the DC injection to the grid is unacceptable for the injected grid current for ± 1Hz.

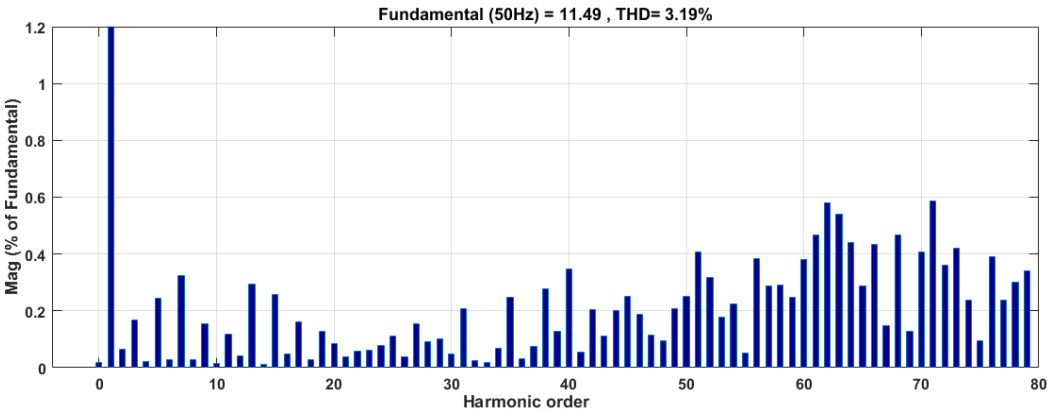

Figure 4-13 Harmonic profile of the inverter output current at a grid frequency of 50 Hz

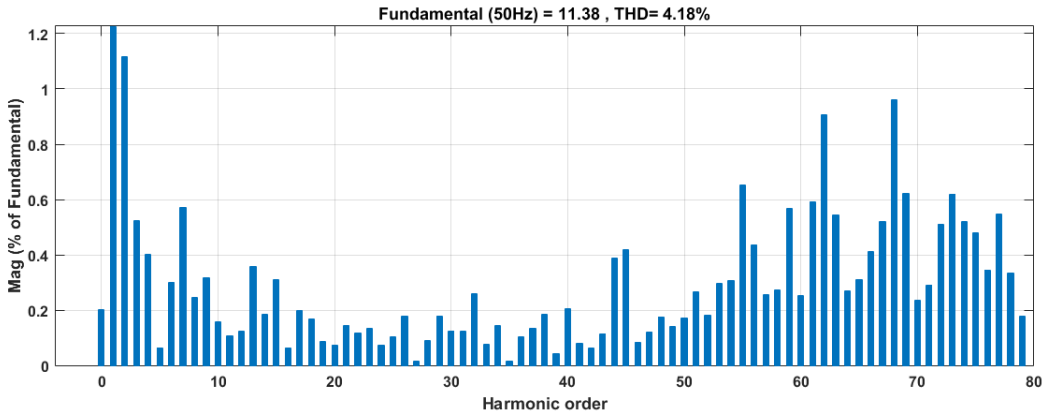

Figure 4-14 Harmonic profile of the inverter output current at a grid frequency of 50.4 Hz

Moreover, it has also been found that, as the frequency of the grid deviates from its nominal value, a unity power factor (PF) might not be guaranteed. Figure 4-15 shows the waveforms of the grid voltage and output current at a grid frequency of 50.8Hz.

As can be seen from the top-left inset of the figure, the synchronisation is not accurate, and a significant phase shift between the grid current and grid voltage can easily be observed.

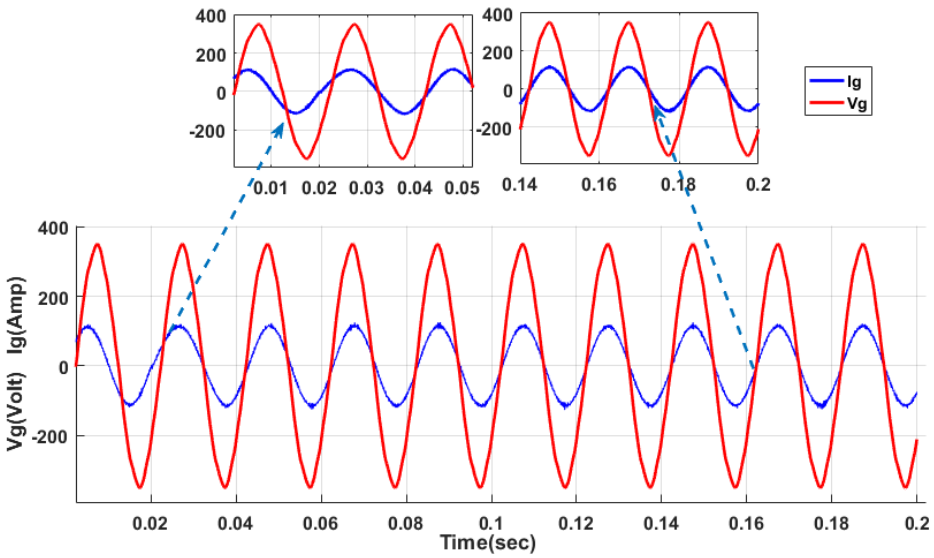

Figure 4-15 Grid voltage and current waveforms at a background grid voltage of 5.8 Hz

4.4 Chapter summary

This chapter presented a Simulink-based design of a single-phase PV grid-connected inverter. The Simulink model was used to investigate the harmonic interaction between the VSI and the background distribution system. In particular, the effect of grid operation conditions such as the grid voltage and frequency, as well as of variations in the grid impedance on the VSI performance, were investigated. The results of the investigation show that variations in grid operating conditions have a significant impact on the harmonic profiles of both the grid current and the PCC voltage. Furthermore, changes in the magnitude and phase angle of the background grid voltage were found to lead to variations in the magnitude and phase angle of the PCC voltage signal. In addition, it was demonstrated that deviation of the in grid frequency from its nominal value can challenge the performance of the current controller, reduce power quality in terms of THD, and lead to steady-state error. Likewise, the increased grid impedance that is associated with a weak grid can cause a distortion in the PCC voltage signal, which in turn influences the injected grid current.

CHAPTER 5

DESIGN AND IMPLEMENTATION OF THE PROPOSED ADAPTIVE PR CONTROLLER

5.1 Introduction

The penetration of PV systems connected to the grid is increasing rapidly. In particular, these systems are gaining fame and popularity due to their suitability for both standalone grid-connected systems [132, 133]. Due to the changeable grid operating condition, smart interface between dispatchers and the network that employ such systems are essential in order to satisfy the consumer demands in the one hand, and for safety and reliability purposes on the other hand [134]. One example of these changeable conditions is the variations in grid impedance. The reasons for variations in grid impedance can be combinations of several factors, including the characteristics of transformers, cables, and loads. Apart from the impedance of medium and high voltage transformers which is mainly inductive, low voltage cables introduce a prevalent resistive impedance that changes according to the distance between the PV system and the transformer [135]. Indeed, grid impedance information is of prime importance in inverter filter design, grid failure detection, compliance with standard specifications such as IEEE929, IEEE1547 and VDE0126, islanding operation and, last but not least, control loop tuning [134].

In this chapter, the design and implementation of the adaptive PR controller (APR) is proposed.

5.2 The proposed adaptive PR controller (APR)

This section presents the development of an on-line adaptation of the APR controller. To achieve this, a fourth-order digital band-pass filter is designed base on Sallen-Key topology. The task of the filter is to filter out the harmonic components around the resonance frequency from the PCC voltage waveform. The fourth-order band-pass filter block is inserted into the control loop in order to monitor and filter out the voltage signal at the point of common coupling (V_{PCC}). The filter is designed to only filter out the harmonic components around the resonant frequency (ω_{res}) which cause oscillation

in the voltage signal. The output signal of the band-pass filter has proceeds in such a way so it can be readable by the controller for parameter tuning. This process can be achieved by using statistic signal processing techniques which consists of signal rectification, integration and mean value determination. This yields estimation of any variation in grid impedance. Finally, the estimated grid impedance value is used as a reference for a look-up so as to select the appropriate corresponding PR parameters K_P and K_R. A two-dimensional look-up table is built and its values are selected based on the best values of K_P and K_R and the corresponding predicted grid impedance. The best values of the controller parameters have been selected using a Partial Swarm optimization algorithm (PSO). It is worth pointing out that only the inductive part is considered, as increases in grid inductance can leads to an unstable distribution system [79]. The technique of the proposed APR controller is illustrated in Figure 5-1.

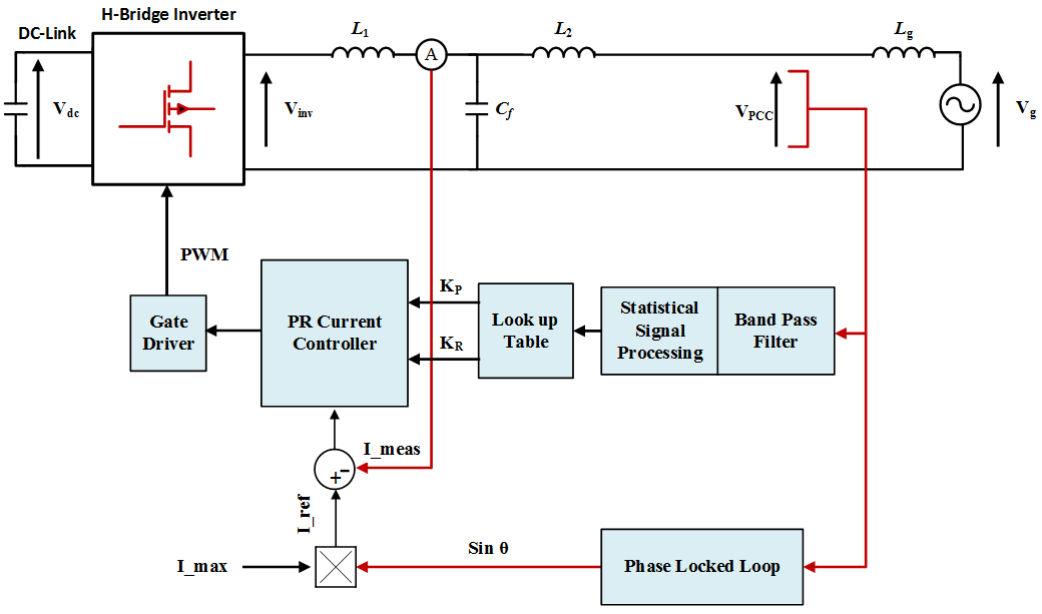

Figure 5-1 Block diagram of the proposed adaptive PR controller (APR)

5.2.1 Band-pass filter design for resonance detection

Band-pass filters are widely used in communication and signal processing applications for frequency selection at a pre specified range. In this work, a fourth-order band-pass filter with high attenuation rate of corner cut-off frequency is designed for resonance detection purpose. The targeted harmonic components at the resonance

frequency are relatively small in magnitude compared to fundamental components. For this reason, a Sallen-Key topology with Butterworth response is proposed to achieve a high-order response and to minimize the ripple at the filter pass-band respectively. In addition to its simplicity, the main advantage of such a topology is its capability of allowing a high quality factor combined with high pass gain without the use of inductors. The passive components and design process of the filter were achieved according to the guidelines given in [136] in which the design techniques of band-pass filters have been extensively discussed. The transfer function of a second order band-pass filer is given in equation 5.1.

$$H(s) = \frac{(1 + \frac{R_b}{R_a}s)\frac{s}{R_a C_1}}{s^2 + \left(\frac{1}{R_1 C_1} + \frac{1}{R_2 C_1} + \frac{1}{R_2 C_2} - \frac{R_b}{R_a R_f C_1}\right)s + \frac{R_1 R_f}{R_1 R_2 R_f C_1 C_2}s} \tag{5.1}$$

The transfer function of the desired 4th order filter is provided by the multiplication of two 2nd order band-pass filter transfer functions, yielding equation 5.2.

$$H_{BP}(s) = H_1(s)H_2(s) \tag{5.2}$$

where $H_1(s)$ and $H_2(s)$ are the transfer functions of first and second stages of the 2nd order filter respectively. Figure 5-2 shows two second-order Sallen-key band-pass filters cascaded together to shape the required fourth order filter. In this work, the designed bandpass filter operates in a frequency range between 3 kHz-to- 4.5 kHz, which is the bandwidth of harmonic components around the resonant frequency

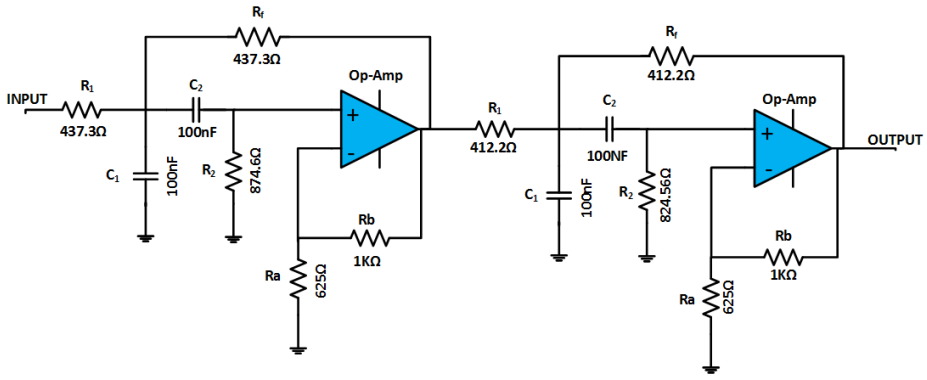

Figure 5-2 Circuit diagram of two cascaded second-order band-pass filters

It is important to mention that the bandwidth of the filter has been selected based on an FFT analysis of the voltage waveform at the PCC, and the calculation of the resonant frequency given in equation 5.3.

$$\omega_{res} = \sqrt{\frac{L_1 + L_2 + L_g}{L_1(L_2 + L_g)C_f}} \tag{5.3}$$

The specification of the 4th order band-pass filter is given in table 6.

Table 6 Specification of band-pass filter

Topology	*Order*	*Response*	*Central frequency*	*Bandwidth*
Sallen-Key	*4th*	*Butterworth*	*3750 Hz*	*1500 Hz*

For the digital implementation of the band-pass filter, the discretization method has to be carefully selected, because many of the existing techniques can result in pole displacement and frequency deviations at which high gain accrues with respect to the continuous transfer function [64]. It has been stated in [64] that most discretization methods result in acceptable performance when tracking the fundamental frequency reference of 50 Hz or even for low order harmonics, which is not the target of the proposed band-pass filter. However, in applications where signals of higher frequencies are targeted, such as in the proposed bandpass filter, the performance level might not be acceptable and special attention has to be paid since some methods have a direct impact on stability. For the designed band-pass filter, discretization has been achieved using the "c2z" function in MATLAB with a suitable discretization method. The *s*-domain transfer function of the designed 4th order bandpass filter is given in equation 5.4

$$BP(s) = \frac{4.09e^{9}s^{2}}{s^{4} + 1.332e^{4}s^{3} + 1.155e^{9}s^{2} + 7.388e^{12}s + 3.076e^{17}} \quad (5.4)$$

For the selection of the discretization method, a comparison has been carried out between two different methods: the zero-order hold (ZOH) and trapezoid (Tustin) method. The zero order hold (ZOH) method as given in equation 5.5 has been selected due to its ability to produce an identical match in the frequency response between the continuous and discrete transfer functions.

$$G(z) = (1 - Z^{-1})Z\left\{L^{-1}\left\{\frac{G(s)}{s}\right\}\right\} \quad (5.5)$$

The corresponding *z*-domain transfer function using the ZOH method is given in equation 5.6.

$$BP(z) = \frac{3.654z^{3} - 5.217z^{2} - 1.234z + 2.798}{z^{4} + 1.972z^{3} + 1.996z^{2} + 1.015z + 0.2639} \quad (5.6)$$

As illustrated in Figure 5-3, the frequency responses of the band-pass filter for both the *s*- and *z*-domains are obviously identical for both, the low and high harmonic orders. The figure also shows that the filter high gain is 38dB, which will magnify the magnitudes of the harmonic components around the resonant frequency for ease of detection, where the harmonic components around the fundamental frequency are attenuated to -56 dB.

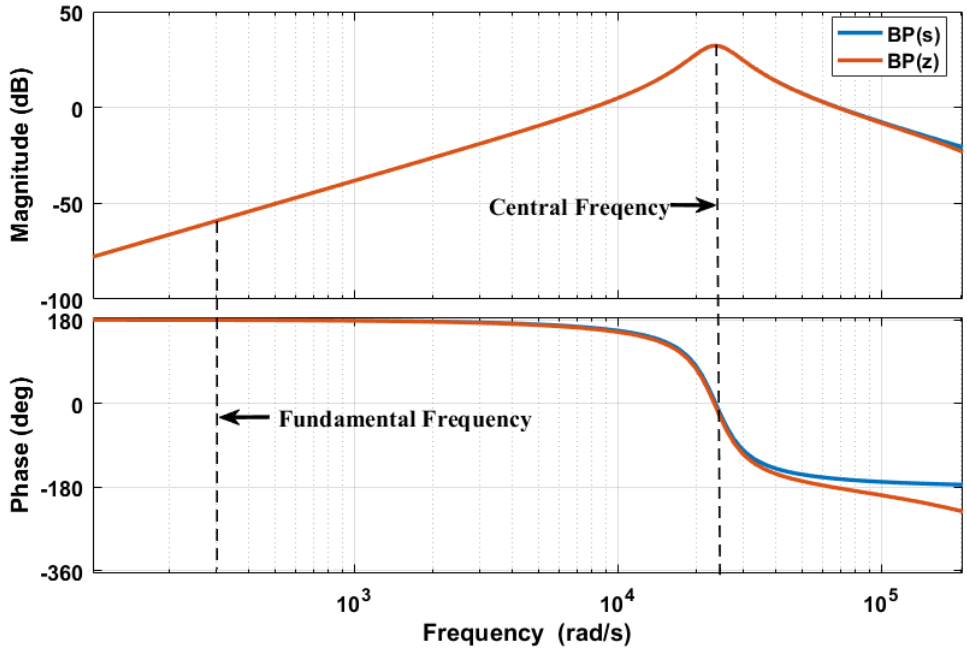

Figure 5-3 Comparison of filter frequency response between s-domain and z-domain transfer functions using ZOH discretization method

In contrast, the discretization using the Tustin method which is given in equation equation5.7 has resulted in pole displacement and different frequency responses between the *s*-and *z*-domain.

$$G(z) = G(s)_{s=\frac{2}{T_s}\frac{z-1}{z+1}} \tag{5.7}$$

where *Ts* is the sampling time.

This can be clearly observed in Figure 5-4, which shows the magnitude and phase angle frequency response of the band-pass filter. Although there is a match between the two frequency responses in the *s*- and *z*-domains in the low-order harmonic components, the presence of frequency deviation in the high harmonic orders is obvious due to pole displacement. This can reduce the robustness and affect the performance of the designed filter.

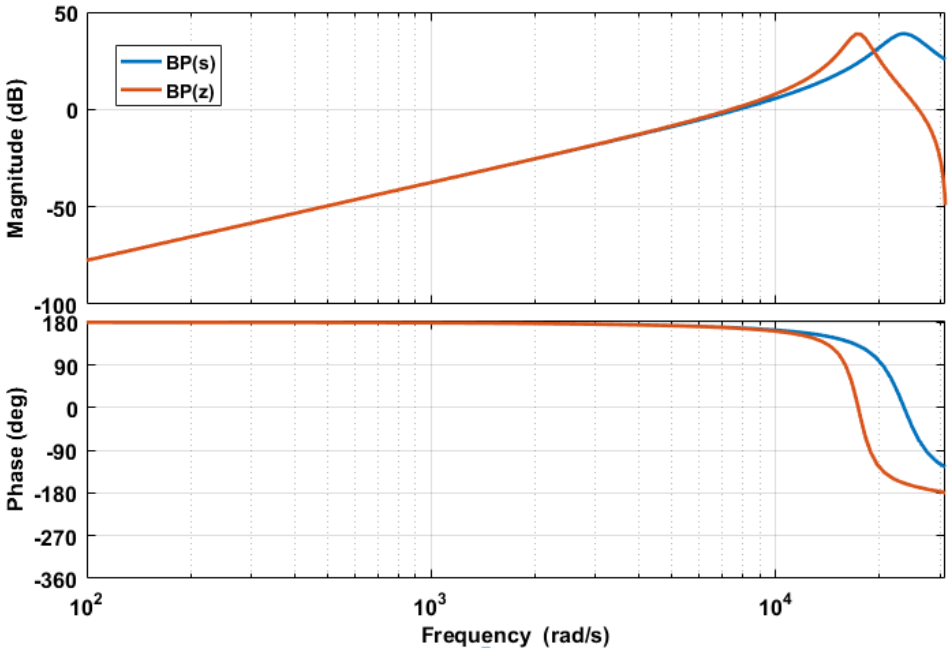

Figure 5-4 Comparison of filter frequency responses comparison between s-domain and z-domain transfers function using Tustin discretization method

The proposed digital band-pass filter is built in Matlab/Simulink using a discrete transfer function block as shown in Figure 5-5. The input signal to the filter is the voltage signal at the PCC (V_{PCC}) which captured by the voltage sensor placed at that point.

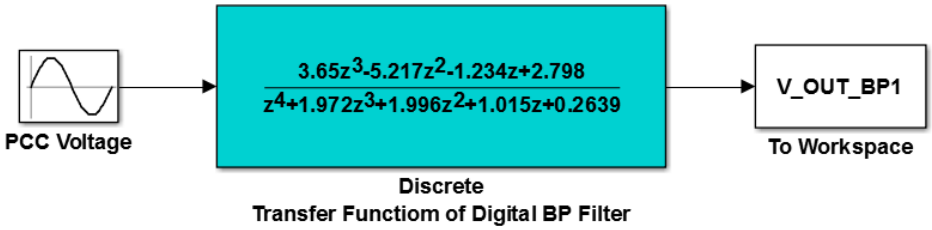

Figure 5-5 Block diagram of the digital band-pass filter in Matlab/Simulink

To assess the performance and filtering effects of the designed digital band-pass filter, FFT analysis has been carried out to the output distorted signal from the band-pass filter (V_{OUT-BP}) in Matlab. At first, the single-phase grid-connected PV inverter shown earlier in Figure 4-1 was interfaced to the grid via the LCL filter in series with grid

inductance varying from 0.1mH to 0.9mH. Figure 5-6 shows the PCC voltage waveform in the case of 0.1mH, which is the input signal to the digital band-pass filter.

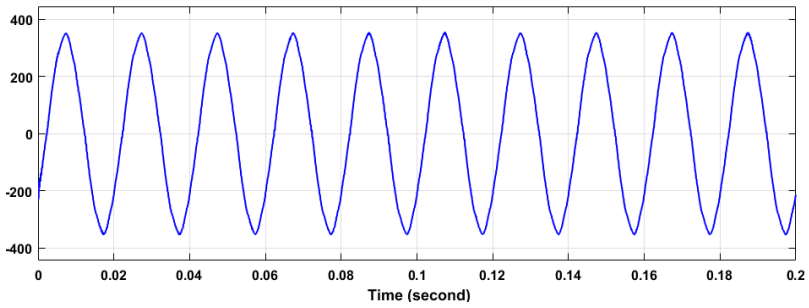

Figure 5-6 PCC voltage waveform (VPCC) at 0.1mH of grid inductor Lg. (I demand=8.32A RMS, VDC=400V, Vg=230V RMS)

As this waveform is received by the digital filter, the resonance will be detected, and only the harmonic components around this resonance will shape the output voltage signal from the band-pass filter (VOUT-BP) as shown in Figure 5-7. This figure illustrates that, even with a low value of grid impedance of 0.1mH, the designed band-pass filter is still able to detect the resonance due to the magnification action achieved by the designed high pass-band gain.

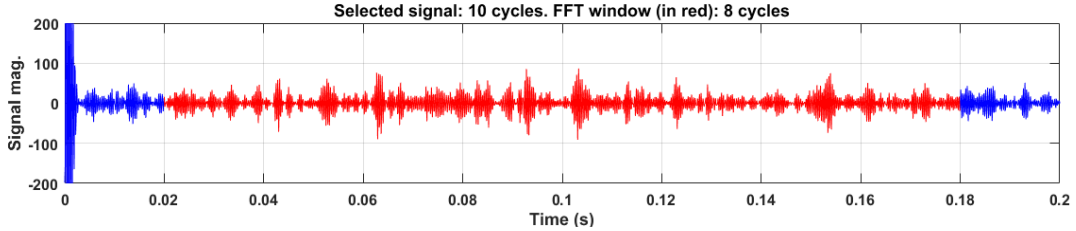

Figure 5-7 Output voltage waveform from the band-pass filter at 0.1mH of grid inductor (I demand=8.32A RMS, VDC=400V, Vg=230V RMS)

The FFT analysis for the output voltage signal from the band-pass filter (V_{OUT-BP}) is shown in Figure 5-8 in the case of 0.1mH. The magnitude of the resonance captured within the filter bandwidth as shown within the red box is significantly magnified and

is presented as a percentage of the fundamental frequency. On the other hand, all the harmonic components outside of the filter bandwidth are attenuated.

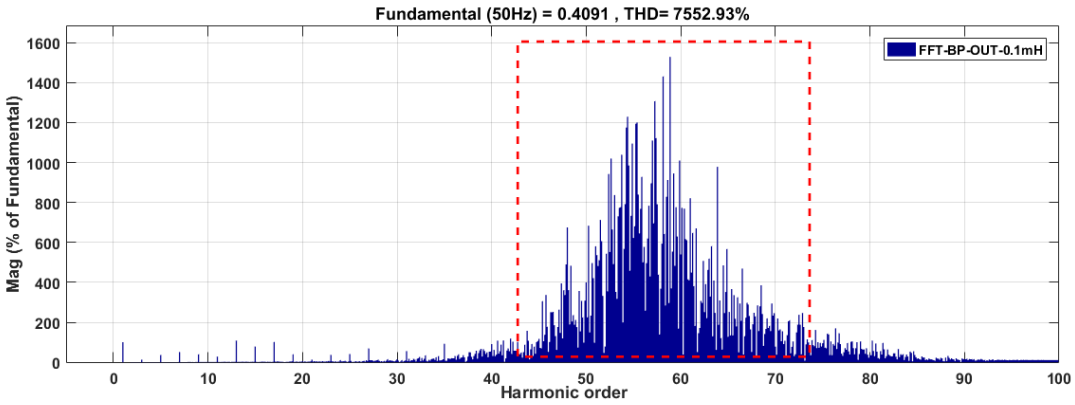

Figure 5-8 Harmonic profile of the output voltage from the bandpass filter at Lg=0.1mH (I demand=8.32A RMS, VDC=400V, Vg=230V RMS)

For further investigation regarding the band-pass filter's performance, the grid inductance of the single-phase grid-connected PV inverter system was increased to 0.8mH. Figure 5-9 shows the PCC voltage which is the input to the filter. As can be noticed, a high level of oscillation can be observed on the input signal compared with the same waveform in the case of the 0.1mH grid inductor which proves that as the grid inductor increases more oscillation will be present in voltage waveform at the PCC.

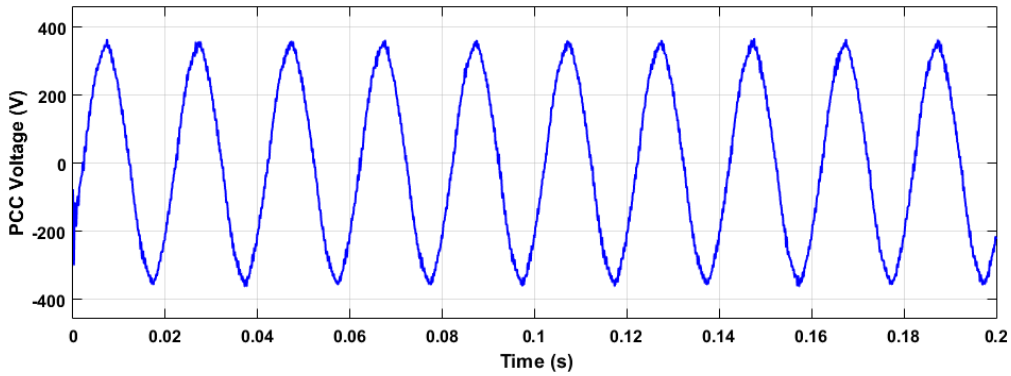

Figure 5-9 PCC voltage waveform (VPCC) at 0.8mH of grid inductor Lg. (I demand=8.32A RMS, V_{DC}=400V, V_g=230V RMS)

The output voltage signal from the band-pass filter (V_{OUT-BP}) and its FFT analysis in the case of 0.8mH are shown in Figures 5-10 and 5-11 respectively.

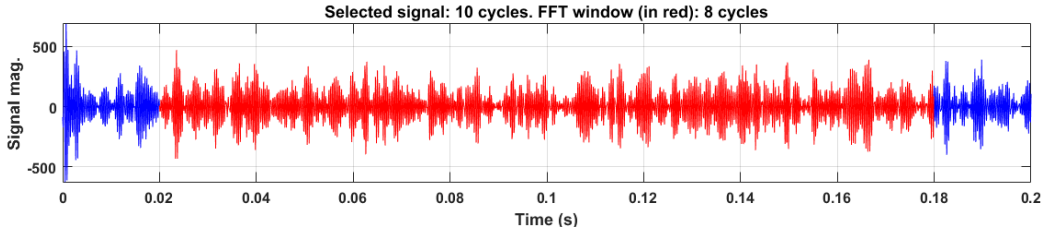

Figure 5-10 Output voltage waveform from the band-pass filter at 0.8mH of grid inductor (I demand=8.32A RMS, VDC=400V, Vg=230V RMS)

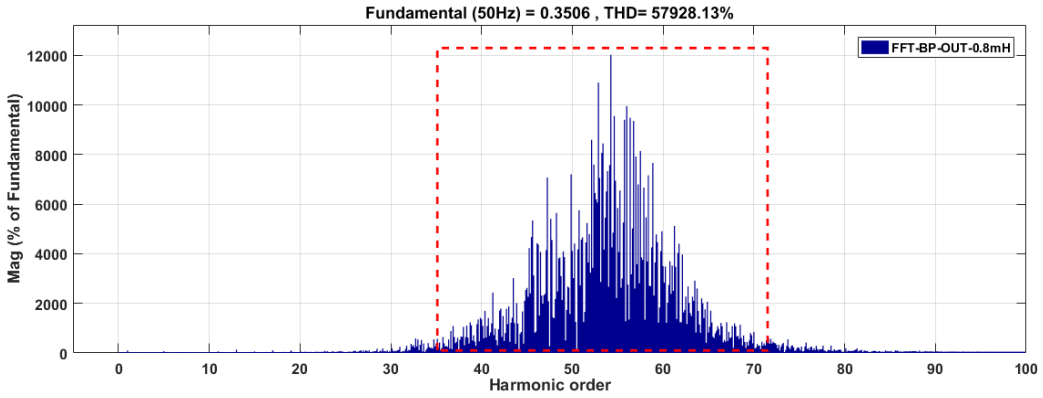

Figure 5-11 Harmonic profile of the output voltage from the bandpass filter at Lg=0.8mH (I demand=8.32A RMS, V_{DC}=400V, V_g=230V RMS)

It can be noted from the figure that the bandpass filter is able to effectively detect and capture the harmonic components around the resonance frequency. Moreover, the shape of the filtered signal is different and changes according to the change in the grid inductor.

5.3 Gain scheduling of the proposed adaptive PR controller

The parameters of the conventional PR controller (K_P, K_R), are tuned at fixed values. In this way, the control action will not follow the change in grid operating conditions such as time-varying grid impedance because the controller needs the impedance information in order to tune the proportional and resonant gains accordingly. The 4th order digital band-pass filter presented in section 5.3 was employed to detect and capture the harmonic components around the resonance frequency of the PCC voltage waveform within the selected bandwidth. It has been shown in Figures 5-7 and 5-10, that the output waveform from the band-pass filter is different for different values of

grid inductance. These obtained signals are in the form of oscillating waveforms and with the help of signal processing techniques, they can be recognised and read by the controller to be considered in the control loop, and hence the controller parameters can be retuned. So the next step following the filtering action is a statistical signal processing chain which consists of the following analysis: signal rectification, integration and the averaging of the filtered signal obtained. The control structure of the adaptive PR controller is depicted in Figure 5-12.

As can be seen, the signal processing of the V_{OUT-BP} signal provides the corresponding grid inductance to the pre-built two-dimensional look-up table. This look-up table consists of the best possible values of K_P and K_R for a wide range of variation in grid inductance from 0.1mH up to 0.8mH. It is worth mentioning that the selection of these inductance values was conducted according to the IEC 60725 standard. The standard states that the maximum grid impedance for a single-phase two-wire 230V 50Hz supplies is 0.4+j025 Ω, which is equal to 0.4Ω and 0.796mH respectively.

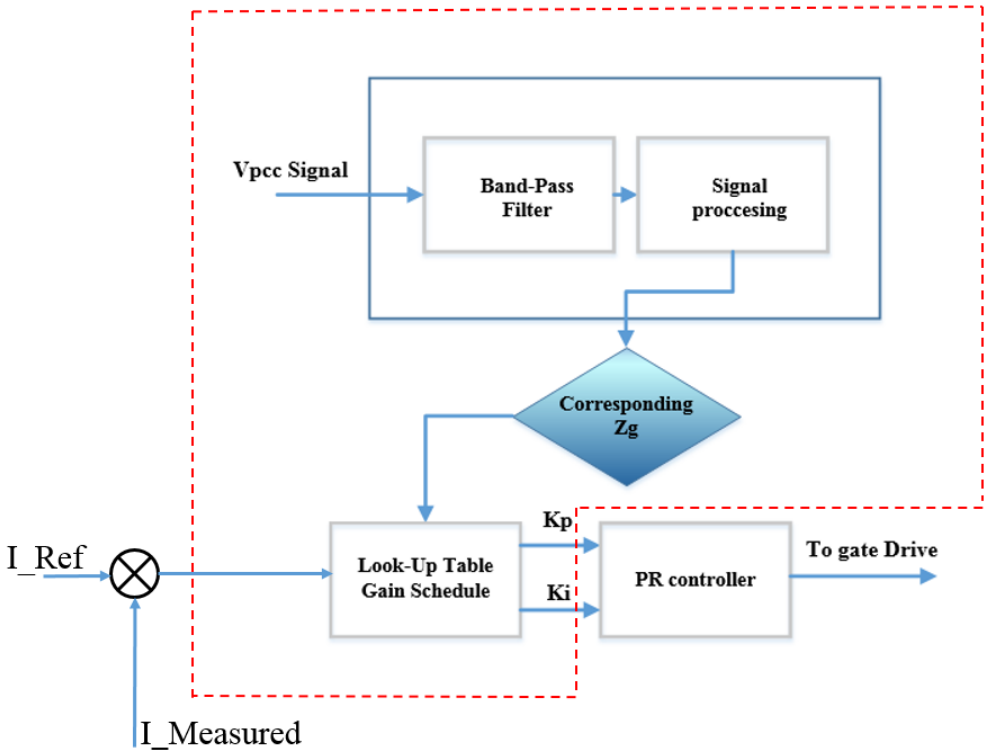

Figure 5-12 Gain schedule of adaptive PR controller

5.3.1 Simulation results of statistical signal processing

As the PCC voltage signal shown in Figures 5-13.a, and 5-14.a goes through the digital band-pass filter, the filter's high pass gain will allow only the harmonic components around the resonant frequency to be passed in the form of an oscillating signal, while attenuating those components around the fundamental frequency. This can be easily seen in Figure 4, where the attenuation gain is equal to -56 dB as illustrated in Figure 5-3 in section 5.3.1. Figures 5-13 and 5-14 show the simulation results of the system being connected to grid inductances of 0.1mH and 0.8 mH respectively. As can be seen from Figure 5-13b, the asymmetrical oscillation of the filtered signal in the case of Lg = 0.1mH is less than that of L_g= 0.8mH presented in Figure5-14b.

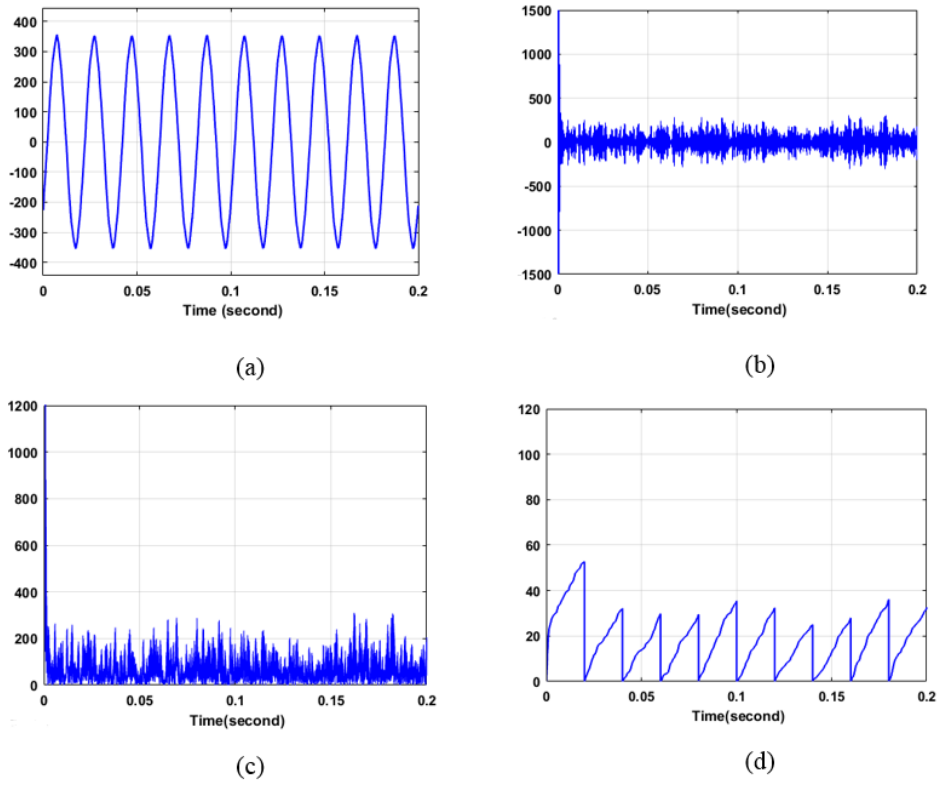

Figure 5-13 Simulation results of the filtering and signal processing chain of L_g = 0.1 mH: (a) Filter input Vpcc signal. (b) Filter output signal, (c) Rectifying signal; and (d) integrated signal.

In fact, it has been found that, the higher the grid inductor, the more oscillation is present in the voltage signal. The next step in the processing chain is the rectification

of the filtered signal to offset the negative part, yielding, the rectifying signals shown in Figures 5-13c and 5-14c for L_g = 0.1mH and L_g = 0.8mH respectively.

The results shown in Figures 5-13d, and 5-14d illustrate the second step which is the integration of the rectified signal. This has been accomplished by summing up the rectified signal at every PCC voltage fundamental cycle. Again, the change in grid inductance can be linked to the change in resonant frequency, where the peak points of the integrated signal related to L_g = 0.8mH is significantly bigger than those of L_g = 0.1mH. Since the maximum values of the integrated signal are different for every cycle, the last step in the signal processing is averaging, which is conducted by taking the average of the last ten cycles of the integrating signal.

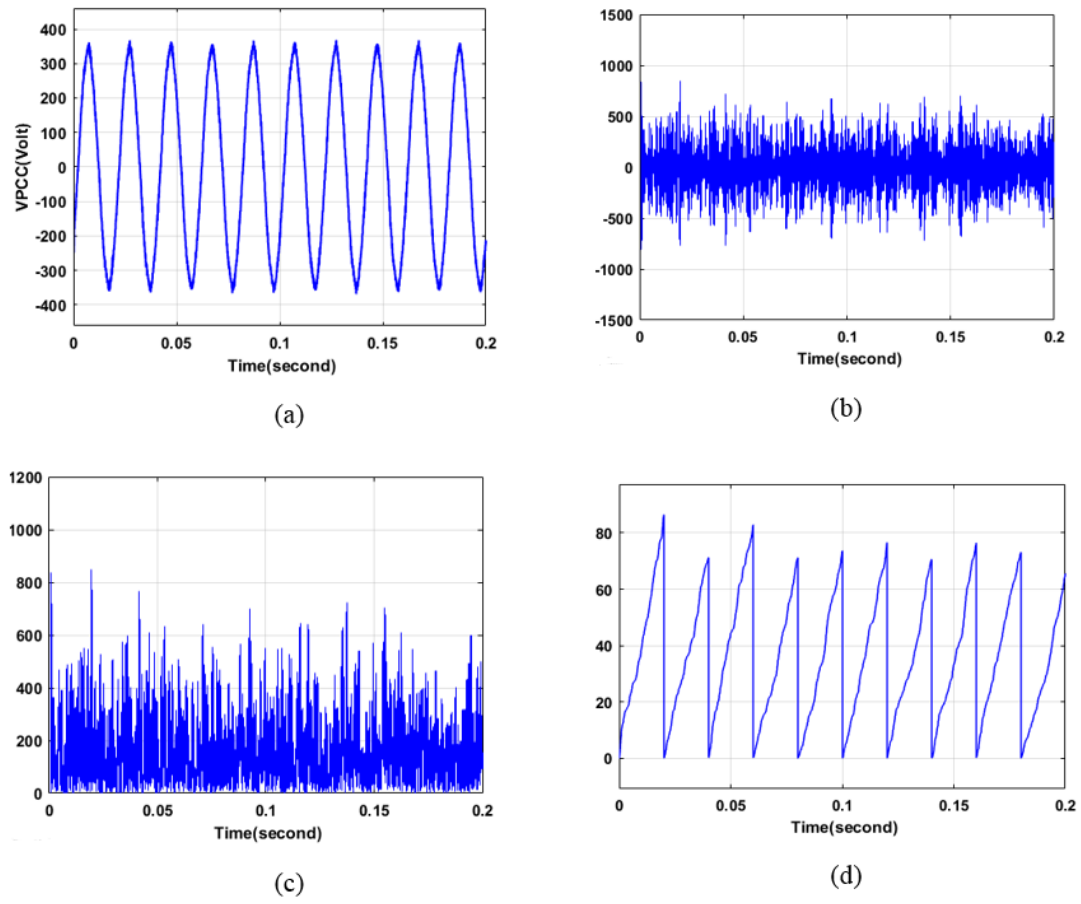

Figure 5-14 Simulation results of filtering and signal processing chain of L_g = 0.8mH: (a) Filter input Vpcc signal (b) Filter output signal, (c) Rectifying signal; and (d) integrated signal.

The resulting value in every case is the corresponding value of the grid inductance which is used to build the look-up table for the adaptive controller gains K_P and K. The data included in table 7 present the average values corresponding to two different values of grid inductance.

Table 7 Average values of the integrated signal for 0.1mH and 0.8mH

Lg (mH)	*Maximum values of the last ten cycle*										*Average value*
	1	*2*	*3*	*4*	*5*	*6*	*7*	*8*	*9*	*10*	
0.1	*52.74*	*32.16*	*29.85*	*29.99*	*31.87*	*35.43*	*25.01*	*35.75*	*32.21*	*27.98*	*30.50*
0.8	*86.47*	*71.22*	*82.87*	*71.19*	*73.4*	*70.6*	*76.57*	*75.88*	*73.11*	*65.17*	*74.84*

5.4 Online adaptation of look-up table for the tuning of PR controller parameters using particle swarm optimisation algorithm.

The parameters of the PR controller are tuned online according to a generated look-up-table built by an iterative technique known as Particle Swarm Optimization (PSO). This algorithm works in a collective way in which members of the population work together in random particle movement in order to find a global optimum without selectivity [137].

One advantage of this algorithm is that even low-fitness population members are not discarded but survive to be the subjects of future successful members of the swarm. Every particle in the population Xi is considered to be a point in the N-dimensional space to represent the optimisation problem; hence;

$$X_i = (X_{i1}, X_{i2}, \dots\dots\dots\dots, X_{iN}) \; for \; i = 1,2, \dots\dots\dots, M \tag{5.8}$$

where N is the number of variables and M is the number of particles which form the population. Each particle in the swarm is completely free to fly within the search space with a velocity $\mathbf{V}_i$ in addition to its position. This velocity is continuously adjusted according to the flying history of the population members and the particle itself.

$$V_i = (V_{i1}, V_{i2}, \dots\dots\dots, V_{iN}) \; for \; i = 1,2, \dots\dots.., M \tag{5.9}$$

Each particle in the search space has a position corresponding to a potential result. This position is evaluated according to a given performance function in order to assess the fitness value of that particle. The particle collects information from other population members about the best position to date, and in the same time to save this position. The particle then determines the next displacement vector within the search space based on the velocity and the best position as depicted in Figure 5-15. The motion of each particle is given in the following equations:

$$v_{in}^{k+1} = c_1 v_{in}^{k+1} + c_{max} r_1 \{0,1\}\left(p_{in}^{k} - x_{in}^{k}\right) + c_{max} r_2 \{0,1\}\left(g_{in}^{k} - x_{in}^{k}\right) \tag{5.10}$$

$$x_{in}^{k+1} = x_{in}^{k} + v_{in}^{k+1} \tag{5.11}$$

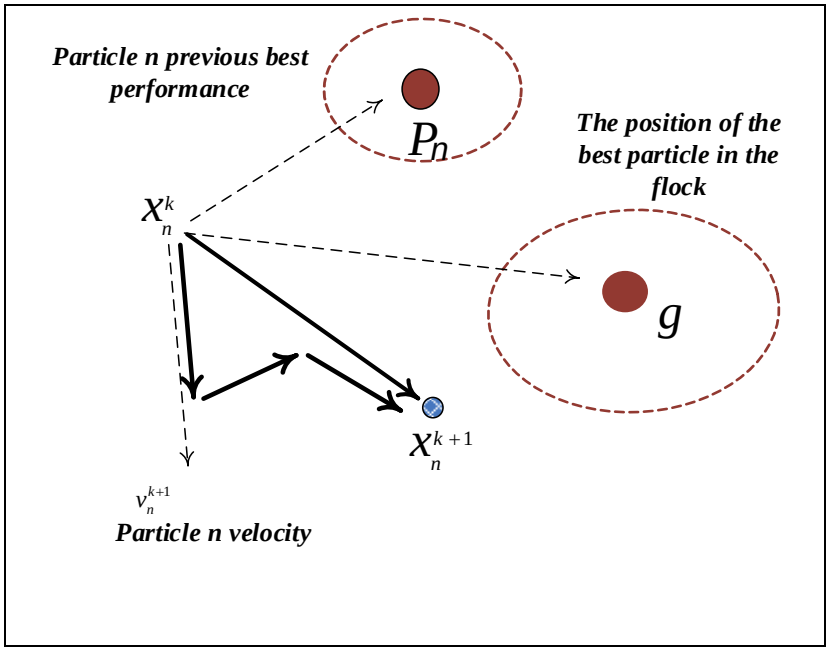

Figure 5-15 Three fundamental elements for the calculation of the next displacement of a particle

For the proposed adaptive PR controller, the PSO algorithm was employed to determine the best values for the controller parameters K_P and K_R which give the best

controller performance under a wide range of variation in grid inductance. Both the total harmonic distortion (THD %) of the injected grid current Ig and voltage at PCC were considered in the cost function given in equation 5.12. Moreover, the error signal resulting from subtracting the reference and measured grid current signals were also considered for the further elimination of steady state error.

$$f(K_P, K_R) = \sum \Big[\Big| I_{g_{ref}} - I_{g_{mes}} \Big| + \Big| THD_{I_{g_{ref}}} - THDI_{g_{mes}} \Big| \Big| THD_{V_{PCC_{ref}}} - THDV_{PCC_{mes}} \Big| \Big] \Delta T \tag{5.12}$$

where $I_{g_{ref}}$ and $I_{g_{mes}}$ are the reference and measured currents respectively.

This equation works in co-operation with a velocity and position equations as shown in equation (5.13), and equation (5.14).

$$V_c(k) = k\big(wV_c(k-1)\big) + c_1(P_b(k) - P(k-1) + c_2(g_{best}(k)) - P(k-1)) \tag{5.13}$$

$$P(k) = P(k-1) + V(k) \tag{5.14}$$

Where, g_{best} denotes the best values of K_p and K_R, c_1 and c_1 are constants.

Figure 5-16 shows the simulation results of the controller parameters K_p and K_R and the resulted THD% values of grid current and voltage at the PCC. It is obvious from the figure that the values of K_P and K_R provided by the PSO algorithm have led to the lowest possible total harmonic distortion for the injected grid current and for the voltage at the PCC, and hence, the power quality requirements for the grid-connected PV inverter system have been satisfied.

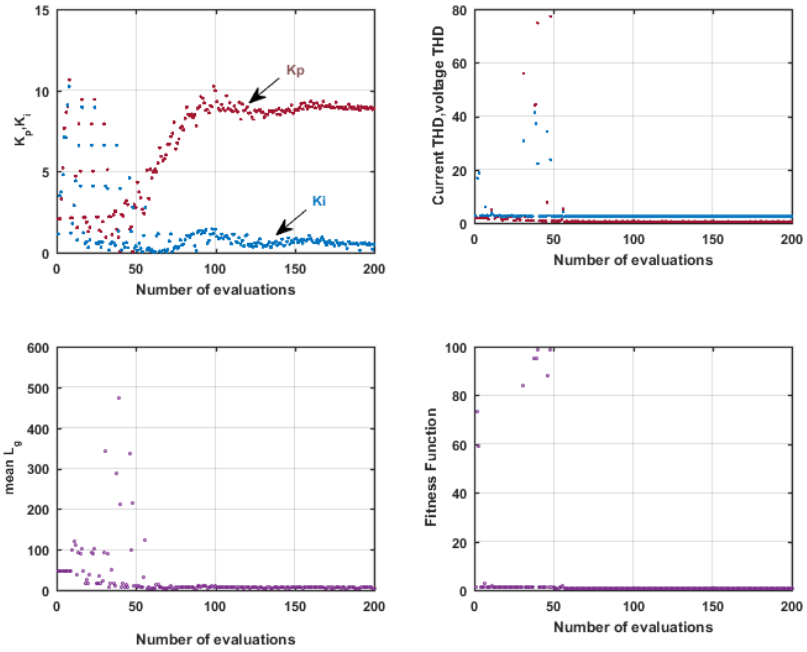

Figure 5-16 Path of the best values for KP and KR determined by the PSO

To evaluate the concept of the proposed adaptive PR controller, the designed 2 kW single-phase grid-connected PV inverter system was used first with the conventional PR controller which has fixed values of KP and KR and then with the adaptive PR controller. The comparison was based on the performance of both controllers in terms of the lowest THD% values of grid current and PCC voltage. The system was connected to a wide range of grid inductance varying from 0.1mH representing a stiff grid to 0.8mH representing a weak grid. The values of THD% of the grid current as well as the PCC voltage were recorded are shown in table 8.

Table 8 Comparison results of conventional PR and APR controller

L_g (mH)	*APR*		*PR*	
	Ig_THD%	*Vpcc_THD%*	*Ig_THD%*	*Vpcc_THD%*
0.2	*0.55*	*2.47*	*0.99*	*2.50*
0.4	*0.54*	*2.48*	*0.99*	*2.55*
0.6	*0.61*	*2.49*	*0.94*	*2.59*
0.8	*0.57*	*2.49*	*0.95*	*2.63*

The figures in the table demonstrate that the performance of the system with the proposed adaptive scheme APR is much better than that using the conventional PR controller. The total harmonic distortion of the grid current as well as PCC voltage has been significantly improved for all cases of grid inductance variation. For instance, at a grid inductance of 0.2mH, the recorded THD% of the grid current under the conventional PR controller was almost twice as much compared to that under the proposed APR controller, where the THD of the PCC voltage under the APR controller is slightly less than that of the PR controller.

Fast Fourier Transform (FFT) analysis has been carried out for the inverter output current with the adaptive and conventional PR controllers. As illustrated in Figures 5-17 and 5-18, the THD of the grid current under the adaptive PR controller is less than that of the conventional PR controller.

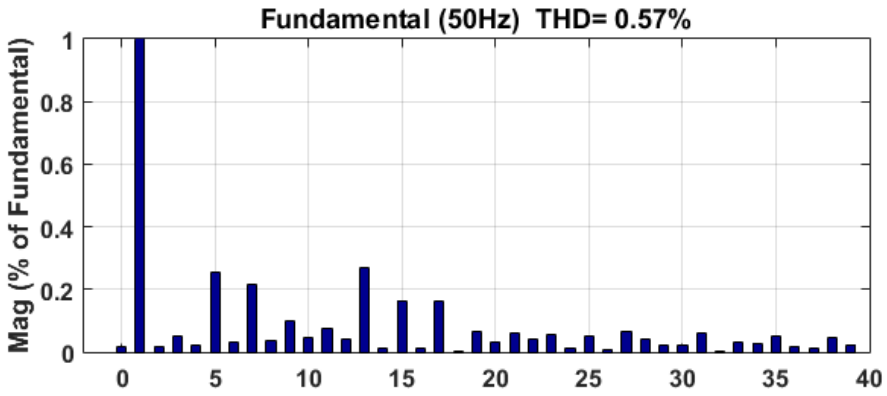

Figure 5-17 FFT analysis of grid current with APR controller for grid inductance of 0.8mH

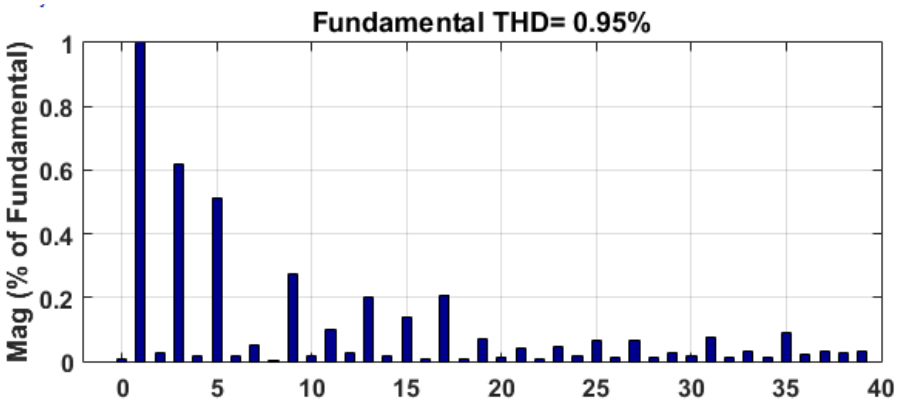

Figure 5-18 FFT analysis of grid current with PR controller for grid inductance of 0.8mH

Figure 5-19 shows the THD of the grid current for a system with grid impedance varied abruptly from 0.2, 0.4, 0.6, and 0.8mH in an interval of 0.2 second for each. As presented in the figure, the APR controller parameters are tuned in accordance with the grid impedance variation. The PR control parameters K_p and K_R change to keep the THD% of grid current at acceptably low levels according to the IEEE929 limit of less than 5 %. In each case, the proposed adaptive controller shows very promising results and can handle any variation in grid impedance. Finally, the simulation results of the harmonic-polluted grid voltage with injected grid current under the proposed control strategy in Figure 5-20 shows that the injected grid current is regulated and synchronized with the grid voltage under wide range of variations in grid impedance. This demonstrates the effectiveness and robustness of the proposed APR controller.

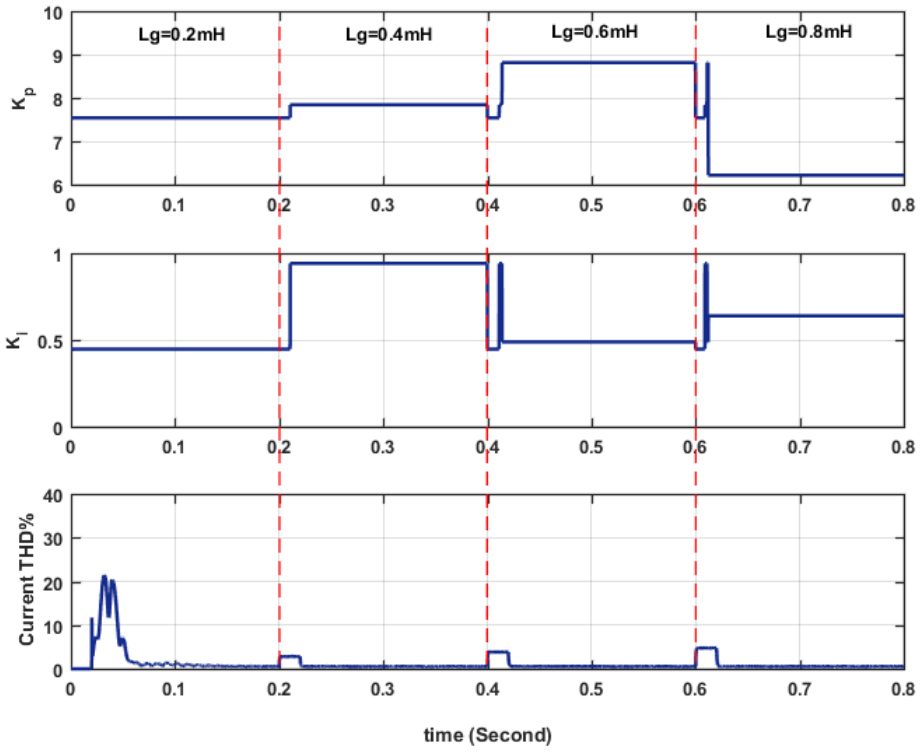

Figure 5-19 Online adaptation of look-up table for APR controller

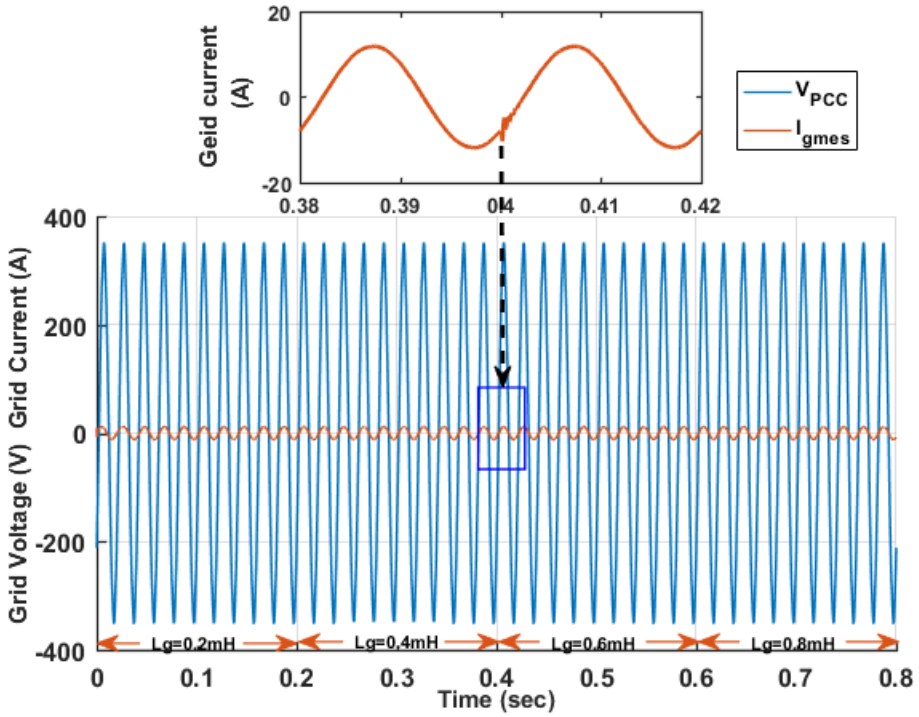

Figure 5-20 Grid voltage and current waveforms under changeable grid impedance with the proposed control strategy.

5.5 Chapter summary

In this chapter, the proposed adaptive PR controller has been presented. The main issue considered is tuning the controller parameters in accordance to the change in grid impedance. A new grid impedance estimation method based on the detection of resonance is proposed. The proposed estimation method employs a digital band-pass filter combined with a statistical signal processing technique. It has been demonstrated that the change in grid impedance leads to a change in the resonance frequency of the voltage signal at the PCC. The bandwidth of the band-pass filter ensures that only the harmonic components around the resonance frequency is captured and then passed. The output signal from the filter is analysed by as signal processing technique consists of signal rectification, integration and average value determination.

The parameters of the PR controller are retuned whenever a change in the grid impedance is detected based on data stored in a look-up table. This look-up table consists of the best possible values controller parameters for a wide range of variation in grid inductance. Particle Swarm Optimization algorithm is used in order to

determine the parameters of the APR controller which ensure the lower THD of injected grid current as well as lower THD of PCC voltage.

The proposed scheme is implemented in the Simulink model and it is demonstrated to be effective in detecting the variation in grid inductance and retuning the controller parameters to obtain a sinusoidal current and voltage with the lowest possible levels of THD.

CHAPTER 6

EXPERIMENTAL SET-UP AND PRACTICAL WORK PREPARATION

6.1 Introduction

This chapter presents the implementation of the single-phase PV grid-connected inverter for the experimental phase of the research work. The experimental system is designed and installed to link the DC source that represents the PV source to the utility grid in a laboratory environment. An overview of the test rig hardware and grid synchronisation sequence is first provided. This is followed by a detailed description of the system's components and the platform of the employed microcontroller, as well as of the system isolation and protection circuit.

6.2 Overview of experimental grid-connected PV inverter system

The experimental system is designed and installed to link the DC source and the utility grid in the Electrical Power laboratory at Newcastle University. A schematic diagram shown in Figure 6-1 gives a general overview of the design of the experimental system.

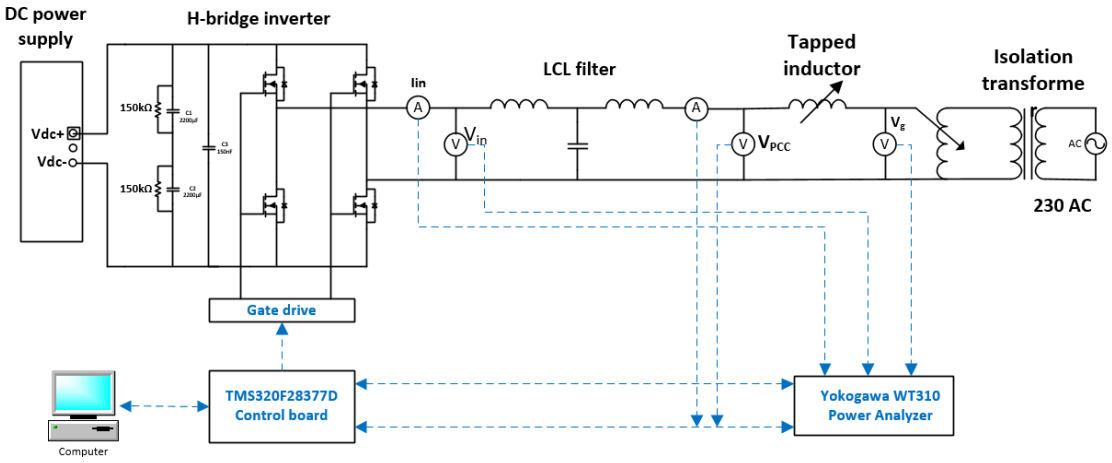

Figure 6-1 Schematic diagram of the test rig system

The system consists of a DC power supply (LP600-4 0-600V 0-4A) which is connected to a silicon carbide Mosfet H-bridge inverter. The inverter output is connected to a

low-pass LCL filter in series with a tapped inductor which represents the variation in grid inductance. Via the LCL filter, the inverter is coupled to the distribution network via an isolation transformer and a variac for safety and protection purposes and to step down the AC mains voltage 230V. A digital Yokogawa WT310 power meter is used to monitor and analyse the output waveforms of the system. The system is provided with a protection circuit that controls the on and off switching process which can quickly disconnect the system in case of emergency. Figure 6-2 a, and b shows a photograph of the experimental system along with its protection unit, while the parameters used in the practical work are given in table 9.

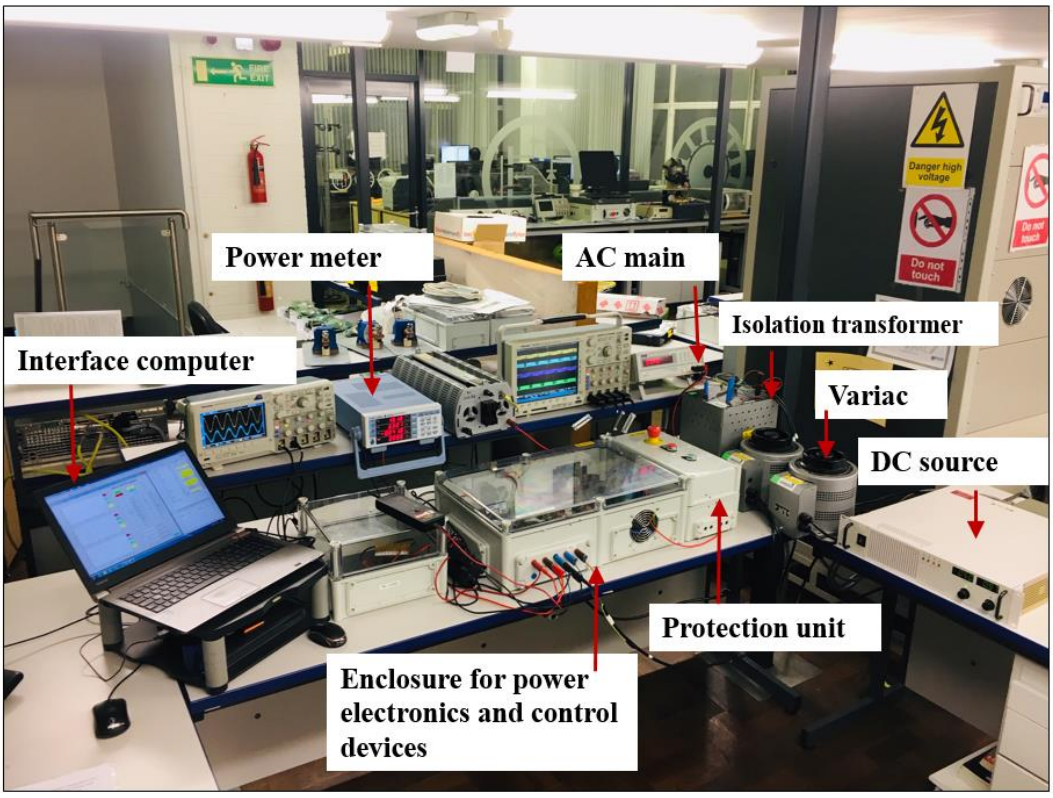

(a)

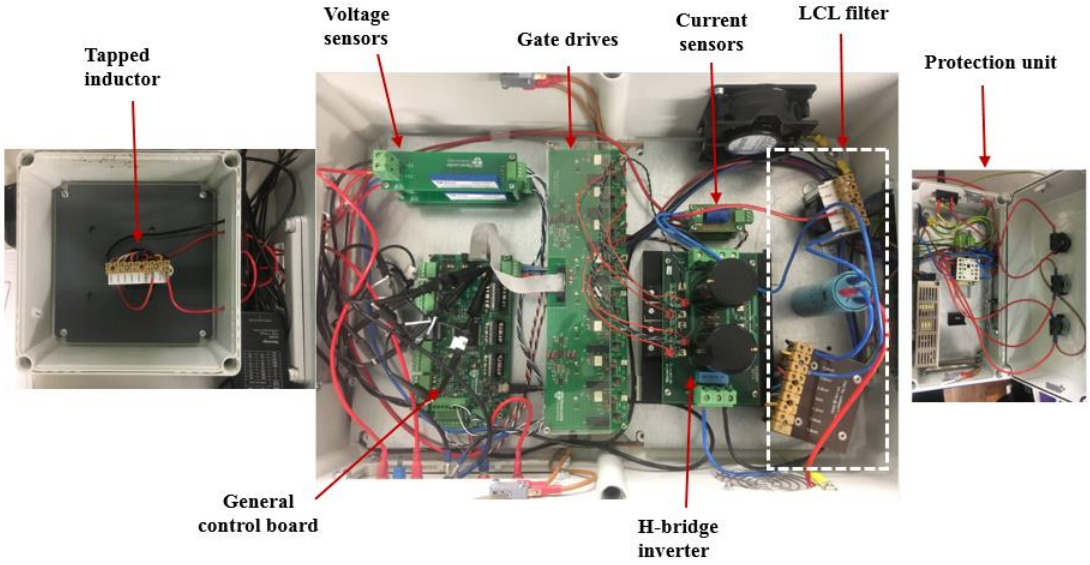

(b)

Figure 6-2 a. Overall experimental system set-up, b. Internal layout of inverter and protection unit enclosures.

Table 9 Parameters of the practical work

Parameters		
Abbreviation	*Nomenclature*	*Value*
P_n	*Nominal Rated Power*	*200W*
V_{DC}	*DC link Voltage*	*100V*
V_g	*Grid Voltage*	*45V*
C_d	*DC Capacitor*	*2200μF*
L_1	*Inverter Side Inductor*	*0.6mH*
L_2	*Grid Side Inductor*	*0.2mH*
C_f	*Filter Capacitor*	$10\ \mu F$
L_g	*Grid Inductance*	*0.1-0.8mH*
f_s	*Switching Frequency*	*20 kHz*
T_s	*Controller Sample Time*	$5 \times 10^{-5} s$

6.3 H-bridge inverter module

Figure 6-3 shows the module of the H-Bridge inverter along with its schematic circuit diagram. The module is made up of a PCB board which consists of a positive and

negative DC link connection. The link is connected in parallel to two off-electrolytic capacitors rated 600V DC and 2200μF each to reduce low frequency ripples on the DC link. For the minimisation of high frequency components, a 150nF polyester film capacitor is connected in parallel across the DC link for filtering purposes. The single-phase inverter is made up of four switches of CMF20120D silicon carbide power MOSFETs with integrated freewheeling diodes. The switches of the inverter are driven by the gate drive with the PWM signals provided by the microcontroller.

Silicon carbide devices are preferable for many power electronics applications due to their advantageous over the other semiconductor devices in terms of switching and conduction losses as well as of thermal conductivity. These benefits ensure higher system efficiency and reduced cooling requirements and allow high switching frequencies to be implemented [138].

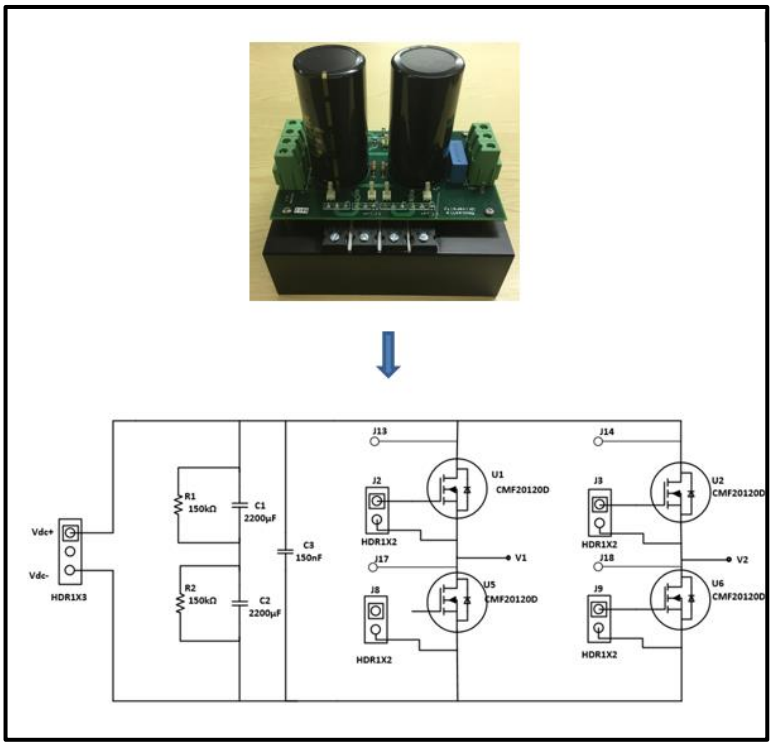

Figure 6-3 Module of experimental H-bridge inverter

The output of the inverter is connected to the variac via the designed LCL filter whose parameters are determined in the same way as that used for the simulation module. Moreover, two voltage sensors are employed one being placed at the point of common coupling and the other on the grid side, while the current sensor is placed on the inverter side of the LCL filter.

6.4 TMS320F377D digital signal processor

The control scheme of the PV grid-connected inverter in this research is implemented on a general control board (GCB) which shown in Figure 6-4. The board was designed and developed in the electrical power lab within Newcastle University based on the Texas Instruments TMS320F377D digital signal controller. It is a 200MHz dual-core processor which is useful for power electronics-based applications such as inverter control. Each of the two CPUs is associated with a 32-bit control low accelerator (CLA), which is a floating-point processing unit that runs at the same clock frequency as the CPU. In addition to the CLA, both CPUs contain another two computational accelerators in the Viterbi Complex Math Unit (VCU) and the Trigonometric Maths Unit (TMU). These mainly important to speed up various numerical calculations. Moreover, the general control board has four 12-bit analogue to digital converters (ADCs) and three buffered 12-bit digital to analogue converters (DACs).

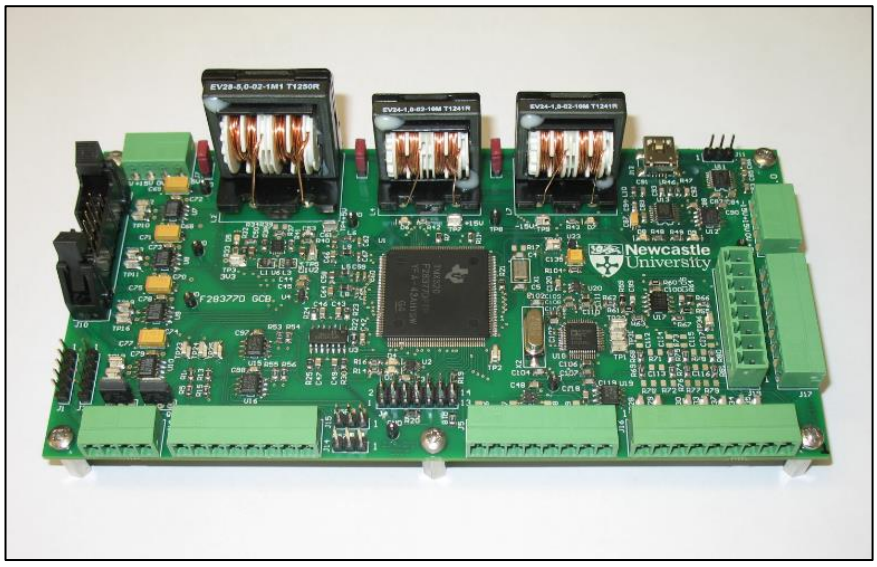

Figure 6-4 TMS320F377D general control board

6.5 Interface and real-time control

The general control board is first interfaced with the gate drive board to provide the PWM signals from the DSP. The general control board is then interfaced with the host PC via a JTAG emulator for real-time control and data transfer. It is worth noting that only one core from the dual-core processor is used for the control algorithm of the

practical system; however, the benefit of using the F2377D is still significant compared to other processor such as TMSF2335, based on its maths accelerators and extra peripheral functions. For the control algorithm to be executes, two software suites are implemented in the host PC: the code composer studio software CCS.v6, where the main control code is written in the C-language; and Matlab software in which the graphical user interface (GUI) code is written.

The execution of the GUI code creates a graphical interface that can be used with the F28377D DSP for monitoring and a high level of real-time control. In practice and during real-time operation, the GUI can be programmed to update or transfer the control demand to the DSP, such as retuning the controller gains; activating or deactivating the PWM or displaying the data collected from the store arrays. A screenshot example of the GUI is presented in Fig 6-5. Finally, current and voltage props are used for the real-time monitoring of the voltage and current signals of interest.

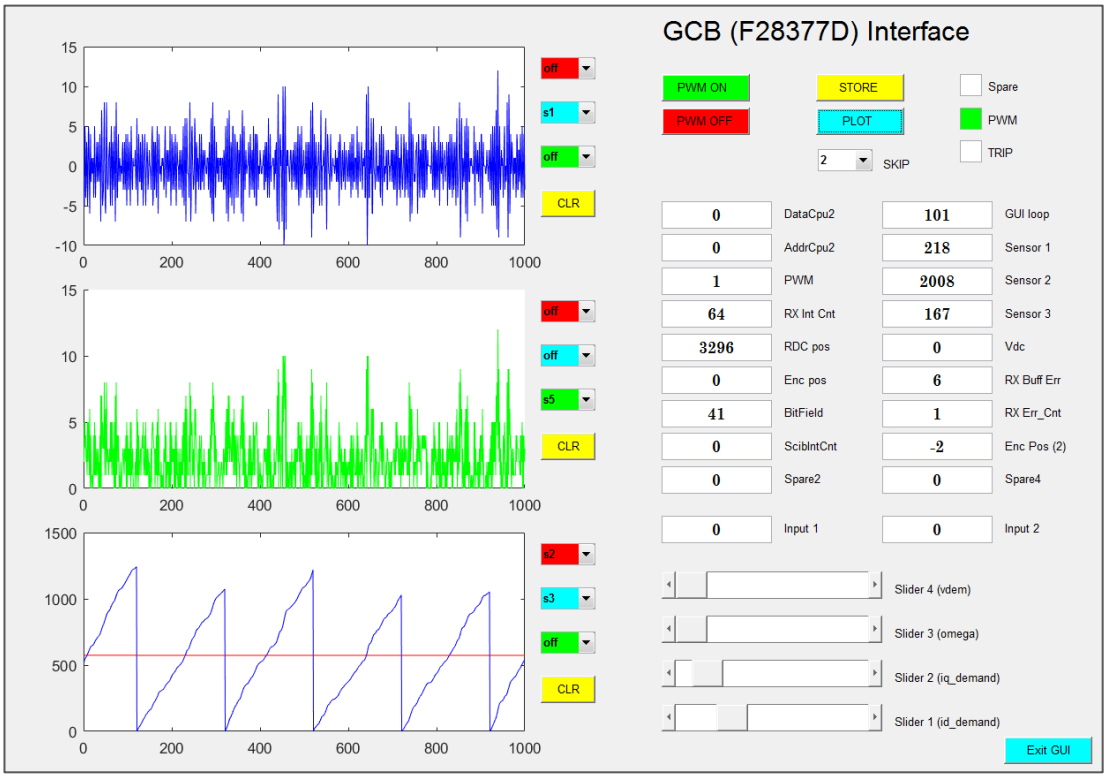

Figure 6-5 Matlab GUI for real-time control

6.6 Practical implementation of adaptive PR controller

The proposed adaptive control algorithm in this research is implemented in the DSP based on the conventional PR controller. The algorithm also includes a digital band-bass filter for the purpose of resonance detection, followed by a chain of statistical signal processing. A block diagram of the proposed adaptive control is shown in Figure 6-6. As can be noticed, the voltage sensor placed at the PCC provides the digital band-pass filter with the PCC voltage signal. The filter then extracts the harmonic components around the resonance frequency which are linked to the variation in grid inductance. Figure 6-6 also illustrates that the controller parameters K_P and K_R are updated from the data stored in the pre-built look-up table.

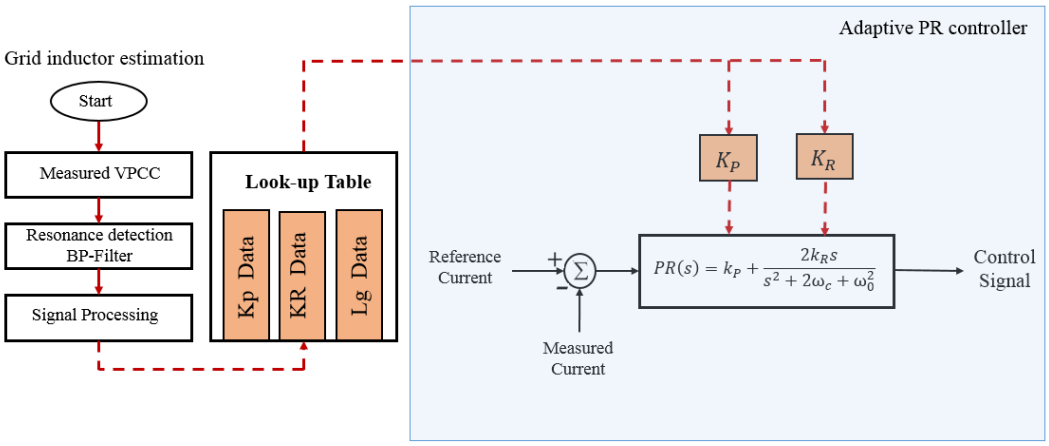

Figure 6-6 Block diagram of the proposed adaptive control implemented in the DSP

6.7 Phase locked loop PLL for unity power factor operation

Unity power factor control is an important control aspect that is required in a typical design of the grid-connected PV inverter to ensure real power injection into the distribution network [139]. More specifically, the current produced from the inverter needs to be in phase with the grid voltage. This can be accomplished by generating a voltage at the output of the inverter bridge with the same angle as the network grid voltage, which in this case is the PCC voltage, and in this way the voltage generated can overcome the effect of the voltage drop and phase shift caused by the inductive

reactance of the LCL filter. Many techniques have been described in the literature such as the phase locked loop technique PLL [140], zero-crossing detection [141], frequency locked loop [142], recursive weighted least-square [143] and discrete Fourier transform techniques [144].

In this research, a power PLL-based (pPLL) algorithm is selected due to its robust performance and ease of implementation. It is a closed-loop feedback control system which synchronises the output current from the inverter bridge in frequency as well as in phase with the grid voltage. A schematic diagram of the power PLL is depicted in Fig 6-7 which, as can be seen, shows that the algorithm is composed of three main parts: the phase detector (PD), loop filter (LF) and voltage control oscillator (VCO). For the PD, the pPLL uses a sinusoidal multiplier along with a low-pass filter to emulate an active power calculation unit $\overline{P}$.

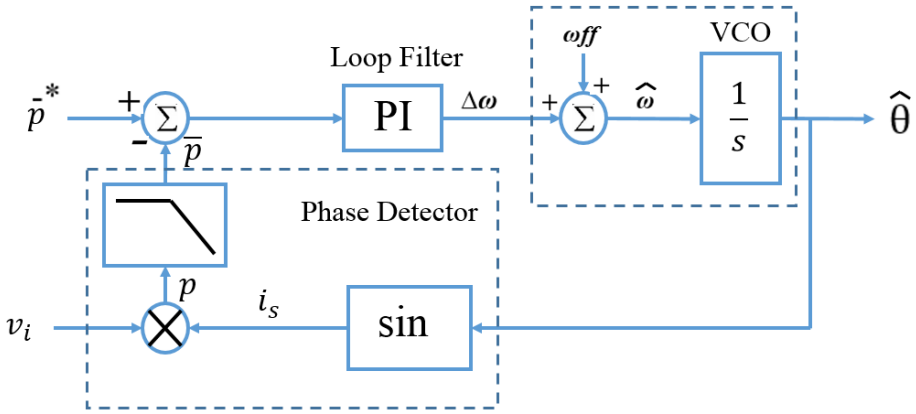

Figure 6-7 Closed-loop feedback control of single-phase pPLL

The friction power resulting from the sinusoidal multiplier is given in equation 6.1:

$$P = v_i i_s = V \cos\theta \ \sin\hat{\theta} \tag{6.1}$$

Rearranging equation 6.1 by applying the product-to-sum trigonometric function, yields:

$$P = \frac{V}{2}\sin(\hat{\theta} - \theta) + \frac{V}{2}\sin(\hat{\theta} + \theta) \quad (6.2)$$

If the mean $\overline{P}$ is equal to zero, then the fictitious current, i_s will go in the quadrature position with respect to the input voltage v_i. In this satiation, the real value of (θ), and the estimated value ($\hat{\theta}$) of the voltage angle will be equalized. If the mean $\overline{P}$ was not zero, than it will be controlled by the PI controller to be zero. The next step in the VCO is to add the output from the PI controller to the nominal value of the grid angular frequency (ωff), which yields the grid angular frequency ($\hat{\omega}$). Finally, the grid voltage angle can be extracted by integrating the obtained grid angular frequency

In the practical work, the pPLL algorithm was implemented in the control algorithm within the CCS and executed in the DSP. The PI controller parameters are set to 100 and 40 for the proportional and integral gains respectively. The experimental result of the grid current and voltage synchronisation is shown in Fig (6-8).

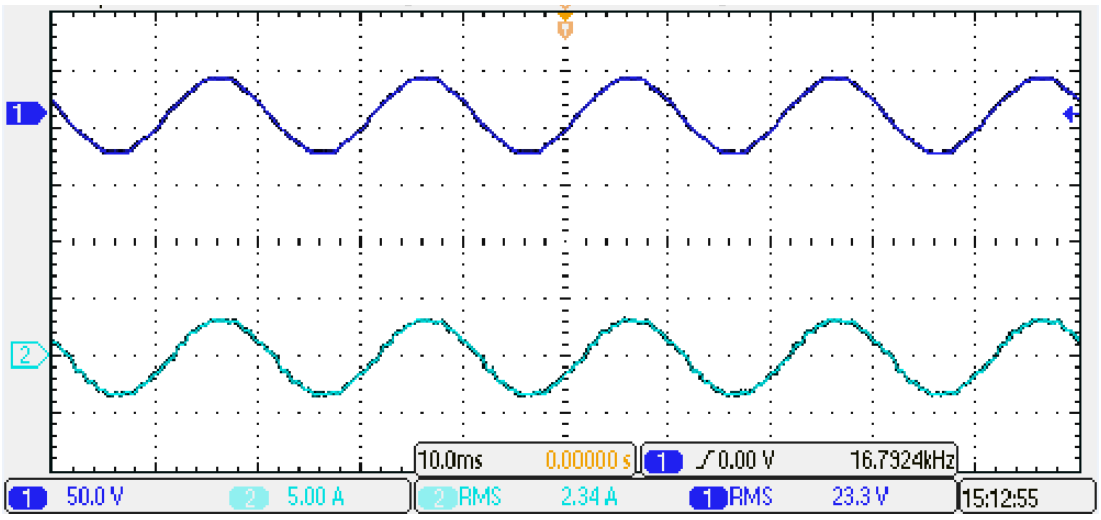

Figure 6-8 Injected grid current in phase with the grid voltage

6.8 Protection circuit of the practical system

For optimal operation and security, the test rig is provided with a protection circuit as shown in Fig 6-9. The system is enclosed in a cage and earthed to prevent any accidental contact while the test is running. The cage is equipped with an emergency stop button to isolate the system in case of emergency. In addition, the safety cage is equipped with a start-stop button via a contractor for the safe operation of the DC power supply. The cage itself is provided with four micro-switches for system isolation in case the cage is opened. Other metal enclosures which contain the isolation transformer and variac are earthed to prevent any possible contact with a live terminal. Finally, to prevent any possible electrical shock, all measurement instruments are connected before any voltage or current is applied.

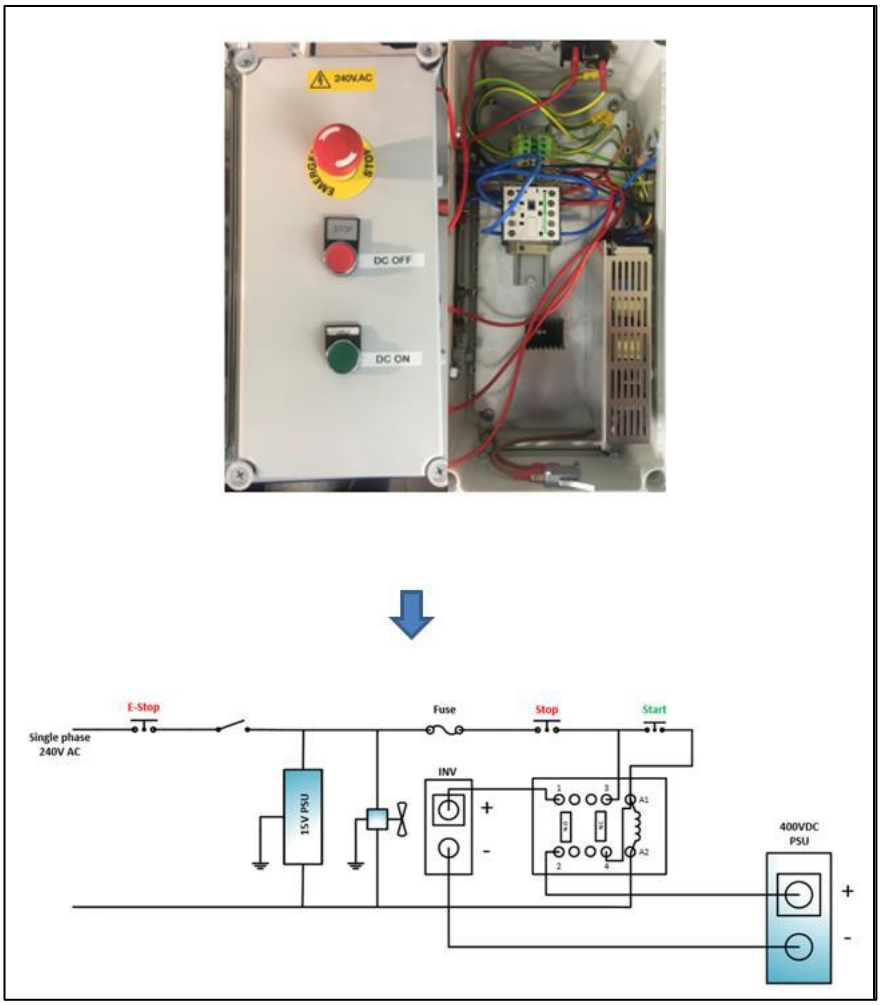

Figure 6-9. Test rig protection circuit

6.9 Chapter summary

This chapter has presented the experimental set-up of the single-phase grid-connected PV inverter system. The design processes have been developed within the electrical power laboratory at Newcastle University. The experimental hardware, including the peripheral components were also described. A description of the control scheme implementation, including unity power factor control along with the proposed adaptive PR controller have been presented. Finally, the chapter has ended with a description of the test rig protection circuit and system isolation.

CHAPTER 7

Experimental and practical results

7.1 Introduction

This chapter provides the experimental results obtained from the test rig of a single-phase grid connected inverter. The first part of the chapter presents investigations on the effect of grid impedance variation on power quality. In particular, the THDs of grid currents (Ig) and PCC voltages (VPCC) are recorder under wide range of grid impedance variation. The change in grid inductance is selected to be in the range of between 0.1 and 0.8mH as the IEC 62727 standard shows that the maximum grid inductance for a single-phase wire is 0.879mH. PI and PR controller are implemented for the control of the injected grid current. The second part of this chapter present a novel techniques for estimating the grid inductance. It includes the practical implementation of a digital band-pass filter along with a statistical signal processing techniques for predicting the change in grid inductance. In order to ease the impact of grid impedance variation, an adaptive control scheme based on PR controller is presented and compared with the conventional PR controller.

7.2 Operation of practical grid-connected inverter systems with control implementation

The functionality of the experimental single-phase grid inverter system is confirmed by its operation. The obtained measurements and waveforms of currents and voltages showed a smooth operation. The power quality of grid current and PCC voltage is investigated via an FFT analysis. Figure 7-1 shows the unipolar PWM for a switching frequency of 20 kHz which used throughout the practical work. In order to operate the system at unity power factor, the grid information is required to synchronise the grid current with the grid voltage. To accomplish this, the grid synchronisation PPLL algorithm has been employed due to its fast response. The experimental results of grid synchronisation which are shown in Figure 7-2 illustrate that the grid current is synchronised with the grid voltage.

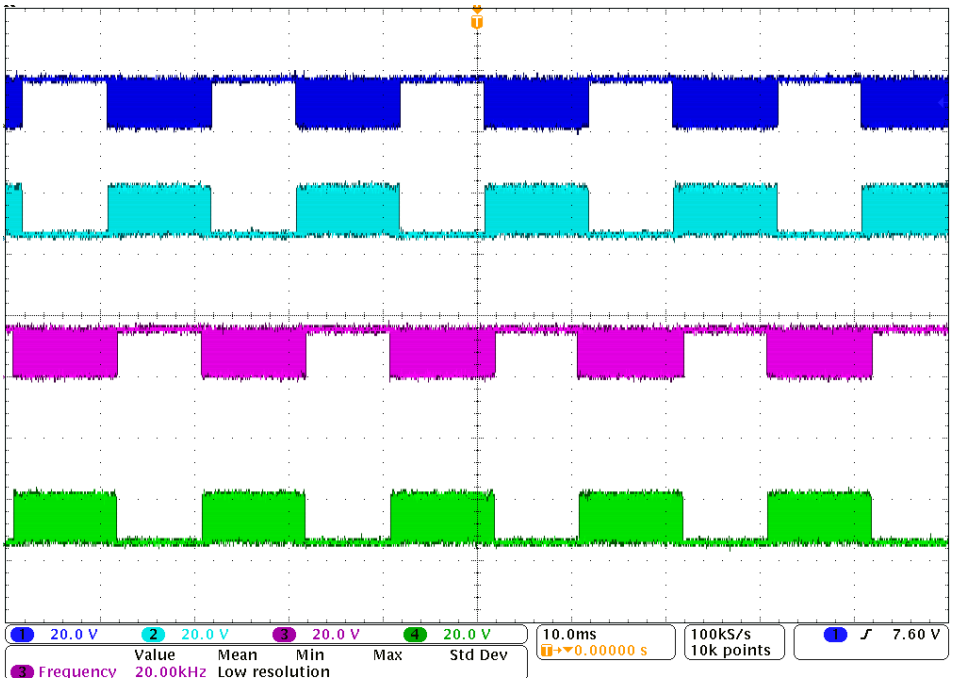

Figure 7-1 Unipolar PWM

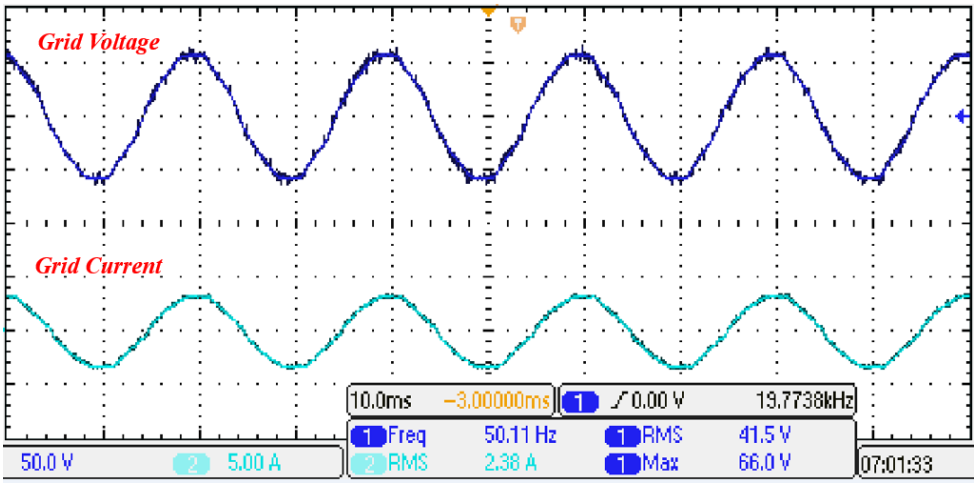

Figure 7-2 Grid synchronisation

7.3 Experimental results with PI controller

Proportional integral PI controller is implemented in order to control the current produced by the inverter before being injected into the grid. The controller gains are carefully tuned as 0.11 and 0.039 for K_p and K_i respectively for a demanded current set to 3Amp. Three waveforms can reflect the performance of the system; the voltage waveform at the PCC (V_{PCC}), the grid current waveforms (L_g) which has to be in phase

with respect to the grid voltage and the output voltage waveform from the inverter. Figure 7-3 shows the three mentioned waveforms at unity power factor. It can be noticed from the figure that the output voltage from the inverter is represented by the 50V unipolar PWM voltage pulses with the same polarity as the grid current for both sequences.

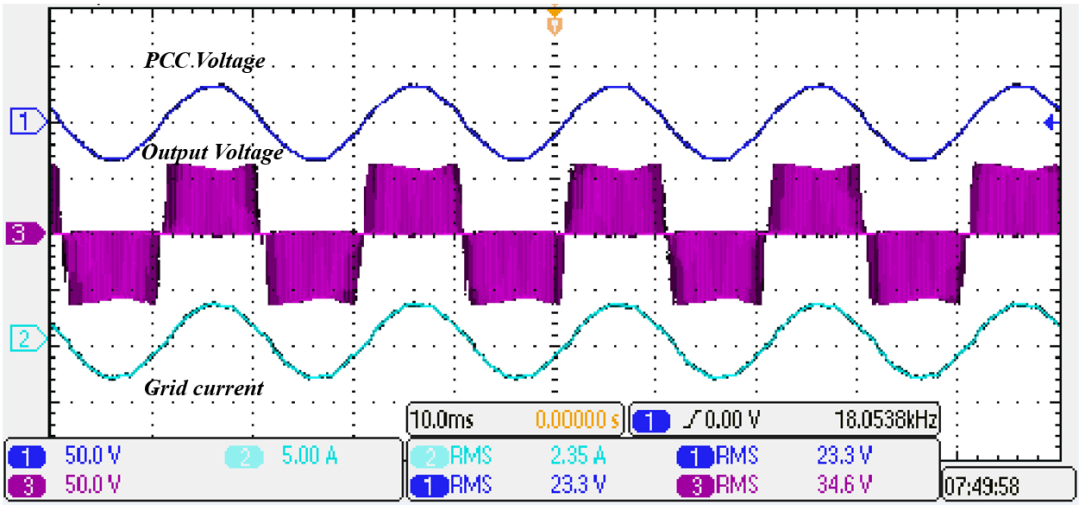

Figure 7-3 System operation with PI controller

7.3.1 Performance of THD% under grid inductance variation with PI controller

One of the most important power quality index for grid-connected PV system is the current distortion level. These distortion levels has to be kept under the limits specified by local and international standards to avoid adverse effects on equipment that connected to the grid. In order to investigate the effect of grid inductance variation on the harmonic performance of grid current and PCC voltage, FFT analysis has been carried out to grid current and PCC voltage waveforms using Matlab/Simulink. These waveforms are transmitted from the microprocessor in the GCB to Matlab workspace by the GUI.

The experimental VSI system was interfaced to the utility grid via a tapped inductance in the range of from 0.1 to 0.8 mH which emulates the grid inductance. This range of inductances is selected because they are given by the standard of IEC 60725 as the typical inductances of the distribution grid. The emulated grid inductor was inserted between the LCL filter and the variac. Since the current and voltage measurements are

taken before the additional grid inductance, then from the output of the VSI this inductance is seen as a part of the grid and is decoupled from the LCL filter. The harmonic profile of the grid current and the PCC voltage at different values of grid inductance during the experimental work are shown in Figure 7-4 and Figure 7-5 respectively.

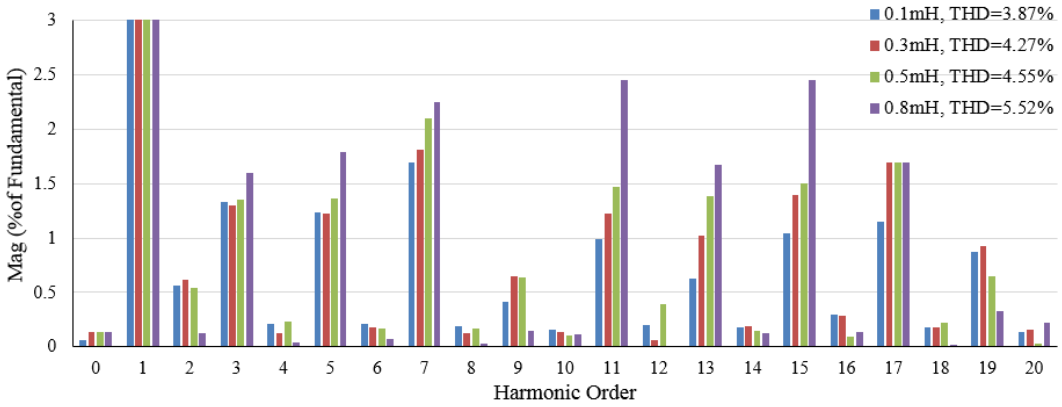

Figure 7-4 Effect of Grid inductance variation on THD of grid current with PI controller, K_P=0.11 and K_i=0.039

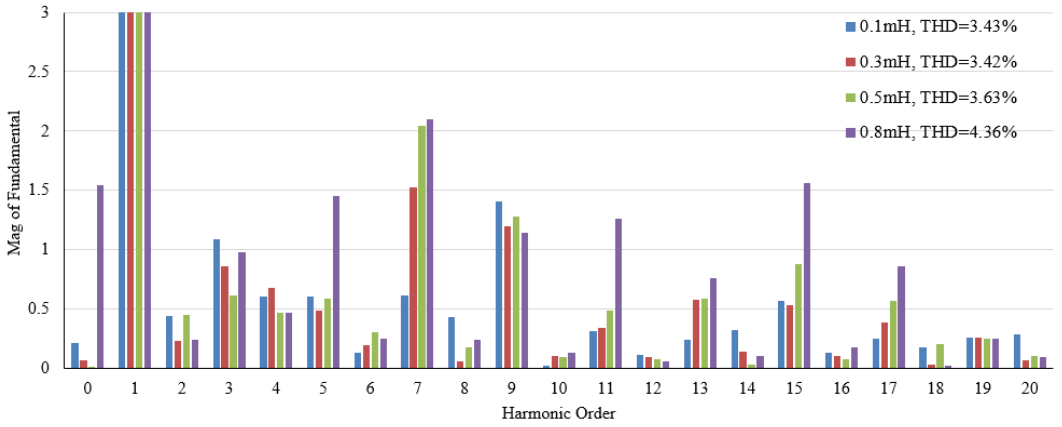

Figure 7-5 Effect of Grid inductance variation on THD of PCC voltage with PI controller, K_P=0.11 and K_i=0.039

As can be seen from the figures, the frequency spectrum of the grid current with the lowest THD is recorded in the case of the smallest grid inductance (0.1mH) with 3.87%, once this inductance increases the THD of grid current significantly increases. The frequency spectrum also shows that THD of grid current has jumped by more than 1% when the grid inductance has been changed from 0.3mH to 0.5mH and the same

incremental percentage for the change from 0.5mH to 0.8 mH. It is also can be noticed that in the case of 0.1mH all harmonic orders have a magnitude less than 1.5% apart from the 7th harmonic order which was 1.24% however they all haven't exceeded the limits of current harmonic distortion for odd harmonics that are specified by standards such as IEEE 929 and IEC 61727. In the other cases of grid inductances 0.3mH, 0.5mH and 0.8mH these standards have been exceeded at the 17th harmonic order where all magnitudes were more than 1.5% (The limit for odd harmonic is < 2%). Although such distortion is not significant in the first three inductances it can still reduce the power quality of the injected current. The highest level of THD was recorded in the case of 0.8mH with 5.52% which is not acceptable by the mentioned IEEE and ICE standard which requires that the THD of the injected grid current must be less than 5% for PV grid-connected system as depicted in the harmonic current distortion limits given in table 10.

Table 10 Harmonic current distortion limits of PV systems

Standard Number		***IEC 61727***	***IEEE929***
Odd Harmonic	$3 \leq h \leq 9$	$< 4.0\%$	$< 4.0\%$
	$11 \leq h \leq 15$	$< 1.5\%$	$< 2.0\%$
	$17 \leq h \leq 21$	$< 4.0\%$	$< 1.5\%$
	$23 \leq h \leq 33$	$< 0.6\%$	$< 0.6\%$
Even Harmonic	$2 \leq h \leq 8$	$< 1.0\%$	*Less than 25% of the odd harmonics limits*
	$2 \leq h \leq 8$	$< 0.5\%$	
Total Harmonic Distortion THD		$< 5\%$	$< 5\%$

Figure 7-5 shows that the harmonic profile of the voltage signal at the PCC for all harmonics order between the DC and the 20th order. It is obvious from the figure that the THD of PCC voltage has also increased by the increase in the grid inductance but the incremental rate was not as significant as that of grid current. The THD of PCC voltage with a grid inductance of 0.1mH was 3.43% and then start to rise gradually affected by the increase of grid inductance to reach 4.36% for a grid inductance of 0.8mH. In addition, with a close look at both figures it can be observed that the

magnitude of the grid current harmonics are proportional to the magnitude of PCC voltage harmonics, for instance, the magnitudes of the 7^{th}, 11^{th}, 13^{th}, 15^{th} and 17^{th} harmonic orders of the grid current have a similar incremental rate as their corresponding 7^{th}, 11^{th}, 13^{th}, 15^{th} and 17^{th} harmonic orders of the PCC voltage. This is can be linked to the change in the magnitude of voltage at the output of the inverter.

Figure7-6 shows the relationship between the grid inductance variation and THD of grid current and PCC voltage. According to this figure, the THD of grid current has increased with the increase of grid inductances while the THD of PCC voltage

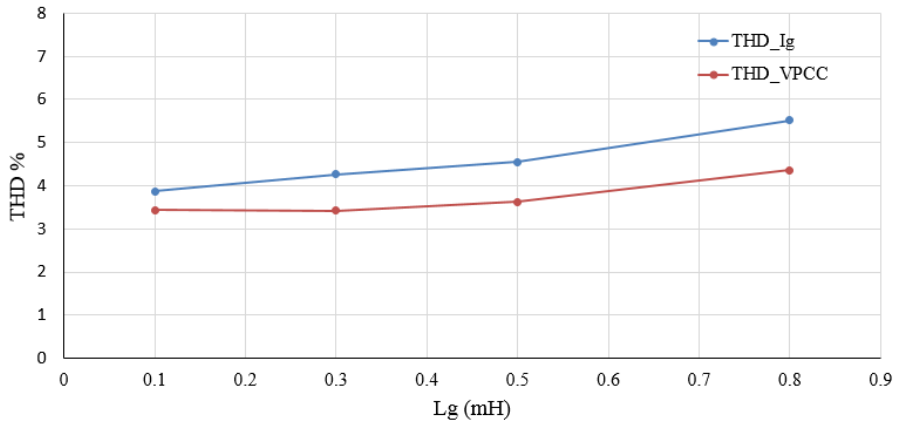

Figure 7-6 Variation of current and PCC voltage THD with varied Lg under PI controller

7.4 Experimental results with PR controller

Proportional resonance PR controller has been also implemented for the regulation of the grid current during the experimental work. Since the tracked signal is a sinusoidal then the PR controller is more suitable than the PI controller in terms of eliminating the steady state error and rejecting the disturbances. During the practical experiment the parameters of the PR controller were carefully selected as K_P=0.129, K_R=106, ω_c= 5 rad/sec for the same current demand as that of PI controller. Figure 7-7 shows three waveforms; the voltage waveform at the PCC (V_{PCC}), the grid current waveforms (L_g) and the output voltage waveform from the inverter. These waveforms represent the operational performance of the experimental single-phase grid connected inverter. It can be noticed from the figure that the system is working at unity power factor as the grid current is in phase with respect to the grid voltage. However, the experimental

current waveform has more distortion levels compared with the current waveform which was obtained in the simulation results. This is because of the non-ideal characteristics of the practical VSI.

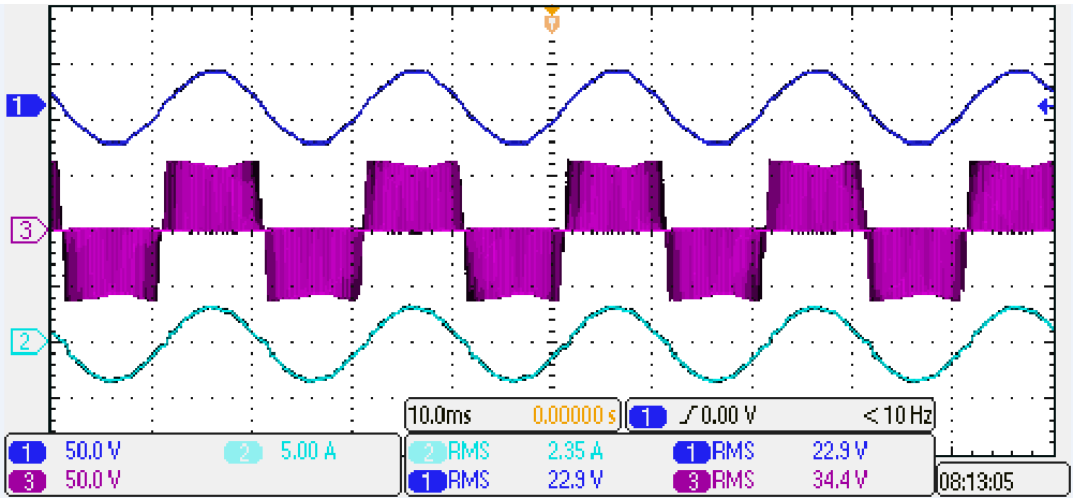

Figure 7-7 System operation with PR controller

7.4.1 Performance of THD% under grid inductance variation with PR controller

The investigation on the impact that the variation of grid inductance has on the power quality of the injected grid current and PCC voltage with PR controller has been carried out with the same way as that of PI controller in section 7-4-2. By applying the FFT analysis, the harmonic profile of the grid current and the PCC voltage at different values of grid inductance during the experimental work are shown in Figure 7-8 and Figure 7-9 respectively.

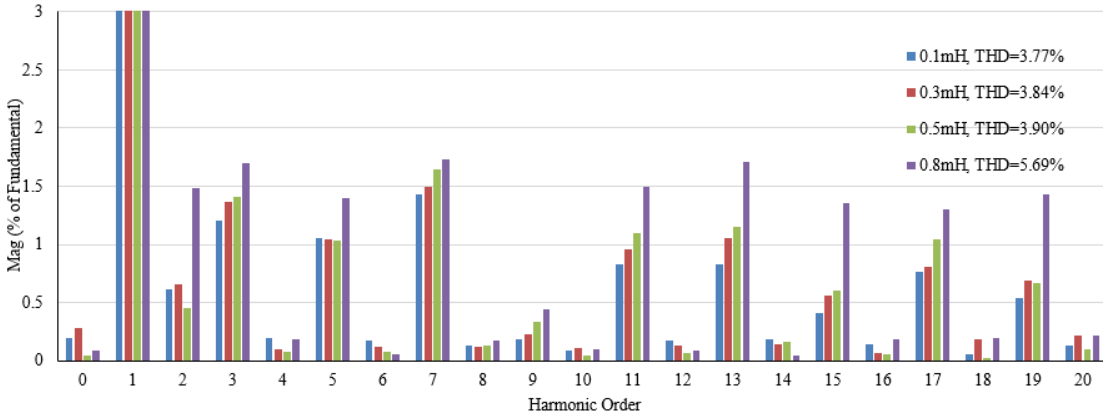

Figure 7-8 Effect of Grid inductance variation on THD of grid current with PR controller, K_P=0.129, K_R=106, and ω_c=5 rad/sec

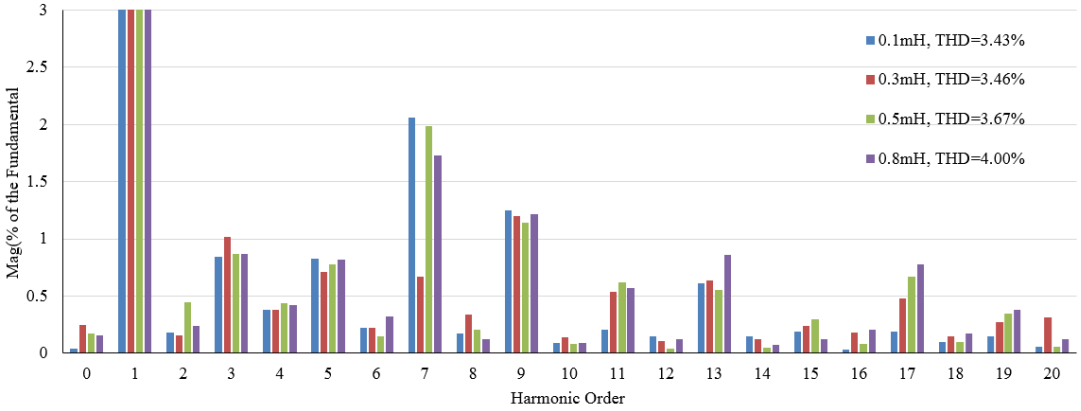

Figure 7-9 Effect of Grid inductance variation on THD of PCC voltage with PR controller, K_P=0.129, K_R=106, and ω_c=5 rad/sec

It is obvious form both figures that the harmonic performance of grid current and PCC voltage is similar to the harmonic profile when the grid current was controlled with the PI controller in which the grid inductance variation has influenced the THD of both waveforms. In particular, the THD of grid current has increased from 3.77% for a grid inductance of 0.1mH to 5.69% when the grid inductance has been changed to 0.8mh. Under the same conditions, the THD of PCC voltage has also increased

Figure7-10 shows the relationship between the grid inductance variation and THD of grid current and PCC voltage. According to this figure, the THD of grid current has increased sharply with the increase of grid inductances while the THD of PCC voltage has experienced a gradual increase.

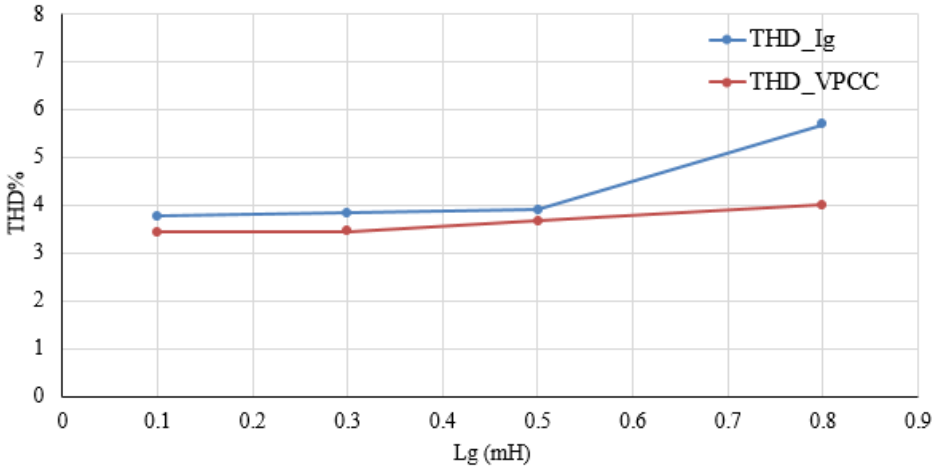

Figure 7-10 Variation of current and PCC voltage THD with varied Lg under PR controller

A comparison between the PI controller and PR controller in terms of THD performance of grid current and PCC voltage with varied grid inductance are given in Figure 7-12. Both controller meet the standard requirement given earlier in table10 for inductance values less than 0.5mH. However, the standard has been exceeded when the grid inductance is 0.8mH. The performance of PR controller is found to better than that of PI controller for all the examined inductances apart from the case of 0.8mH where the THD of grid current was slightly bigger than that of the PI controller. This can be alleviated by proper tuning of the controller parameters or adding the harmonic compensation to the structure of the PR controller.

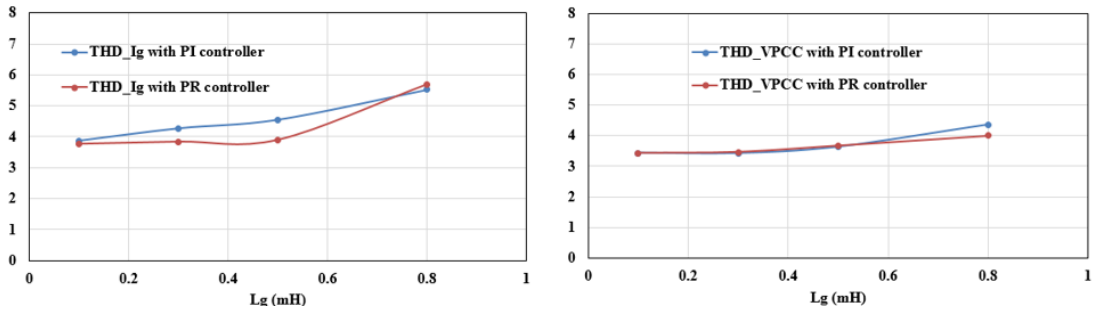

Figure 7-11 comparison of THD performance of grid current and PCC voltage between PI and PR controllers with varied grid inductance

7.4.1 Effect of changing the controller gains on THD performance.

The tuning of controller parameters during the simulation work has been achieved by partial swarm optimisation algorithms as described in chapter four. The computational time of this algorithm is quite long which make it difficult to be implemented on line during the practical experiment. Nevertheless, the algorithm is found to be useful to give the range of controller parameters, by knowing this, the gains were easier to be determined. Herein, the effect of changing the proportional gain on the harmonic performance for both controller techniques are investigated. The grid inductance between the grid and the VSI is set to 0.1mH, and the THD of grid current is obtained for possible maximum and minimum value of K_P. In the case of PR controller was varied from 0.04 to 0.14 which was the maximum value for the system to be controlled. Beyond this value the system was unstable at KP=0.16. While in the case of PI controller KP was varied from 0.02 to 0.15 and at 0.16 the system was unstable. The variation in THD of grid current under both control schemes with varied KP is given in Figures 7-12 for the PI controller and 7-13 for the PR controller.

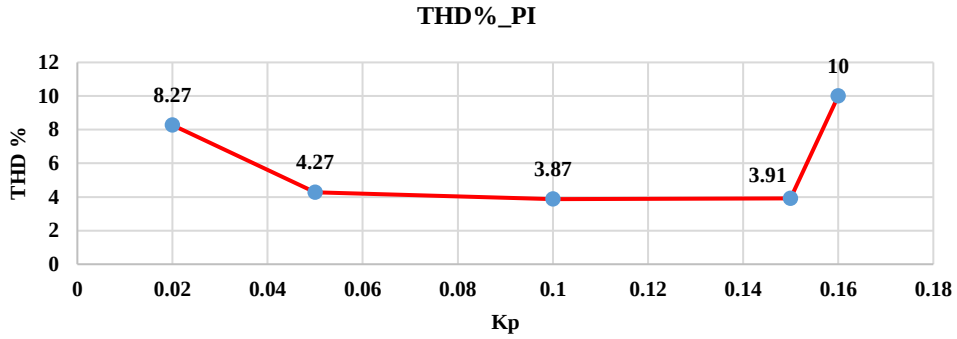

Figure 7-12 Variation of THD of grid current with K_P under PI controller

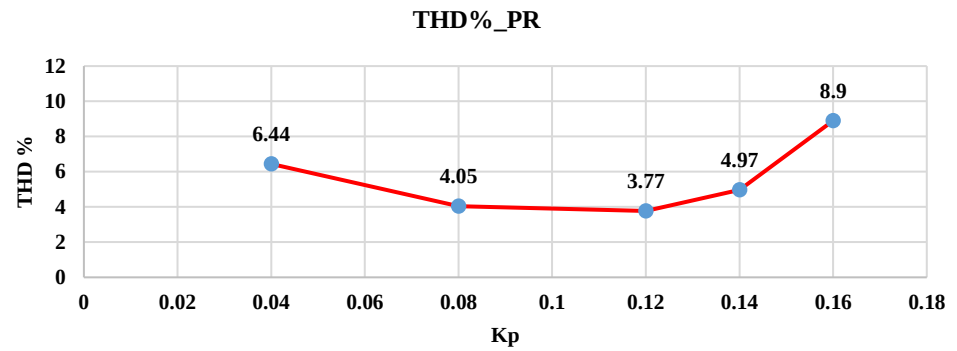

Figure 7-13 Variation of THD of grid current with KP under PR controllers

As can be seen from both figures, changing the values of KP has a direct impact on the harmonic performance of grid current. The lowest achievable level of grid current THD is 3.87% with K_P=0.1 in the case of PI controller, while with PR controller the lowest THD was 3.77 with K_P=0.12. In addition, the figures show that the harmonic performance of grid current with PR controller is better that that of PI controller due to poor action associated with the integral part of PI controller. It is worth mentioning out that when the value of K_P exceeds the maximum or the minimum of the plotted values the THD of the grid current exceeds the standard requirement and the system moves toward instability as illustrated in figure 7-14 and 7-15.

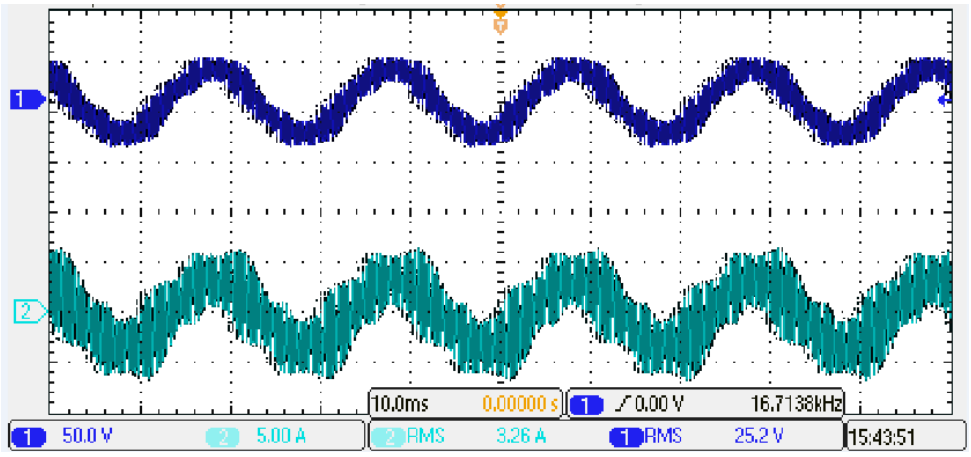

Figure 7-14 grid current and PCC voltage waveforms with K_P=0.17, PI controller

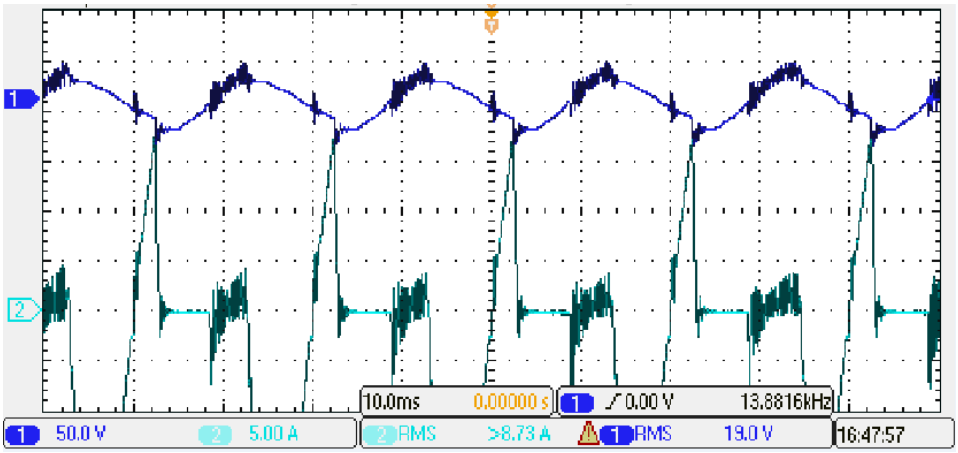

Figure 7-15 grid current and PCC voltage waveforms with K_P=0.189, PR controller

According to the experimental results which obtained from investigating the effect of grid inductance variation and the effect of varying the proportional gain, it can be concluded that, the THD of grid current can be reduced by reducing the effect of grid inductance variation in the one hand, and by proper tuning of the controller gain on the other hand. From this prospective, the next section presents a simple and effective grid impedance estimation technique which can provide the controller by an estimated and readable grid inductance. Based on this estimated value the controller can adapt itself to the change in grid impedance by retuning its parameters.

7.5 Practical implementation of adaptive PR controller

Practical implementation of the proposed adaptive scheme of digital PR controller is presented in this section in order to validate the simulation results given earlier in chapter four. The adaptive scheme is based on a grid impedance estimation method that utilizes a high-order band-pass filter and a chain of statistical signal processing techniques in order to provide the controller with the information of grid inductance variation. The design process of the digital band-pass filter in the practical experiment is the same as that of the simulation work apart from the determination of resonance frequency range. During the simulation work the region of the system's resonance frequency was based only on the reactive components of the LCL filter and FFT analysis for the voltage signal at the PCC. Unfortunately, this can't be the case in practical as the overall grid impedance is not negligible due to the existed isolation transformer impedance and the variac impedance.

7.5.1 Estimation of grid inductance variation

As the grid inductance can be considered as part of the LCL filter, the change in their values will results in changes in the resonance frequency of the LCL filter. Based on this fact, the resonance frequency is a beneficial information for estimating the value of grid inductance. The method proposed in this research is to exploit the resonance frequency in order to detect the change in grid inductance and thus used in optimising the current controller operation. It employs a high-order digital band-pass filter to extract the harmonic components around the resonance frequency from the voltage waveform at the PCC. To accomplish this, the knowledge of the resonance frequency

range is essential in order to design the bandwidth of the digital filter. It is possible to excite the resonance of the LCL filter by slightly increasing the proportional gain of the current controller to the point where the closed-loop reach the border of the stability region. During the practical experiment the proportional gain has been carefully increased by a step of 10% up to the value in which the system become unstable. The instability operation was kept for 0.2 second in order to ensure the needed resolution which required for the FFT analysis. Figure 7-12 shows the experiment result of resonance excitation, (a) near the border of the stability region and (b) at the border of the stability region.

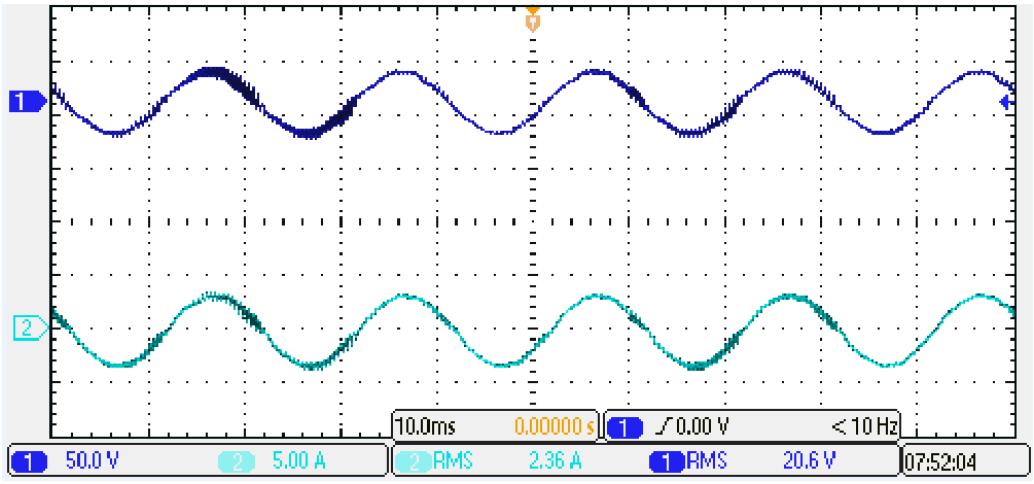

(a)

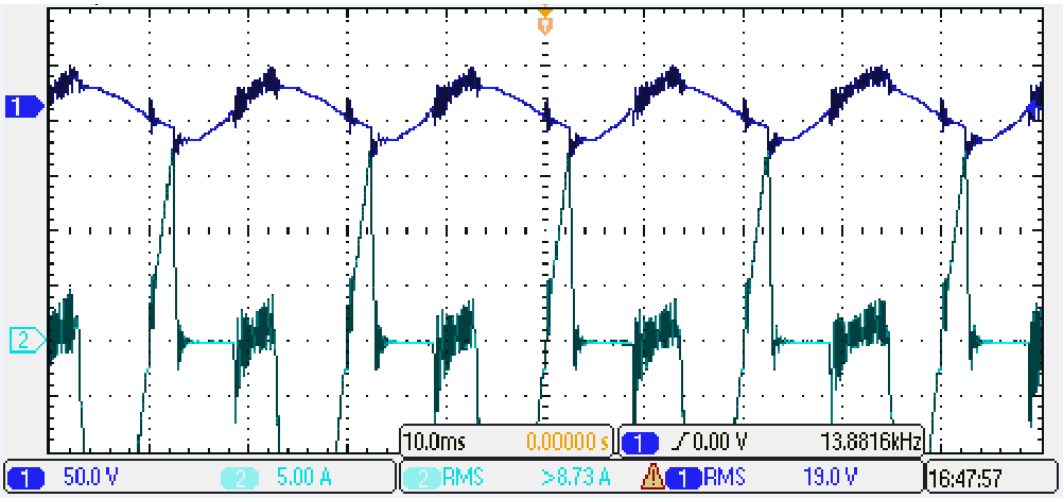

(b)

Figure 7-16 Resonance excitation of the system, (a) near the border of the stability region, (b) beyond the border of stability region

(I demand=3A, VDC=60V, Vac=20V, and K_P=0.189)

Based on the fact that the resonance frequency is changing whenever grid inductance changes, and the considered variation of grid inductance is in the range of between 0.1mH to 0.8mH thus, a practical experiment has been carried out for two values of grid inductance 0.1mH, and 0.8mH in order to determine the exact bandwidth of the required band-pass filter. By carrying out the FFT analysis to the highly distorted signal of the grid current, the resonance frequency was experimentally determined. The harmonic performance of the measured grid current in the case of L_g equal to 0.1mH and 0.8mH are shown in Figures 7-17 and 7-18 respectively. As can be seen from the figure, the resonance frequency is equal to 2600Hz in the case of 0.1mH, while with 0.8mH of grid inductance to resonance frequency is equal to 2150Hz.

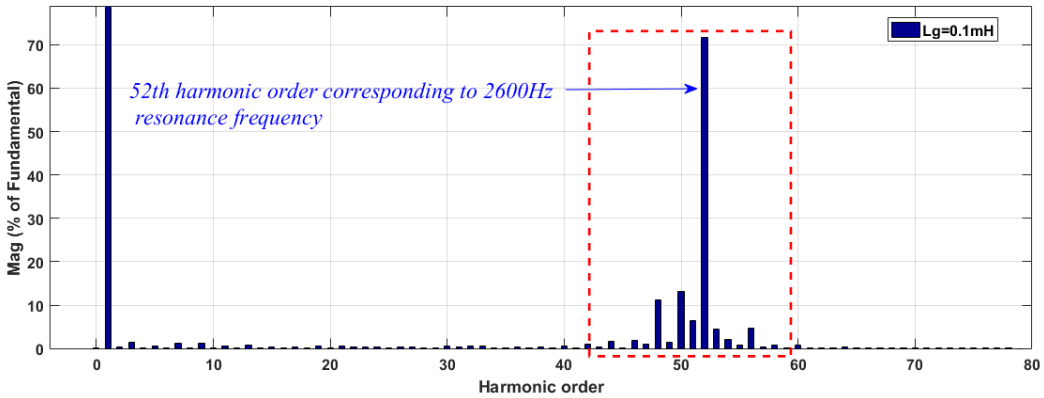

Figure 7-17 harmonic performance of measured grid current in the case of 0.1mH

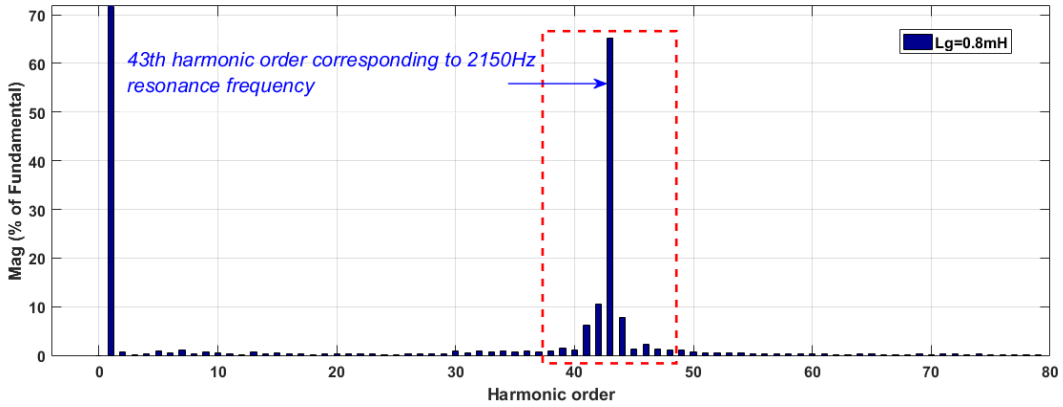

Figure 7-18 harmonic performance of measured grid current in the case of 0.8mH

In addition, the frequency spectrum clearly shows how the resonance frequency peak changed its position following the change in grid inductance. With the knowledge of

the variation range of resonance frequency, the task of designing the band-pass filter with an accurate pass band is remarkably achievable.

7.5.2 Digital band-pass filter for resonance extraction

The design process of the digital band-pass filter in the practical experiment is similar to that followed during the simulation work. However, the bandwidth of the filter has been slightly expanded to take into account the nominal value of grid inductance which include also the variac and isolation transformer. A Matlab code has been developed in order to determine the parameters of the analogue 4^{th} order Sallen-Key band-pass filter as provided in Appendix7. The specifications of the filter are given in table11.

Table 11 Specification of band-pass filter

Specification of Band-pass filter	
Order	*4th*
Passband gain	*25dB*
Centre frequency	*2.2kHz*
Bandwidth	*1kHz*

The obtained transfer functions of the band-pass filter in the *s*- and *z*-domain are given in equation 7.1 and 7.2 respectively. While the corresponding bode diagram is shown in Figure 7-19.

$$G(s) = \frac{1.301s^2}{s^4+1.999e^4s^3+4.624e^8s^3+2.341e^{12}s^2+3.812e^{16}} \tag{7.1}$$

$$G(z) = \frac{1.218z^3-1.4360.781z+0.999}{z^4-2.617z^3-3.155z^2-1.924z+0.5491} \tag{7.2}$$

As can be observed from the bode diagram of the band-pass filter, the passband gain at the centre frequency is magnified to 25dB and thus all harmonic components around the resonance frequency which are typically small in magnitudes will easily captured. While the fundamental frequency is attenuated to -50dB which is corresponded to

0.0032V/V. In addition, the Bode diagram shows a good match in the frequency domain between the discrete and contentious transfer functions of the band-pass filter. The input signal to the digital band-pass filter is the voltage signal at the PCC. The output signal from band pass filter has been captured and analysed by FFT analysis in Matlab in order to assess the filter performance and the filter ability to filter out only the harmonic components within the interested range.

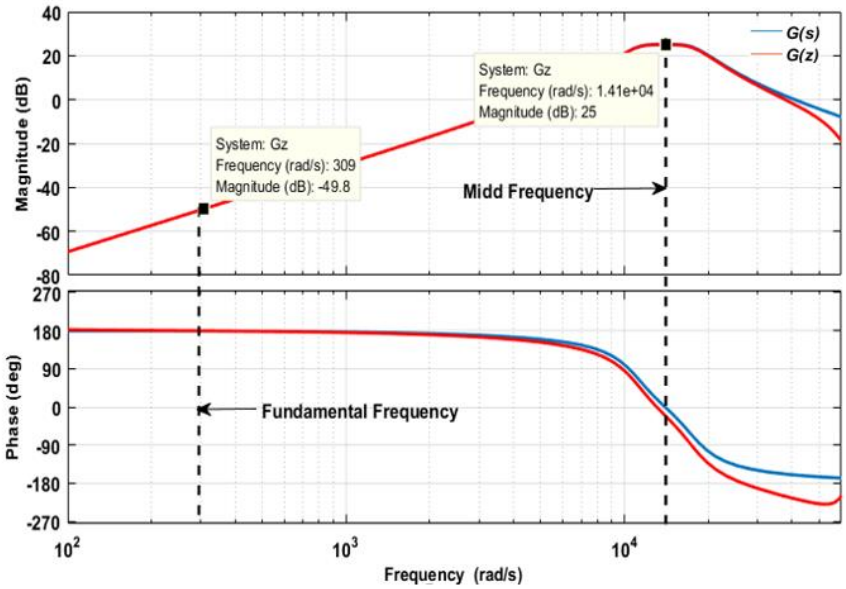

Figure 7-19 Frequency response of Band-pass filter

In the practical experiment the measured data which sensed by the measurement sensors in the GCB are digitally collected by data storage registers. These real data are transmitted from the microprocessor to the Matlab workspace through the general user interface GUI. Once these data are available in Matlab workspace, FFT analysis can be conducted to all measurement such as input and output signals of the digital band-pass filter. It has been demonstrated earlier in section 7.4.1 that the level of harmonic distortions observed on the voltage signal at the PCC is increasing as the grid inductance increase due to the resonance excitation. In addition, the results presented early in section 7.5.1 showed that the position of the resonance frequency changes according to the change in grid inductance therefor, the designed band-pass filter should be assessed in terms of filtering effect and resonance detection at different values of grid inductances. Figures 7-20 and 7-21 show the results of the performance

of the digital filter and the FFT analysis to the output voltages signals at 0.3mH and 0.8mH of grid inductance respectively.

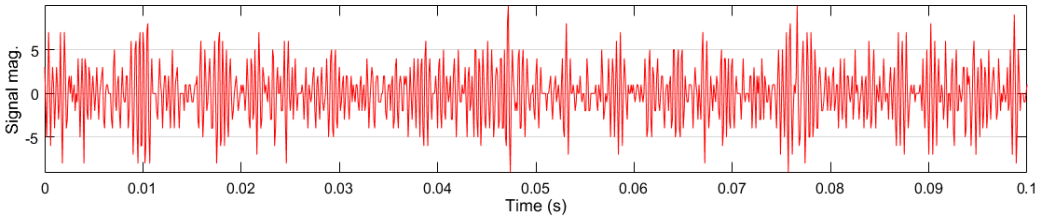

(a)

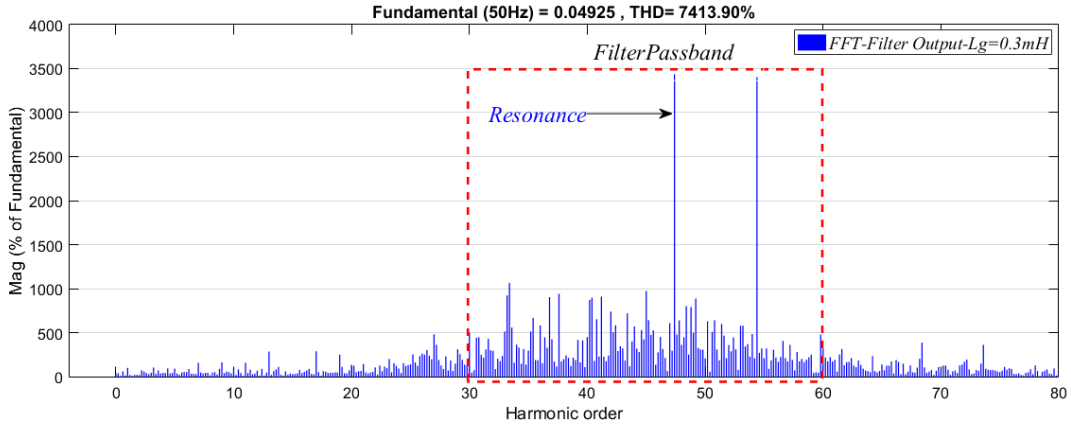

(b)

Figure 7-20 (a) Output voltage signal from the digital band-pass filter, (b) FFT analysis of the output voltage signal from the digital band-pass filter at 0.3mH of grid inductance

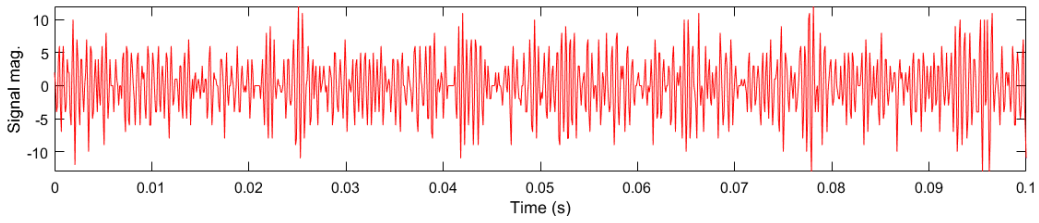

(a)

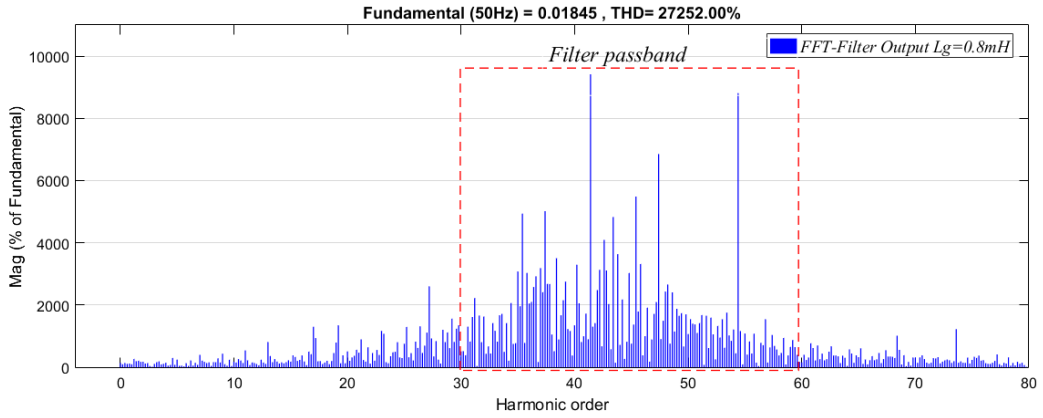

(b)

Figure 7-21 (a) Output voltage signal from the digital band-pass filter, (b) FFT analysis of the output voltage signal from the digital band-pass filter at 0.8mH of grid inductance

As it can be seen from both figures, the designed digital band-pass filter was able to filter out the harmonic components in the form of an oscillation signal within the selected pass-band of the digital filter which in the range of 30^{th} and 59^{th} harmonics as shown in Figures 7-20.(a) and 7-21.(a). Although the output voltage signals from the digital filter under both cases of grid inductance have similar shapes, however, the FFT analysis to the filter output signal in both cases of grid inductance shows a significant difference, for instance, the level of THD in the filter output signal with 0.8mH was almost four times higher than that in the case of 0.3mH of grid inductance, this can be clearly noticed from Figures 7-20. (b) and 7-21. (b). these finding results confirm that the higher the grid inductance the more distortion presents in the PCC voltage. In addition, the finding results confirm that the designed digital band-pass filter has magnified the magnitudes of the harmonic components within the selected bandwidth due to the selected high pass-band gain.

7.6 Design and operation of the adaptive PR APR controller

In order to reduce the effect of grid inductance variation on the harmonic performance of grid current and PCC voltage the PR controller has to be robust against this variation. To accomplish this task, the PR controller needs the information of change in grid inductances in order to retune its parameters according to this change. As demonstrated in section 7-5-2 the digital band-pass filter is able to detect the resonance frequency resulted from the change in grid inductance and hence the controller can be adapted to these variation if the information provided by the digital filter were

readable. However the information provided by the digital filter are in the shape of an oscillating signal as shown in Figures 7-23. (a), and 7-24. (a), which cannot be directly recognised by the current controller. To exploit these information in a beneficial way, a chain of statistical signal processing techniques are employed in the current control loop to provide the PR controller with the information of grid inductance variation. By using this simple techniques, the current controller will not be overwhelmed by undesired complex calculation that associated with other techniques such as FFT function. As it has been deeply explained in chapter five, the signal processing techniques consists of the following analysis: signal rectification, integration and the averaging of the integrated signal obtained from the digital band-pass filter. The schematic diagram of the proposed adaptive technique of APR controller is depicted in Figure 7-22. The variation of grid inductance is determined through the filtering operation and the signal processing chain. The average value obtained from the processing chain is received by a pre-built look-up table which consists of the best values of the controller's gains and their corresponding values of average signals.

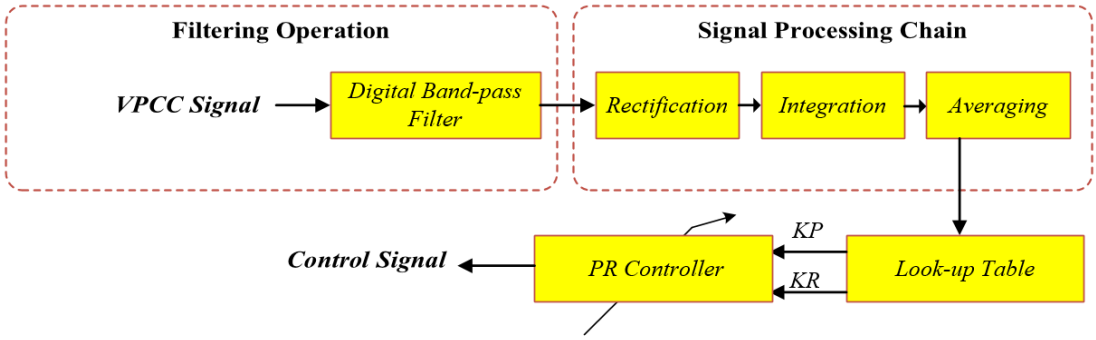

Figure 7-22 Adaptive techniques of PR controller

7.7 Experimental results of filtering operation and signal processing

The digital implementation of the filtering and the signal processing operations has been accomplished by a written c-code within the control platform. The related experimental results are shown in Figures 7-23 and 7-24 for grid inductance of 0.3mH and 0.8mH respectively. As shown in Figure 7-23.a and 7-24.a, the digital band-pass filter has filtered out only the harmonic components around the resonance frequency within the designed pass-band. The output signal from the digital filter is oscillating

along the vertical axis, thus rectification is applied to overcome the negative part of the oscillating signal. The next step in the signal processing is integrating the rectified signal at every control cycle as shown in Figure 7-23.c and 7-24.c.

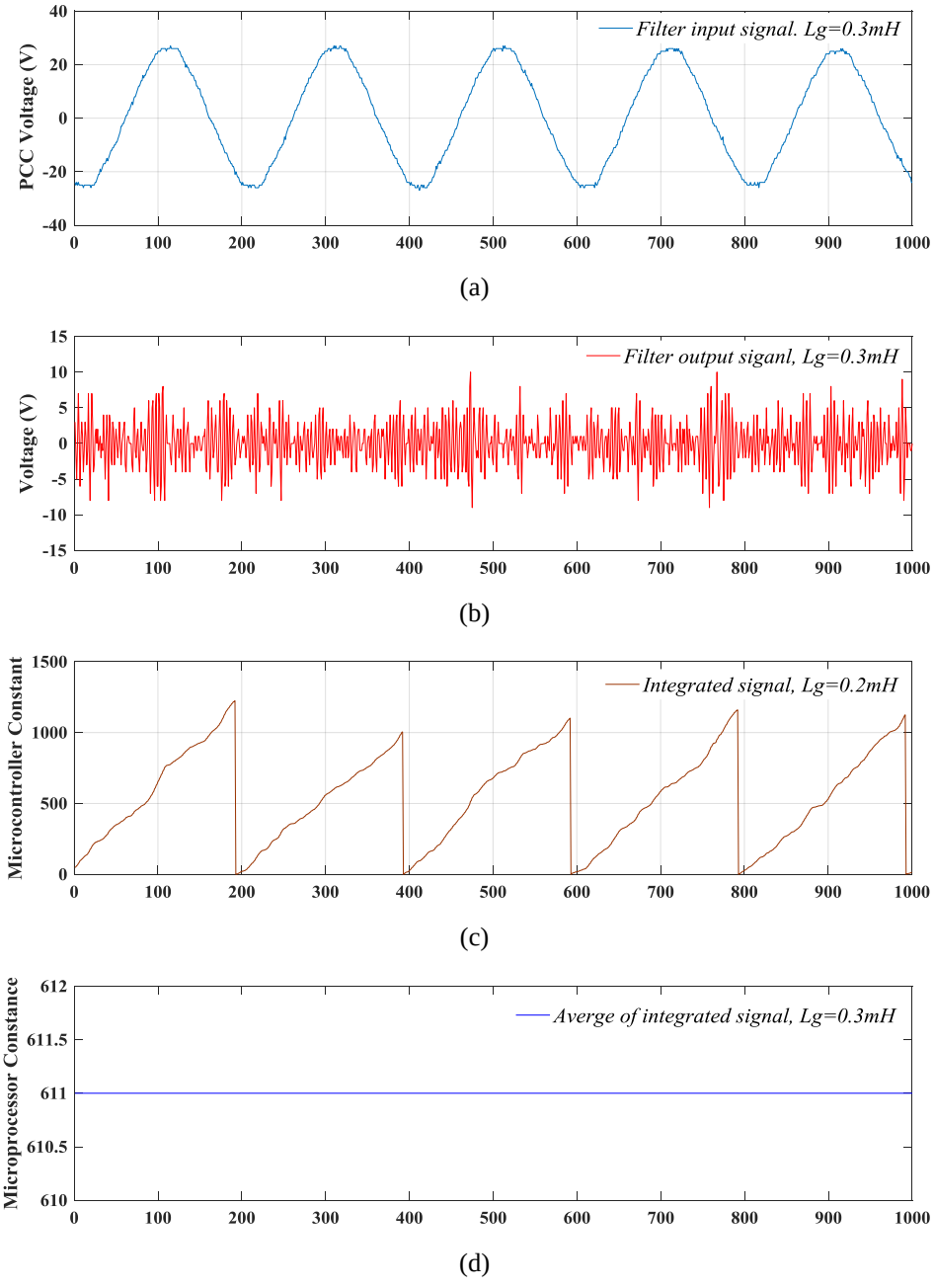

Figure 7-23 Filtering and signal processing operation of PCC voltage at 0.3mH of grid inductance

It can be noticed that the maximum points of the integrated signal in the case of 0.8mH of grid inductance which shown in Figure 7-23.c, are bigger than the corresponding points in the case of 0.3mH of grid inductance. This is because that the oscillation

presents in the PCC voltage signal has a proportional relationship with grid inductance. Moreover, the figures of integrated signals show inconsistency in regards to the maximum points. For this reason the average of the last ten cycles of the integrated signal is calculated and then used in the look-up table. The average of the integrated signal in the case of 0.3mH and 0.8mH of grid inductances are shown in Figures 7-23.d, and 7-24.d, respectively.

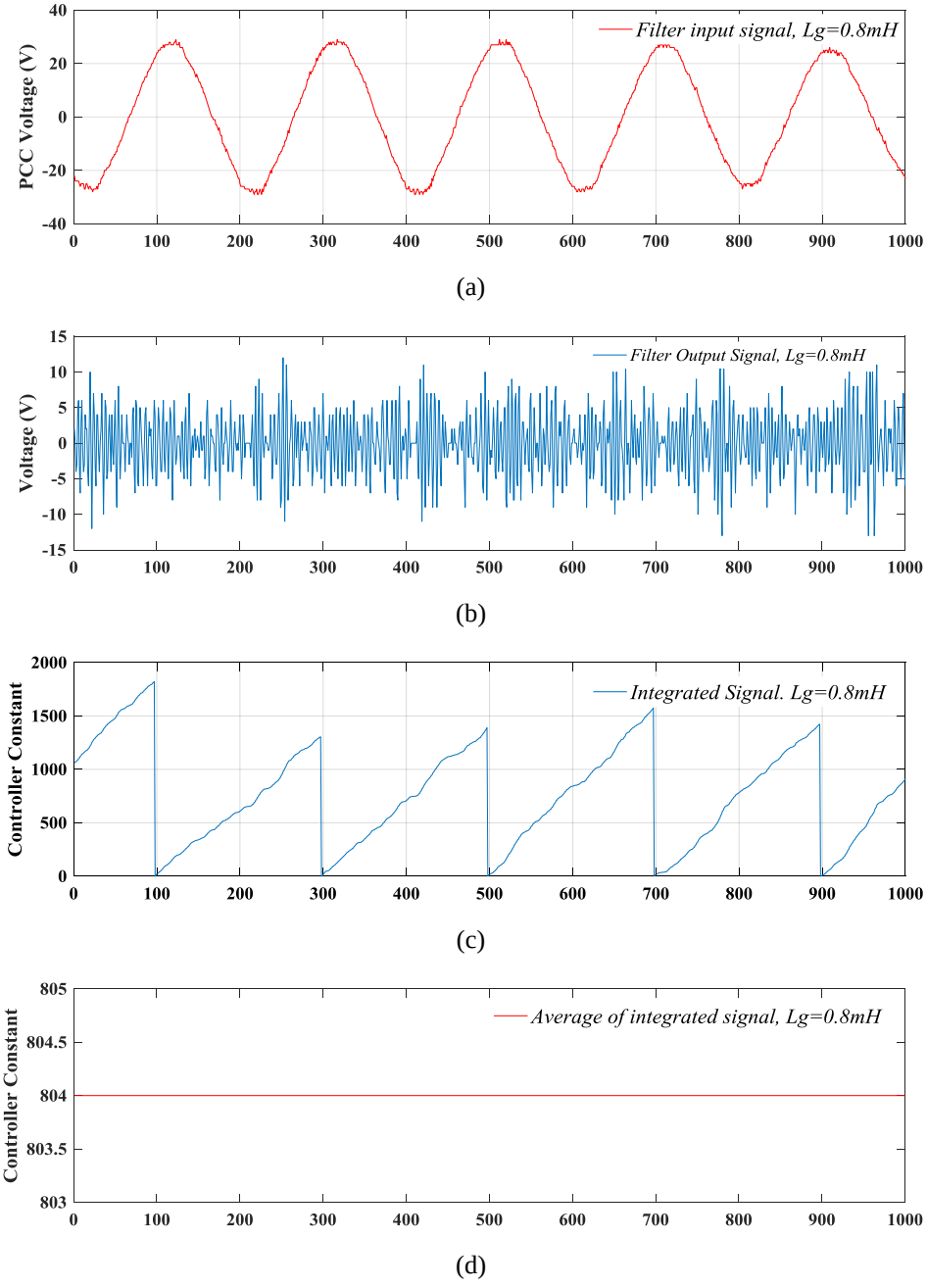

Figure 7-24 Filtering and signal processing operation of PCC voltage at 0.8mH of grid inductance

7.8 Mathematical representation of filtering and processing operation

The operation of band-pass filtering and signal processing have been accomplished within the c-code as expressed in the following equations:

$$Filter\ input = V_{PCC} = u(n) \tag{7.3}$$

$$Filter\ output = b_1 * B_1 - b_2 * B_2 + b_3 * B_3 + b_4 * B_4 + a_1 * A_1 - a_2 * A_2 + a_3 * A_3 - a_4 * A_4 = u(n) \tag{7.4}$$

Where b_1, b_2, b_3 and b_4 are the coefficients of the numerator of the transfer function of the digital band-pass filter in z-domain which is given earlier in equation 7.2, while a_1, a_2, a_3, and a_4 are the coefficients of the denominator of the mentioned transfer function.

Storing the previous states as follow:

$$B_4 = B_3 \tag{7.5}$$

$$B_3 = B_2 \tag{7.6}$$

$$B_2 = B_1 \tag{7.7}$$

$$B_1 = Filter\ input = u(n) \tag{7.8}$$

$$A_4 = A_3 \tag{7.9}$$

$$A_3 = A_2 \tag{7.10}$$

$$A_2 = A_1 \tag{7.11}$$

$$A_1 = Filter\ output = y(n) \tag{7.12}$$

$y(n)$ is the oscillating output signal from the digital band-pass filter. The followed step is to rectify this signal as given in equation 7.14.

$$Rectified\ output = abs(Filter\ output) \tag{7.14}$$

The next step in the signal processing is the integration of the rectified signal which is achieved as follow

$$Integrated\ output = Integrated\ output + Rectified\ output \tag{7.15}$$

$$Accumulater = Accumulater + Integrated\ output \tag{7.16}$$

The accumulate is reset to zero at the end of the control cycle

$$Average\ output = Accumulater/One\ cycle \tag{7.17}$$

$$Accumulater\ counter\ 10\ points = Accumulater\ counter\ 10\ points + Average\ output \tag{7.18}$$

$$Average\ output\ 10\ points = Accumulater\ counter\ 10\ points/10 \tag{7.19}$$

The average of the ten cycle reflects the variation of the grid inductance which used to build the look-up table

7.8.1 Building of look-up table

The look-up table consists of the best values of the PR controller parameters K_P and K_R and the corresponding value of the grid inductance. During the practical experiment, the emulated grid inductance was varied from 0.1mH to 0.8mH of grid inductance and the controller gains were carefully tuned for every case until the lowest THD is guaranteed. The performance of the THD is observed online throughout the power analyser and then the measured dada was transmitted to the Matlab for further analysis with the FFT function. The best gains values obtained experimentally are given in Table 12.

Table 12 Look-up table data for the APR controller

Lg(mH)	Average output 10 points	K_P	K_R	ω_c
0.3	611	0.11	98	5
0.5	714	0.091	82	5
0.8	804	0.082	75	5

7.8.2 Performance of APR against PR controller

To assess the performance of the adaptive PR (APR) controller in terms of harmonic performance improvement, FFT analysis have been carried out to the grid current and PCC voltage for three cases of grid inductances and the results obtained are compared to that of the fixed gains PR controller.

- ***With Lg=0.3mH***

From the previous results in section 7-4-1, the harmonic performance of the grid current and PCC voltage in the case 0.3mH of grid inductance with fixed gains PR controller shows that the THD of grid current and PCC voltage are 3.84% and 3.465 respectively. The controller gains are reduced from 0.129 of KP and 106 of KR to 0.11 of KP and 89 of KR when the grid inductance increased from 0.1mH to 0.3mH. The APR controller responded to this increase by reducing its parameters according to the change in grid inductance. The harmonic profile of grid current and PCC voltage when the APR controller is implemented is shown in Figures 7-25.

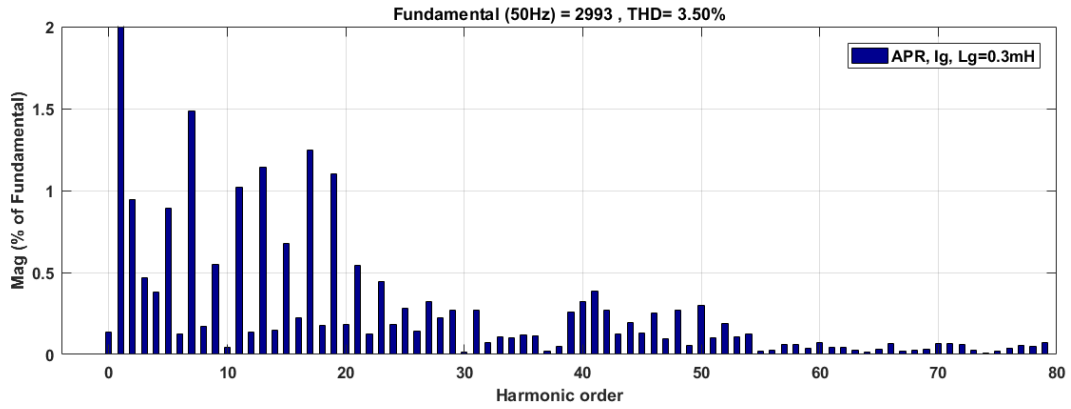

(a) Harmonic profile of grid current at 0.3mH with APR controller

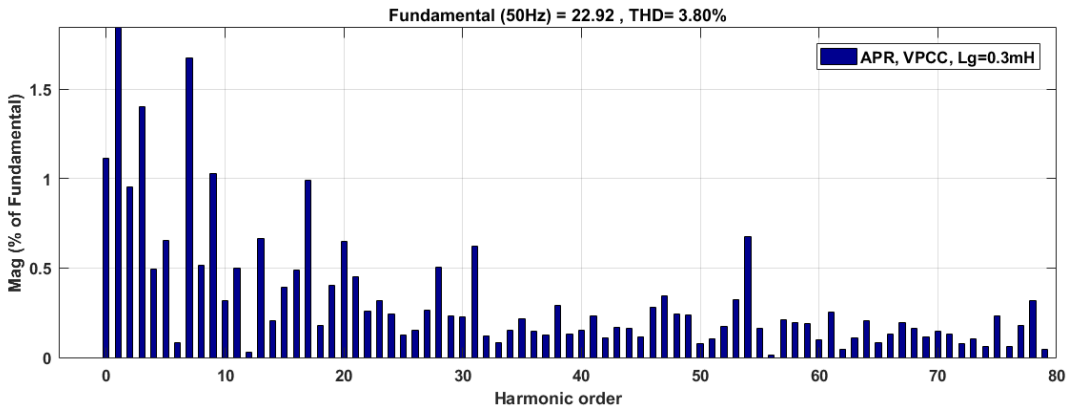

(b)Harmonic profile of PCC voltage at 0.3mH with APR controller

Figure 7-25 Harmonic profile of grid current and PCC voltage at 0.3mH with APR controller (KP=0.11, KR=98)

- ***With Lg=0.5mH***

The harmonic performance of grid current and PCC voltage in the case of 0.5mH of grid inductance is shown in Figure 7-26. The THD of grid current is significantly reduced. This because the APR controller detect the change in grid inductance and changes its parameters accordingly. The THD of grid current is reduced from 3.90% to 3.60% while the THD of PCC voltage increased to 3.84 %. As can be noticed, the THD of PCC voltage in the case of APR controller is larger than that of the PR controller, this the lowest level that can be obtained with the selected value of K_P and K_R. These values are selected as they provide the lowest level of grid current distortion.

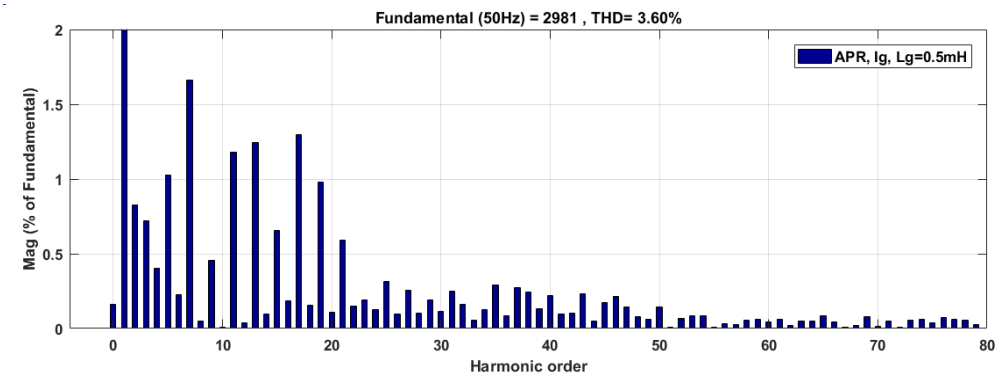

(a) Harmonic profile of grid current at 0.5mH with APR controller

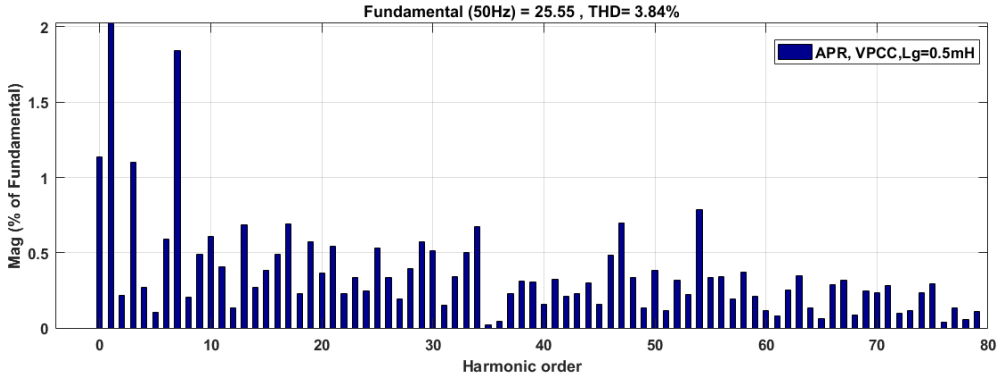

(b) Harmonic profile of PCC voltage at 0.5mH with APR controller

Figure 7-26 Harmonic profile of grid current and PCC voltage at 0.5mH with APR controller (KP=0.091, KR=82)

- ***With Lg=0.8mH***

The harmonic performance of grid current and PCC voltage in the case of 0.5mH of grid inductance is shown in Figure 7-26. The THD of grid current and PCC voltage are significantly reduced. The THD of grid current with APR controller is 3.91% compared to 5.52% with the classical PR controller. While the THD of PCC voltage is also reduced from 4.36% with PR controller to 4.22% with the APR controller.

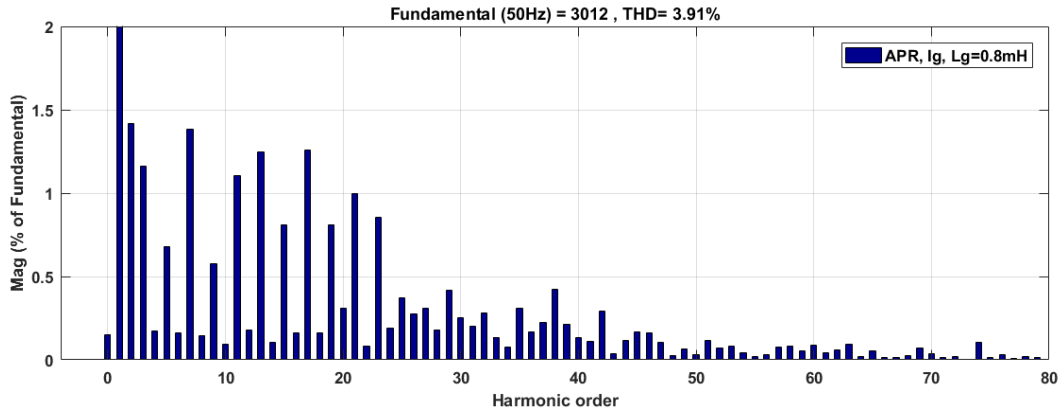

(a) Harmonic profile of grid current at 0.8mH with APR controller

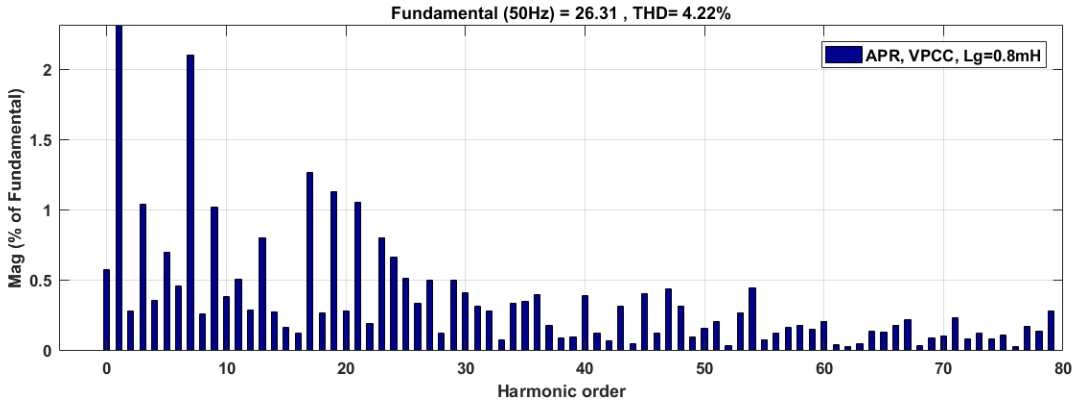

(b) Harmonic profile of PCC voltage at 0.8mH with APR controller

Figure 7-27 Harmonic profile of grid current and PCC voltage at 0.8mH with APR controller (KP=0.081, KR=75)

Table 13 THD comparison of grid current between PI, PR and APR controllers

Lg(mH)	THD%_Ig (PI controller)	THD%_Ig (PR Controller)	THD%_Ig (APR controller)
0.3	4.27	3.84	3.50
0.5	4.55	3.90	3.60
0.8	5.52	5.69	3.91

Table 14 THD comparison of PCC voltage between PI, PR and APR controllers

Lg(mH)	THD%_V (PI controller)	THD%_V (PR Controller)	THD%_V (APR controller)
0.3	3.42	3.46	3.80
0.5	3.63	3.67	3.84
0.8	4.36	4.00	4.22

A comparison of harmonic performance of grid current and PCC voltage between PI, PR and APR controllers are presented in table13 and table 14 respectively. According to the data provided in table 13, the THD of grid current were significantly reduced when the APR controller is used. While the THD of PCC voltage in the case of APR was larger than that of the PI and PR controller as shown in table 14. However, the THD of PCC voltage was reduced again when higher value of grid inductance is presented in the system.

7.9 Chapter summary

This chapter presents the experimental results of the control of a single-phase grid connected inverter. A comparison between the PI and the PR controllers is presented. In addition, the effect of grid inductance variation on the harmonic performance of grid current and PCC voltage is provided. The experimental results shows that the PR controller has a better performance of that of the PI controller in terms of harmonic distortion. Moreover, it has been shown that the increase in grid inductance can affect the power quality of the system. For this reason, a grid inductance estimation technique based on resonance detection is presented. The estimated grid inductance is utilized to adapt the PR controller to this change. Experimental results that the harmonic performance of grid current and PCC voltage is improved with the implementation of the APR controller.

Thesis Conclusion and Future Work

The final chapter of the thesis provides the main drown conclusion and suggests some recommendation for future work.

7.1 Thesis conclusion

Photovoltaic PV systems have shown significant growth in recent years driven by the increasing efficiency and reductions in the cost of PV modules. Today, distribution generation based PV systems have a major contribution to the total electricity production worldwide. However, in grid-connected PV systems, the control part is an important factor to be considered when they are connected to the distribution network. In general, the control part is accomplish by a closed-loop current control system in order to inject a sinusoidal current into the utility grid. The quality of this current has to comply with certain stringent standard such as IEEE 1547 and IEC60725 which dictate specific grid requirements.

This thesis focuses on improving the power quality of the grid current in single-phase grid-connected PV inverter systems. In particular it concerns about improving the harmonic performance of grid current under the variation of grid operating conditions. A single-phase grid-connected inverter has been firstly modelled based on the mathematical representation of its components and then developed into a robust simulation model in MATLAB/Simulink environment. For the control part, the proportional resonant PR controller has been employed in order to regulate the produced current.

The first part of the thesis presents an investigation on the effect of grid operating condition on the harmonic performance of the grid current and voltage at the point of common coupling. These investigations include the effect of three main conditions: grid voltage distortion, grid impedance variation and grid frequency deviation. In regards to the background grid voltage distortion, the harmonic profile of the simulated grid voltage has been generated from a real experimental data of grid voltage. The finding results confirms that the change in the harmonic magnitudes of the background grid voltage has a significant impact on the corresponding harmonic magnitudes of the grid current. To assess the sensitivity towards deviations in the background grid frequency, the simulated VSI was subjected to a frequency shift of ± 1Hz of the

fundamental component (50 Hz). The obtained results showed that the power quality was negatively affected in terms of THD% and DC injection. Furthermore, the grid current THD% and the PCC voltage THD% are both influenced by the ±1 Hz deviation. For example, the THD% of the grid current increases from 3.19% at a grid frequency of 50Hz to 4.18% for a grid frequency of 50.4Hz. The impact was even more significant when the grid frequency was manually set to 51 Hz, where the THD% is found to exceed IEEE1547 standards which was also the scenario for the THD% of PPC voltage. The effects of grid impedance variation on the system performance has been studied for a wide range of grid inductances. Since the LCL filter is interfacing between the voltage source inverter and the grid impedance so their impedances will be coupled leading to changes in the position of the resonance frequency. It has been shown that the higher the grid inductances the lower is the resonance frequency. This can lead to a serious stability problems especially with the profanation of such systems. It has also been demonstrated that the grid impedance variation causes a voltage and current distortion therefor the online information of grid impedance is essential to avoid instability. Accordingly, chapter five presents a simulation results of a novel technique to design an adaptive PR controller taking into account the change in grid inductance values. The proposed technique utilize the resonance frequency to predict the change of grid inductance. A fourth-order digital band-pass filter combined with chain of statistical signal processing are employed to feed the PR controller with grid impedance information and thus retuning the controller gains. The obtained simulation results showed that the proposed controller was able to detect the grid impedance variation and accordingly adapts itself to this change resulting in lower levels of current total harmonic distortion.

In order to practically validate the simulation results, the other part of this thesis (chapters six and seven) presents the test-rig preparation of an experimental single-phase grid-connected inverter. It has been experimentally proven that the variation of grid impedance has influenced the harmonic performance of grid current and PCC voltage leading to higher levels of THD. It has also shown that the effect of grid impedance variation can be significantly reduced by retuning the controller's gains. By applying the proposed APR controller experimentally, it has been clearly demonstrated that the levels of THD in grid current and PCC voltage is reduced.

7.2 Recommendation for future work

Based on the research presented in this thesis, the performance of the current controller can be improved by taking into account the variation in grid operating conditions. As only grid inductance was considered in the proposed current controller, the performance of the current controller can be further improved by including other conditions such as frequency variation. There a considerable amount of researches in the literature on frequency adaptive PR controller, a step further would be to combine this with the proposed APR controller which definitely will improve the robustness of the grid-connected inverter PV systems. So far, the proposed APR controller has been applied only to single-phase H-bridge inverter which only applied for low voltage applications. For the future work, this can be investigated for medium and high voltage application where multi-levels converter are employed.

The particle swarm optimisation algorithm used during the simulation work to optimise the controller gains can be further investigated to be practically implemented online within the microcontroller especially with more powerful DSP unit. Moreover, the data obtained from the digital band-pass filter might be processed in a better way to provide the controller with grid impedance information especially in the case of weak grid where the grid impedance is more volatile and expected to change over time. Another suggestion for future work is to operate the proposed APR controller in the rated power level although the concept has been proven with lower power level.

References

[1] T. Preda, K. Uhlen, and D. E. Nordgård, "An overview of the present grid codes for integration of distributed generation," in *CIRED 2012 Workshop: Integration of Renewables into the Distribution Grid*, 2012, pp. 1-4.

[2] "Renewable 2017 Global Status Report," ed.

[3] *Renewable 2018 Global Status Report*. Available: http://www.ren21.net/gsr-2018/chapters/chapter_01/chapter_01/

[4] S. Kouro, J. I. Leon, D. Vinnikov, and L. G. Franquelo, "Grid-Connected Photovoltaic Systems: An Overview of Recent Research and Emerging PV Converter Technology," *IEEE Industrial Electronics Magazine*, vol. 9, pp. 47-61, 2015.

[5] E. Du, N. Zhang, B. Hodge, Q. Wang, C. Kang, B. Kroposki, *et al.*, "The Role of Concentrating Solar Power Toward High Renewable Energy Penetrated Power Systems," *IEEE Transactions on Power Systems*, vol. 33, pp. 6630-6641, 2018.

[6] Z. Wang, L. Jiang, Z. Zou, and M. Cheng, "Operation of SMES for the Current Source Inverter Fed Distributed Power System Under Islanding Mode," *IEEE Transactions on Applied Superconductivity*, vol. 23, pp. 5700404-5700404, 2013.

[7] Z. Wang, B. Wu, D. Xu, and N. R. Zargari, "Hybrid PWM for High-Power Current-Source-Inverter-Fed Drives With Low Switching Frequency," *IEEE Transactions on Power Electronics*, vol. 26, pp. 1754-1764, 2011.

[8] J. Glasdam, J. Hjerrild, Ł. H. Kocewiak, and C. L. Bak, "Review on multi-level voltage source converter based HVDC technologies for grid connection of large offshore wind farms," in *2012 IEEE International Conference on Power System Technology (POWERCON)*, 2012, pp. 1-6.

[9] B. S. N. Raj, R. Siddharth, and S. M. Shyni, "MPPT with bi-directional DC-DC converter and multi-level inverter for grid connected hybrid system," in *2017 International Conference on Computation of Power, Energy Information and Commuincation (ICCPEIC)*, 2017, pp. 773-777.

[10] W. Qi, J. Liu, X. Chen, and P. D. Christofides, "Supervisory Predictive Control of Standalone Wind/Solar Energy Generation Systems," *IEEE Transactions on Control Systems Technology*, vol. 19, pp. 199-207, 2011.

[11] Z. Yao, L. Xiao, and Y. Yan, "Seamless Transfer of Single-Phase Grid-Interactive Inverters Between Grid-Connected and Stand-Alone Modes," *IEEE Transactions on Power Electronics*, vol. 25, pp. 1597-1603, 2010.

[12] D. S. Ochs, P. Sotoodeh, and B. Mirafzal, "A technique for voltage-source inverter seamless transitions between grid-connected and standalone modes," in *2013 Twenty-Eighth Annual IEEE Applied Power Electronics Conference and Exposition (APEC)*, 2013, pp. 952-959.

[13] R. Kadri, J. Gaubert, and G. Champenois, "An Improved Maximum Power Point Tracking for Photovoltaic Grid-Connected Inverter Based on Voltage-Oriented Control," *IEEE Transactions on Industrial Electronics*, vol. 58, pp. 66-75, 2011.

[14] V. Miñambres-Marcos, E. Romero-Cadaval, M. Á. Guerrero-Martínez, and M. I. Milanés-Montero, "Three-phase single stage photovoltaic inverter with

active filtering capabilities," in *IECON 2012 - 38th Annual Conference on IEEE Industrial Electronics Society*, 2012, pp. 5253-5258.

[15] X. Yaosuo, C. Liuchen, K. Sren Baekhj, J. Bordonau, and T. Shimizu, "Topologies of single-phase inverters for small distributed power generators: an overview," *IEEE Transactions on Power Electronics,* vol. 19, pp. 1305-1314, 2004.

[16] S. B. Kjaer, J. K. Pedersen, and F. Blaabjerg, "A review of single-phase grid-connected inverters for photovoltaic modules," *IEEE Transactions on Industry Applications,* vol. 41, pp. 1292-1306, 2005.

[17] G. Ding, F. Gao, H. Tian, C. Ma, M. Chen, G. He, *et al.*, "Adaptive DC-Link Voltage Control of Two-Stage Photovoltaic Inverter During Low Voltage Ride-Through Operation," *IEEE Transactions on Power Electronics,* vol. 31, pp. 4182-4194, 2016.

[18] M. A. Ghasemi, H. M. Foroushani, and M. Parniani, "Partial Shading Detection and Smooth Maximum Power Point Tracking of PV Arrays Under PSC," *IEEE Transactions on Power Electronics,* vol. 31, pp. 6281-6292, 2016.

[19] C. Moo and G. Wu, "Maximum Power Point Tracking With Ripple Current Orientation for Photovoltaic Applications," *IEEE Journal of Emerging and Selected Topics in Power Electronics,* vol. 2, pp. 842-848, 2014.

[20] A. Sangwongwanich, Y. Yang, and F. Blaabjerg, "High-Performance Constant Power Generation in Grid-Connected PV Systems," *IEEE Transactions on Power Electronics,* vol. 31, pp. 1822-1825, 2016.

[21] S. Jain and V. Agarwal, "A Single-Stage Grid Connected Inverter Topology for Solar PV Systems With Maximum Power Point Tracking," *IEEE Transactions on Power Electronics,* vol. 22, pp. 1928-1940, 2007.

[22] T. Wu, C. Chang, L. Lin, and C. Kuo, "Power Loss Comparison of Single- and Two-Stage Grid-Connected Photovoltaic Systems," *IEEE Transactions on Energy Conversion,* vol. 26, pp. 707-715, 2011.

[23] Y. Shi, B. Liu, and S. Duan, "Eliminating DC Current Injection in Current-Transformer-Sensed STATCOMs," *IEEE Transactions on Power Electronics,* vol. 28, pp. 3760-3767, 2013.

[24] J. Yin, S. Duan, and B. Liu, "Stability Analysis of Grid-Connected Inverter With LCL Filter Adopting a Digital Single-Loop Controller With Inherent Damping Characteristic," *IEEE Transactions on Industrial Informatics,* vol. 9, pp. 1104-1112, 2013.

[25] J. Fang, G. Xiao, X. Yang, and Y. Tang, "Parameter Design of a Novel Series-Parallel-Resonant<italic>LCL</italic>Filter for Single-Phase Half-Bridge Active Power Filters," *IEEE Transactions on Power Electronics,* vol. 32, pp. 200-217, 2017.

[26] H. Liu, Y. Ran, K. Liu, W. Wang, and D. Xu, "A Modified Single-Phase Transformerless Y-Source PV Grid-Connected Inverter," *IEEE Access,* vol. 6, pp. 18561-18569, 2018.

[27] D. Meneses, F. Blaabjerg, G. Ó, and J. A. Cobos, "Review and Comparison of Step-Up Transformerless Topologies for Photovoltaic AC-Module Application," *IEEE Transactions on Power Electronics,* vol. 28, pp. 2649-2663, 2013.

[28] H. Patel and V. Agarwal, "A Single-Stage Single-Phase Transformer-Less Doubly Grounded Grid-Connected PV Interface," *IEEE Transactions on Energy Conversion,* vol. 24, pp. 93-101, 2009.

[29] N. Vázquez, M. Rosas, C. Hernández, E. Vázquez, and F. J. Perez-Pinal, "A New Common-Mode Transformerless Photovoltaic Inverter," *IEEE Transactions on Industrial Electronics*, vol. 62, pp. 6381-6391, 2015.

[30] Y. R. Kafle, G. E. Town, X. Guochun, and S. Gautam, "Performance comparison of single-phase transformerless PV inverter systems," in *2017 IEEE Applied Power Electronics Conference and Exposition (APEC)*, 2017, pp. 3589-3593.

[31] Q. Tran, M. C. Pham, L. Parent, and K. Sousa, "Integration of PV Systems into Grid: From Impact Analysis to Solutions," in *2018 IEEE International Conference on Environment and Electrical Engineering and 2018 IEEE Industrial and Commercial Power Systems Europe (EEEIC / I&CPS Europe)*, 2018, pp. 1-6.

[32] Y. Wu, J. Lin, and H. Lin, "Standards and Guidelines for Grid-Connected Photovoltaic Generation Systems: A Review and Comparison," *IEEE Transactions on Industry Applications*, vol. 53, pp. 3205-3216, 2017.

[33] "IEEE Standard for Interconnecting Distributed Resources with Electric Power Systems - Amendment 1," *IEEE Std 1547a-2014 (Amendment to IEEE Std 1547-2003)*, pp. 1-16, 2014.

[34] Y. Yang, K. Zhou, and F. Blaabjerg, "Current Harmonics From Single-Phase Grid-Connected Inverters—Examination and Suppression," *IEEE Journal of Emerging and Selected Topics in Power Electronics*, vol. 4, pp. 221-233, 2016.

[35] P. P. Das and S. Chattopadhyay, "A Voltage-Independent Islanding Detection Method and Low-Voltage Ride Through of a Two-Stage PV Inverter," *IEEE Transactions on Industry Applications*, vol. 54, pp. 2773-2783, 2018.

[36] E. J. Estebanez, V. M. Moreno, A. Pigazo, M. Liserre, and A. Dell'Aquila, "Performance Evaluation of Active Islanding-Detection Algorithms in Distributed-Generation Photovoltaic Systems: Two Inverters Case," *IEEE Transactions on Industrial Electronics*, vol. 58, pp. 1185-1193, 2011.

[37] I. Agirman and V. Blasko, "A novel control method of a VSC without AC line voltage sensors," *IEEE Transactions on Industry Applications*, vol. 39, pp. 519-524, 2003.

[38] R. Teodorescu, F. Blaabjerg, U. Borup, and M. Liserre, "A new control structure for grid-connected LCL PV inverters with zero steady-state error and selective harmonic compensation," in *Nineteenth Annual IEEE Applied Power Electronics Conference and Exposition, 2004. APEC '04.*, 2004, pp. 580-586 Vol.1.

[39] J. Hu and Z. Q. Zhu, "Improved Voltage-Vector Sequences on Dead-Beat Predictive Direct Power Control of Reversible Three-Phase Grid-Connected Voltage-Source Converters," *IEEE Transactions on Power Electronics*, vol. 28, pp. 254-267, 2013.

[40] L. Tarisciotti, A. J. Watson, P. Zanchetta, S. Bifaretti, J. C. Clare, and P. Wheeler, "An improved Dead-Beat current control for Cascaded H-Bridge active rectifier with low switching frequency," in *6th IET International Conference on Power Electronics, Machines and Drives (PEMD 2012)*, 2012, pp. 1-6.

[41] P. A. Dahono, "New hysteresis current controller for single-phase full-bridge inverters," *IET Power Electronics*, vol. 2, pp. 585-594, 2009.

[42] F. Ma and L. Li, "Research on constant-frequency hysteresis current control in differential three-level grid-connected inverter," in *IECON 2012 - 38th Annual Conference on IEEE Industrial Electronics Society*, 2012, pp. 730-733.

[43] X. Chen, H. Zhang, and J. Zhao, "A new Improvement Strategy based on hysteresis space vector control of Grid-connected inverter," in *2011 International Conference on Advanced Power System Automation and Protection*, 2011, pp. 1613-1617.

[44] T. Ito, H. Miyata, M. Taniguchi, T. Aihara, N. Uchiyama, and H. Konishi, "Harmonic current reduction control for grid-connected PV generation systems," in *The 2010 International Power Electronics Conference - ECCE ASIA -*, 2010, pp. 1695-1700.

[45] Q. Trinh, F. H. Choo, and P. Wang, "Control Strategy to Eliminate Impact of Voltage Measurement Errors on Grid Current Performance of Three-Phase Grid-Connected Inverters," *IEEE Transactions on Industrial Electronics*, vol. 64, pp. 7508-7519, 2017.

[46] T. Ye, N. Dai, C. Lam, M. Wong, and J. M. Guerrero, "Analysis, Design, and Implementation of a Quasi-Proportional-Resonant Controller for a Multifunctional Capacitive-Coupling Grid-Connected Inverter," *IEEE Transactions on Industry Applications*, vol. 52, pp. 4269-4280, 2016.

[47] R. Teodorescu, F. Blaabjerg, M. Liserre, and P. C. Loh, "Proportional-resonant controllers and filters for grid-connected voltage-source converters," *IEE Proceedings - Electric Power Applications*, vol. 153, pp. 750-762, 2006.

[48] M. Ebrahimi and S. A. Khajehoddin, "A simple DQ current controller for single-phase grid-connected inverters," in *2015 IEEE Applied Power Electronics Conference and Exposition (APEC)*, 2015, pp. 2840-2845.

[49] V. Khadkikar, A. Chandra, and B. N. Singh, "Generalised single-phase p-q theory for active power filtering: simulation and DSP-based experimental investigation," *IET Power Electronics*, vol. 2, pp. 67-78, 2009.

[50] J. Choi, Y. Kim, and H. Kim, "Digital PLL control for single-phase photovoltaic system," *IEE Proceedings - Electric Power Applications*, vol. 153, pp. 40-46, 2006.

[51] Y. Sozer and D. A. Torrey, "Modeling and Control of Utility Interactive Inverters," *IEEE Transactions on Power Electronics*, vol. 24, pp. 2475-2483, 2009.

[52] L. Herman, I. Papic, and B. Blazic, "A Proportional-Resonant Current Controller for Selective Harmonic Compensation in a Hybrid Active Power Filter," *IEEE Transactions on Power Delivery*, vol. 29, pp. 2055-2065, 2014.

[53] C. Lascu, L. Asiminoaei, I. Boldea, and F. Blaabjerg, "Frequency Response Analysis of Current Controllers for Selective Harmonic Compensation in Active Power Filters," *IEEE Transactions on Industrial Electronics*, vol. 56, pp. 337-347, 2009.

[54] A. Kuperman, "Proportional-Resonant Current Controllers Design Based on Desired Transient Performance," *IEEE Transactions on Power Electronics*, vol. 30, pp. 5341-5345, 2015.

[55] M. Liserre, R. Teodorescu, and F. Blaabjerg, "Stability of photovoltaic and wind turbine grid-connected inverters for a large set of grid impedance values," *IEEE Transactions on Power Electronics*, vol. 21, pp. 263-272, 2006.

[56] R. Bojoi, L. R. Limongi, D. Roiu, and A. Tenconi, "Frequency-domain analysis of resonant current controllers for active power conditioners," in *2008 34th Annual Conference of IEEE Industrial Electronics*, 2008, pp. 3141-3148.

[57] G. Escobar, P. Mattavelli, A. M. Stankovic, A. A. Valdez, and J. Leyva-Ramos, "An Adaptive Control for UPS to Compensate Unbalance and Harmonic

Distortion Using a Combined Capacitor/Load Current Sensing," *IEEE Transactions on Industrial Electronics*, vol. 54, pp. 839-847, 2007.

[58] H. Wang, W. Zhang, J. Hu, and Y. He, *Design and optimization of proportional resonant controller for rotor current of a wind turbine driven DFIG*, 2008.

[59] S. Nirmal, K. N. Sivarajan, E. A. Jasmin, M. Nandakumar, and B. Jayanand, "Steady state error elimination and harmonic compensation using proportional resonant current controller in grid-tied DC microgrids," in *2018 International Conference on Power, Instrumentation, Control and Computing (PICC)*, 2018, pp. 1-5.

[60] Y. Xiaoming, W. Merk, H. Stemmler, and J. Allmeling, "Stationary-frame generalized integrators for current control of active power filters with zero steady-state error for current harmonics of concern under unbalanced and distorted operating conditions," *IEEE Transactions on Industry Applications*, vol. 38, pp. 523-532, 2002.

[61] D. N. Zmood and D. G. Holmes, "Stationary frame current regulation of PWM inverters with zero steady-state error," *IEEE Transactions on Power Electronics*, vol. 18, pp. 814-822, 2003.

[62] M. Castilla, J. Miret, J. Matas, L. G. d. Vicuna, and J. M. Guerrero, "Linear Current Control Scheme With Series Resonant Harmonic Compensator for Single-Phase Grid-Connected Photovoltaic Inverters," *IEEE Transactions on Industrial Electronics*, vol. 55, pp. 2724-2733, 2008.

[63] N. F. Roslan, J. A. Suul, A. Luna, I. Candela, and P. Rodriguez, "A simulation study of proportional resonant controller based on the implementation of frequency-adaptive virtual flux estimation with the LCL filter," in *IECON 2015 - 41st Annual Conference of the IEEE Industrial Electronics Society*, 2015, pp. 001934-001941.

[64] A. G. Yepes, F. D. Freijedo, J. Doval-Gandoy, L. Ó, J. Malvar, and P. Fernandez-Comesaña, "Effects of Discretization Methods on the Performance of Resonant Controllers," *IEEE Transactions on Power Electronics*, vol. 25, pp. 1692-1712, 2010.

[65] A. Vidal, F. D. Freijedo, A. G. Yepes, P. Fernandez-Comesana, J. Malvar, L. Ó, *et al.*, "Assessment and Optimization of the Transient Response of Proportional-Resonant Current Controllers for Distributed Power Generation Systems," *IEEE Transactions on Industrial Electronics*, vol. 60, pp. 1367-1383, 2013.

[66] M. Castilla, J. Miret, J. Matas, L. G. d. Vicuna, and J. M. Guerrero, "Control Design Guidelines for Single-Phase Grid-Connected Photovoltaic Inverters With Damped Resonant Harmonic Compensators," *IEEE Transactions on Industrial Electronics*, vol. 56, pp. 4492-4501, 2009.

[67] H. S. Goh, M. Armstrong, and B. Zahawi, "The effect of grid operating conditions on the current controller performance of grid connected photovoltaic inverters," in *2009 13th European Conference on Power Electronics and Applications*, 2009, pp. 1-8.

[68] Y. Yang, K. Zhou, and F. Blaabjerg, "Enhancing the Frequency Adaptability of Periodic Current Controllers With a Fixed Sampling Rate for Grid-Connected Power Converters," *IEEE Transactions on Power Electronics*, vol. 31, pp. 7273-7285, 2016.

[69] Y. Yang, K. Zhou, H. Wang, F. Blaabjerg, D. Wang, and B. Zhang, "Frequency Adaptive Selective Harmonic Control for Grid-Connected Inverters," *IEEE Transactions on Power Electronics*, vol. 30, pp. 3912-3924, 2015.

[70] F. Gonzalez-Espin, G. Garcera, I. Patrao, and E. Figueres, "An Adaptive Control System for Three-Phase Photovoltaic Inverters Working in a Polluted and Variable Frequency Electric Grid," *IEEE Transactions on Power Electronics*, vol. 27, pp. 4248-4261, 2012.

[71] K. Seifi and M. Moallem, "An Adaptive PR Controller for Synchronizing Grid-Connected Inverters," *IEEE Transactions on Industrial Electronics*, vol. 66, pp. 2034-2043, 2019.

[72] S. Golestan, E. Ebrahimzadeh, J. M. Guerrero, and J. C. Vasquez, "An Adaptive Resonant Regulator for Single-Phase Grid-Tied VSCs," *IEEE Transactions on Power Electronics*, vol. 33, pp. 1867-1873, 2018.

[73] Y. A. I. Mohamed, "Mitigation of Converter-Grid Resonance, Grid-Induced Distortion, and Parametric Instabilities in Converter-Based Distributed Generation," *IEEE Transactions on Power Electronics*, vol. 26, pp. 983-996, 2011.

[74] C. Citro, P. Siano, and C. Cecati, "Designing Inverters' Current Controllers With Resonance Frequencies Cancellation," *IEEE Transactions on Industrial Electronics*, vol. 63, pp. 3072-3080, 2016.

[75] W. Chen and J. Lin, "One-Dimensional Optimization for Proportional–Resonant Controller Design Against the Change in Source Impedance and Solar Irradiation in PV Systems," *IEEE Transactions on Industrial Electronics*, vol. 61, pp. 1845-1854, 2014.

[76] Y. W. Li, D. M. Vilathgamuwa, F. Blaabjerg, and P. C. Loh, "A Robust Control Scheme for Medium-Voltage-Level DVR Implementation," *IEEE Transactions on Industrial Electronics*, vol. 54, pp. 2249-2261, 2007.

[77] W. Lu, K. Zhou, D. Wang, and M. Cheng, "A General Parallel Structure Repetitive Control Scheme for Multiphase DC–AC PWM Converters," *IEEE Transactions on Power Electronics*, vol. 28, pp. 3980-3987, 2013.

[78] M. Rashed, C. Klumpner, and G. Asher, "Repetitive and Resonant Control for a Single-Phase Grid-Connected Hybrid Cascaded Multilevel Converter," *IEEE Transactions on Power Electronics*, vol. 28, pp. 2224-2234, 2013.

[79] M. A. Azzouz and E. F. El-Saadany, "Multivariable Grid Admittance Identification for Impedance Stabilization of Active Distribution Networks," *IEEE Transactions on Smart Grid*, vol. 8, pp. 1116-1128, 2017.

[80] A. Ghanem, M. Rashed, M. Sumner, M. A. Elsayes, and I. I. I. Mansy, "Grid impedance estimation for islanding detection and adaptive control of converters," *IET Power Electronics*, vol. 10, pp. 1279-1288, 2017.

[81] L. Asiminoaei, R. Teodorescu, F. Blaabjerg, and U. Borup, "A digital controlled PV-inverter with grid impedance estimation for ENS detection," *IEEE Transactions on Power Electronics*, vol. 20, pp. 1480-1490, 2005.

[82] L. Asiminoaei, R. Teodorescu, F. Blaabjerg, and U. Borup, "Implementation and test of an online embedded grid impedance estimation technique for PV inverters," *IEEE Transactions on Industrial Electronics*, vol. 52, pp. 1136-1144, 2005.

[83] Z. Staroszczyk, "A method for real-time, wide-band identification of the source impedance in power systems," *IEEE Transactions on Instrumentation and Measurement*, vol. 54, pp. 377-385, 2005.

[84] J. Sun, "Impedance-Based Stability Criterion for Grid-Connected Inverters," *IEEE Transactions on Power Electronics*, vol. 26, pp. 3075-3078, 2011.

[85] G. Herong, X. Guo, W. Deyu, and W. Wu, "Real-time grid impedance estimation technique for grid-connected power converters," in *2012 IEEE International Symposium on Industrial Electronics*, 2012, pp. 1621-1626.

[86] N. Hoffmann and F. W. Fuchs, "Minimal Invasive Equivalent Grid Impedance Estimation in Inductive–Resistive Power Networks Using Extended Kalman Filter," *IEEE Transactions on Power Electronics*, vol. 29, pp. 631-641, 2014.

[87] M. Ciobotaru, R. Teodorescu, P. Rodriguez, A. Timbus, and F. Blaabjerg, "Online grid impedance estimation for single-phase grid-connected systems using PQ variations," in *2007 IEEE Power Electronics Specialists Conference*, 2007, pp. 2306-2312.

[88] S. Cobreces, E. J. Bueno, D. Pizarro, F. J. Rodriguez, and F. Huerta, "Grid Impedance Monitoring System for Distributed Power Generation Electronic Interfaces," *IEEE Transactions on Instrumentation and Measurement*, vol. 58, pp. 3112-3121, 2009.

[89] J. Yang, W. Li, T. Chen, W. Xu, and M. Wu, "Online estimation and application of power grid impedance matrices based on synchronised phasor measurements," *IET Generation, Transmission & Distribution*, vol. 4, pp. 1052-1059, 2010.

[90] V. Valdivia, A. Lazaro, A. Barrado, P. Zumel, C. Fernandez, and M. Sanz, "Black-Box Modeling of Three-Phase Voltage Source Inverters for System-Level Analysis," *IEEE Transactions on Industrial Electronics*, vol. 59, pp. 3648-3662, 2012.

[91] D. Martin and E. Santi, "Autotuning of Digital Deadbeat Current Controllers for Grid-Tie Inverters Using Wide Bandwidth Impedance Identification," *IEEE Transactions on Industry Applications*, vol. 50, pp. 441-451, 2014.

[92] M. D. Lutovac, D. V. Tošić, and B. L. Evans, *Filter design for signal processing using MATLAB and Mathematica*: Miroslav Lutovac, 2001.

[93] L. Bowtell and T. Ahfock, "Comparison between unipolar and bipolar single phase gridconnected inverters for PV applications," in *2007 Australasian Universities Power Engineering Conference*, 2007, pp. 1-5.

[94] R. Sharma and J. A. R. Ball, "Unipolar switched inverter low-frequency harmonics caused by switching delay," *IET Power Electronics*, vol. 2, pp. 508-516, 2009.

[95] D. Pan, X. Ruan, C. Bao, W. Li, and X. Wang, "Capacitor-Current-Feedback Active Damping With Reduced Computation Delay for Improving Robustness of LCL-Type Grid-Connected Inverter," *IEEE Transactions on Power Electronics*, vol. 29, pp. 3414-3427, 2014.

[96] T. Erika and D. G. Holmes, "Grid current regulation of a three-phase voltage source inverter with an LCL input filter," *IEEE Transactions on Power Electronics*, vol. 18, pp. 888-895, 2003.

[97] J. Xu, S. Xie, L. Huang, and L. Ji, "Design of LCL-filter considering the control impact for grid-connected inverter with one current feedback only," *IET Power Electronics*, vol. 10, pp. 1324-1332, 2017.

[98] R. Peña-Alzola, M. Liserre, F. Blaabjerg, R. Sebastián, J. Dannehl, and F. W. Fuchs, "Analysis of the Passive Damping Losses in LCL-Filter-Based Grid Converters," *IEEE Transactions on Power Electronics*, vol. 28, pp. 2642-2646, 2013.

[99] W. Wu, Y. He, T. Tang, and F. Blaabjerg, "A New Design Method for the Passive Damped LCL and LLCL Filter-Based Single-Phase Grid-Tied

Inverter," *IEEE Transactions on Industrial Electronics*, vol. 60, pp. 4339-4350, 2013.

[100] R. Peña-Alzola, M. Liserre, F. Blaabjerg, M. Ordonez, and Y. Yang, "LCL-Filter Design for Robust Active Damping in Grid-Connected Converters," *IEEE Transactions on Industrial Informatics*, vol. 10, pp. 2192-2203, 2014.

[101] M. B. Saïd-Romdhane, M. W. Naouar, I. Slama-Belkhodja, and E. Monmasson, "Robust Active Damping Methods for LCL Filter-Based Grid-Connected Converters," *IEEE Transactions on Power Electronics*, vol. 32, pp. 6739-6750, 2017.

[102] W. Yao, Y. Yang, X. Zhang, F. Blaabjerg, and P. C. Loh, "Design and Analysis of Robust Active Damping for LCL Filters Using Digital Notch Filters," *IEEE Transactions on Power Electronics*, vol. 32, pp. 2360-2375, 2017.

[103] M. Liserre, F. Blaabjerg, and S. Hansen, "Design and control of an LCL-filter-based three-phase active rectifier," *IEEE Transactions on Industry Applications*, vol. 41, pp. 1281-1291, 2005.

[104] C. Hanju, V. Trung-Kien, and K. Jae-Eon, "Design and control of Proportional-Resonant controller based Photovoltaic power conditioning system," in *Energy Conversion Congress and Exposition, 2009. ECCE 2009. IEEE*, 2009, pp. 2198-2205.

[105] H. M. El-Deeb, A. Elserougi, A. S. Abdel-khalik, S. Ahmed, and A. M. Massoud, "An adaptive PR controller for inverter-based distribution generation with active damped LCL filter," in *GCC Conference and Exhibition (GCC), 2013 7th IEEE*, 2013, pp. 462-467.

[106] B. Li, W. Yao, L. Hang, and L. M. Tolbert, "Robust proportional resonant regulator for grid-connected voltage source inverter (VSI) using direct pole placement design method," *IET Power Electronics*, vol. 5, pp. 1367-1373, 2012.

[107] A. Khairy, M. Ibrahim, N. Abdel-Rahim, and H. Elsherif, "Comparing proportional-resonant and fuzzy-logic controllers for current controlled single-phase grid-connected PWM DC/AC inverters," in *Renewable Power Generation (RPG 2011), IET Conference on*, 2011, pp. 1-6.

[108] R. Teodorescu, F. Blaabjerg, U. Borup, and M. Liserre, "A new control structure for grid-connected LCL PV inverters with zero steady-state error and selective harmonic compensation," in *Applied Power Electronics Conference and Exposition, 2004. APEC '04. Nineteenth Annual IEEE*, 2004, pp. 580-586 Vol.1.

[109] J. K. Pandit, B. Sakthisudhursun, and M. V. Aware, "PR controller implementation using double update mode digital PWM for grid connected inverter," in *Power Electronics, Drives and Energy Systems (PEDES), 2014 IEEE International Conference on*, 2014, pp. 1-6.

[110] H. Cha, T. K. Vu, and J. E. Kim, "Design and control of Proportional-Resonant controller based Photovoltaic power conditioning system," in *2009 IEEE Energy Conversion Congress and Exposition*, 2009, pp. 2198-2205.

[111] R. Teodorescu, F. Blaabjerg, M. Liserre, and P. C. Loh, "Proportional-resonant controllers and filters for grid-connected voltage-source converters," *Electric Power Applications, IEE Proceedings*, vol. 153, pp. 750-762, 2006.

[112] T. Ye, N. Dai, C. S. Lam, M. C. Wong, and J. M. Guerrero, "Analysis, Design, and Implementation of a Quasi-Proportional-Resonant Controller for a Multifunctional Capacitive-Coupling Grid-Connected Inverter," *IEEE Transactions on Industry Applications*, vol. 52, pp. 4269-4280, 2016.

[113] M. Hamzeh, A. Ghazanfari, H. Mokhtari, and H. Karimi, "Integrating hybrid power source into an islanded MV microgrid using CHB multilevel inverter under unbalanced and nonlinear load conditions," in *2014 IEEE PES General Meeting | Conference & Exposition*, 2014, pp. 1-1.

[114] M. Hamzeh, H. Karimi, and H. Mokhtari, "A New Control Strategy for a Multi-Bus MV Microgrid Under Unbalanced Conditions," *IEEE Transactions on Power Systems,* vol. 27, pp. 2225-2232, 2012.

[115] R. Sharma, F. Zare, D. Nešić, and A. Ghosh, "A Hidden Block in a Grid Connected Active Front End System: Modelling, Control and Stability Analysis," *IEEE Access,* vol. 5, pp. 11852-11866, 2017.

[116] Y. Tang, P. C. Loh, P. Wang, F. H. Choo, and F. Gao, "Exploring Inherent Damping Characteristic of LCL-Filters for Three-Phase Grid-Connected Voltage Source Inverters," *IEEE Transactions on Power Electronics,* vol. 27, pp. 1433-1443, 2012.

[117] R. Teodorescu, F. Blaabjerg, M. Liserre, and A. Dell'Aquila, "A stable three-phase LCL-filter based active rectifier without damping," in *38th IAS Annual Meeting on Conference Record of the Industry Applications Conference, 2003.*, 2003, pp. 1552-1557 vol.3.

[118] J. R. Massing, M. Stefanello, H. A. Grundling, and H. Pinheiro, "Adaptive Current Control for Grid-Connected Converters With LCL Filter," *IEEE Transactions on Industrial Electronics,* vol. 59, pp. 4681-4693, 2012.

[119] C. Bao, X. Ruan, X. Wang, W. Li, D. Pan, and K. Weng, "Step-by-Step Controller Design for LCL-Type Grid-Connected Inverter with Capacitor-Current-Feedback Active-Damping," *IEEE Transactions on Power Electronics*, vol. 29, pp. 1239-1253, 2014.

[120] R. Beres, X. Wang, F. Blaabjerg, C. L. Bak, and M. Liserre, "Comparative evaluation of passive damping topologies for parallel grid-connected converters with LCL filters," in *2014 International Power Electronics Conference (IPEC-Hiroshima 2014 - ECCE ASIA)*, 2014, pp. 3320-3327.

[121] I. Hernando-Gil, H. Shi, F. Li, S. Djokic, and M. Lehtonen, "Evaluation of Fault Levels and Power Supply Network Impedances in 230/400 V 50 Hz Generic Distribution Systems," *IEEE Transactions on Power Delivery,* vol. 32, pp. 768-777, 2017.

[122] D. Shmilovitz, "On the definition of total harmonic distortion and its effect on measurement interpretation," *IEEE Transactions on Power Delivery,* vol. 20, pp. 526-528, 2005.

[123] S. Golestan, M. Monfared, F. D. Freijedo, and J. M. Guerrero, "Design and Tuning of a Modified Power-Based PLL for Single-Phase Grid-Connected Power Conditioning Systems," *IEEE Transactions on Power Electronics,* vol. 27, pp. 3639-3650, 2012.

[124] A. Nelson, G. Martin, and J. Hurtt, "Experimental evaluation of grid support enabled PV inverter response to abnormal grid conditions," in *2017 IEEE Power & Energy Society Innovative Smart Grid Technologies Conference (ISGT)*, 2017, pp. 1-5.

[125] A. Canova, L. Giaccone, F. Spertino, and M. Tartaglia, "Electrical Impact of Photovoltaic Plant in Distributed Network," *IEEE Transactions on Industry Applications,* vol. 45, pp. 341-347, 2009.

[126] A. D. Simmons and D. G. Infield, "Current waveform quality from grid-connected photovoltaic inverters and its dependence on operating conditions,"

Progress in Photovoltaics: Research and Applications, vol. 8, pp. 411-420, 2000.

[127] M. Liserre, F. Blaabjerg, and R. Teodorescu, "Grid Impedance Estimation via Excitation of LCL -Filter Resonance," *IEEE Transactions on Industry Applications,* vol. 43, pp. 1401-1407, 2007.

[128] S. Yang, Q. Lei, F. Z. Peng, and Z. Qian, "A Robust Control Scheme for Grid-Connected Voltage-Source Inverters," *IEEE Transactions on Industrial Electronics,* vol. 58, pp. 202-212, 2011.

[129] M. Liserre, R. Teodorescu, and F. Blaabjerg, "Stability of grid-connected PV inverters with large grid impedance variation," in *Power Electronics Specialists Conference, 2004. PESC 04. 2004 IEEE 35th Annual*, 2004, pp. 4773-4779 Vol.6.

[130] M. Mascioli, M. Pahlevani, and P. K. Jain, "Frequency-adaptive current controller for grid-connected renewable energy systems," in *2014 IEEE 36th International Telecommunications Energy Conference (INTELEC)*, 2014, pp. 1-6.

[131] "IEEE Standard for Interconnection and Interoperability of Distributed Energy Resources with Associated Electric Power Systems Interfaces," *IEEE Std 1547-2018 (Revision of IEEE Std 1547-2003)*, pp. 1-138, 2018.

[132] C. Citro, P. Siano, and C. Cecati, "Designing Inverters’ Current Controllers With Resonance Frequencies Cancellation," *IEEE Transactions on Industrial Electronics,* vol. 63, pp. 3072-3080, 2016.

[133] N. Agarwal, M. W. Ahmad, and S. Anand, "Quasi-Online Technique for Health Monitoring of Capacitor in Single-Phase Solar Inverter," *IEEE Transactions on Power Electronics,* vol. 33, pp. 5283-5291, 2018.

[134] M. J. B. Ghorbal, W. Ghzaiel, I. Slama-Belkhodja, and J. M. Guerrero, "Online detection and estimation of grid impedance variation for Distributed Power Generation," in *2012 16th IEEE Mediterranean Electrotechnical Conference*, 2012, pp. 555-560.

[135] M. Liserre, R. Teodorescu, and F. Blaabjerg, "Stability of grid-connected PV inverters with large grid impedance variation," in *2004 IEEE 35th Annual Power Electronics Specialists Conference (IEEE Cat. No.04CH37551)*, 2004, pp. 4773-4779 Vol.6.

[136] D. Z. M. A. Miss Zin Ma Ma Myo, Dr.Zaw Min Naing, "Design and Implementation of Active Band-Pass Filter for Low Frequency RFID (Radio Frequency Identification) System2009 ",.

[137] S. A. Ethni, S. M. Gadoue, and B. Zahawi, "Inter-turn short circuit stator fault identification for induction machines using computational intelligence algorithms," in *2015 IEEE International Conference on Industrial Technology (ICIT)*, 2015, pp. 757-762.

[138] M. Eull, M. Preindl, and A. Emadi, "Analysis and design of a high efficiency, high power density three-phase silicon carbide inverter," in *2016 IEEE Transportation Electrification Conference and Expo (ITEC)*, 2016, pp. 1-6.

[139] P. Kanjiya, V. Khadkikar, and M. S. E. Moursi, "A Novel Type-1 Frequency-Locked Loop for Fast Detection of Frequency and Phase With Improved Stability Margins," *IEEE Transactions on Power Electronics,* vol. 31, pp. 2550-2561, 2016.

[140] F. D. Freijedo, A. G. Yepes, L. Ó, A. Vidal, and J. Doval-Gandoy, "Three-Phase PLLs With Fast Postfault Retracking and Steady-State Rejection of

Voltage Unbalance and Harmonics by Means of Lead Compensation," *IEEE Transactions on Power Electronics*, vol. 26, pp. 85-97, 2011.

[141] Z. Chen and Z. Li, "Robust Precise Time Difference Estimation Based on Digital Zero-Crossing Detection Algorithm," *IEEE Transactions on Instrumentation and Measurement,* vol. 65, pp. 1739-1748, 2016.

[142] P. Rodriguez, A. Luna, I. Candela, R. Mujal, R. Teodorescu, and F. Blaabjerg, "Multiresonant Frequency-Locked Loop for Grid Synchronization of Power Converters Under Distorted Grid Conditions," *IEEE Transactions on Industrial Electronics,* vol. 58, pp. 127-138, 2011.

[143] M. D. Kusljevic, J. J. Tomic, and L. D. Jovanovic, "Frequency Estimation of Three-Phase Power System Using Weighted-Least-Square Algorithm and Adaptive FIR Filtering," *IEEE Transactions on Instrumentation and Measurement,* vol. 59, pp. 322-329, 2010.

[144] B. P. McGrath, D. G. Holmes, and J. J. H. Galloway, "Power converter line synchronization using a discrete Fourier transform (DFT) based on a variable sample rate," *IEEE Transactions on Power Electronics,* vol. 20, pp. 877-884, 2005.

Appendix

Appendix 1 Parameter design of digital Bandpass filter

This Matlab file has been developed in order to determine the parameters of the digital bandpass filter that implemented in the practical experiment and the simulation. The different in the design between the practical and simulation relies on the different between the rated power of the single-phase grid-connected inverter system. The power level determines the parameters of the LCL filter and thus changes the range of the resonance frequency.

```
% after alpha has been determined, all quantities of the practical filters can be
calculated using the following equations:


% 0 = alpha^2+ (alpha*d_o*a_1/ (b_1*(1+alpha^2))) ^2+ (1/alpha^2)-2-(d_o^2/b_1);


% The mid frequency of filter 1 is:
clc
clear all
Fs = 20000;                     % Hz
Ts = 1/Fs;
d_o = 0.6067;                   % Delta Omega =1/Q AND Q = fm/Bw;
a_1 = 1.4142;
b_1 = 1;

%alpha = (gbest (1, end))
alpha=0.8044;
f_min = 1550;
f_max = 2900;
fm = (f_max + f_min)/2

% the mid ferquency of the filter 1 is:
fm1=fm/alpha
% the mid ferquency of the filter 2 is:
fm2 = fm* alpha

% with fm being the mid frequency of the overall fourth-order band-    pass filter.
% the individual pole quality, Qi is the same for both filters:

Bw = f_max - f_min
Q = fm/Bw
Qi = (Q * (1+alpha^2)*b_1)/ (alpha*a_1)
Am =20;

%the individual gain at the mid frequency is the same for both filters
Ami = (Qi/Q)*(sqrt(Am/b_1))

c=100e-9;                % the capacitor value of both filters

R11=1/(2*3.14*fm1*c)     % The input resistance of the first filter

R12=1/(2*3.14*fm2*c)     % The input resistance of the second filter

Rb=1e3                   % the op-Amp upper resistance
%G= 3-(1/Qi)             % the inner gain
G=(3*Qi-1)/Qi
```

```
Ra=Rb/(G-1)              % the op-Amp lower resistance

num1=[(1+(Rb/Ra))/(c*R11) 0];
den1= [1 (1/(R11*c))+(1/(2*R11*c))+(1/(2*R11*c))-(Rb/(Ra*R11*c))
((R11+R11)/(R11*2*R11*R11*c*c))];
G1= tf(num1,den1)                      % transfer function of the first filter
%bode(G1)

num2=[(1+(Rb/Ra))/(c*R12) 0];
den2= [1 (1/(R12*c))+(1/(2*R12*c))+(1/(2*R12*c))-(Rb/(Ra*R12*c))
((R12+R12)/(R12*2*R12*R12*c*c))];
G2= tf(num2,den2)
%bode(G2)                       % transfer function of second filter

GT=G1*G2
bode(GT)
hold on
Gz = c2d (GT, Ts, 'zoh')
bode(Gz)
%bode(G1)

%%%%%%%%%%%%%%%%%%%%%%%%%%%%%%%%%%%%%%%%%%%%%%%%%%%%%%%%%%%%%%%%%%%%%%%%%%%%

                % Filter C Code  22/08/2017

% a1=2.031
% a2=2.617
% a3=1.635
% a4=0.6529
%
% b1=2.657
% b2=3.001
% b3=1.972
% b4=2.3164
%
% float A1,A2,A3,A4, Filter_output ;    // initialize in CLA task 8
% float B1,B2,B3,B4, Filter_input  ;    // initialize in CLA task 8
%
% //Band pass filter for resonant detection
%
% Filter_input  = vg;
%
% Filter_output = b1*B1 -b2*B2 - b3*B3 + b4*B4 + a1*A1 - a2*A2 + a3*A3 - a4*A4;
%
% B4 = B3;
% B3 = B2;
% B2 = B1;
% B1 = Filter_input;                        //   = U(n)
%
% A4 = A3;
% A3 = A2;
% A2 = A1;
% A1 = Filter_output;                       // = Y(n)
%
```

Appendix 2

```
% this code is used for the practical system
close all
clear all
clc

%The given transfer function in case of grid side current is sensed
%(sCfRd+1)/CL1L2/(s(s^2+sCRd(L1+L2)/L1L2C+(L1+L2)/L1L2C))in case of grid
%side current

L1 = 0.6e-3;                                % /0.0514;
Lg=0.1;
L2 = 0.25e-3;                               %+0.4e-3;              %/0.0514;
Cf = 10e-6;                                 %/1.9730e-04;
Rd = 0.1;                                     %/16.1333;
Ts = 1/20000;
Kp = 0.2;                                   % Determine the stability gain and phase
margine
Ki = 150;                                   % 600.0;    Eliminate the steady state
error
wc=10;                                      %cutoff frequency wc
W0=314;
W3=150;                                     % for HC3
W5=250;                                     % for HC5
W7=350;                                     % for HC7

wres2=(L1+L2)/(L1*L2*Cf);                   %wres sequare
ZL2Cf2=1/(Cf*L2)                            %Zlgcf sequare

%with Lg


%Passively damped filter.grid side current
 num = [Cf*Rd/(Cf*L1*L2) 1/(Cf*L1*L2)];
 den = [1 Cf*Rd*(L1+L2)/(Cf*L1*L2) (L1+L2)/(L1*L2*Cf) 0];

Gs = tf (num, den)

%Passively damped filter.inverter side current
%The given transfer function in case of grid side current is sensed.

%s^2+sRdCfZL2Cf2+ZL2Cf^2/sL1*(s^2+sRdCfwres2+wres2)

% num=[1 Cf*Rd/(Cf*L2) 1/(Cf*L2)];
% den=[0.6e-3 0.6e-3*Rd*Cf*wres2 0.6e-3*wres2 0];
% Gs = tf (num, den);
%bode (Gs)

% PR controller

num1 = [Kp 2*Kp*wc+2*Ki*wc Kp*W0*W0];
den1 = [1 2*wc W0^2];

GPR = tf (num1, den1)
%%%%%%%%%%%%%%%%%%%%%%%%%%%%%%%%%%%%%%%%%%

num3 = [2*Ki*wc 0];                                   %HC(S) Tird harmonic
den3 = [1 2*wc W3^2];
GHC3 = tf (num3, den3);


num5 = [2*Ki*wc 0];                                   %HC(S) Fifth harmonic
den5 = [1 2*wc W5^2];
GHC5 = tf (num5, den5);


num7 = [2*Ki*wc 0];                                  %HC(S) Seventh harmonic
den7 = [1 2*wc W7^2];
GHC7 = tf (num7, den7);

GPRT= GPR+GHC3+GHC5+GHC7;


%%%%%%%%%%%%%%%%%%%%%%%%%%%%%%%%%%%%%%%%%%%%%%%%%%%%%%%%%%%%
% Trabnsfer function of PWM
```

```
 num2 = [1];
 den2 = [1.5*Ts 1];

Gpwm = tf (num2, den2)
%Gpwm=1 %%%%%%%% for simple analysis

%cascaded system
Gsys1 = series (GPRT, Gs)                 %%%% lcl filter and PR controller

% Open-loop trasfer function %%%%% loop gain
Gsys2 = series (Gsys1, Gpwm)
%bode(Gsys2)
hold on
%Feedback loop
% num3 = [1 ];
% den3 = [0 1];
% Gf = tf(num3, den3)

Gf=1   %  unity feed back

% Continuous time closed-loop transfer function
Gsys = feedback (Gsys2, Gf)
bode(Gsys)

% Discrete time closed-loop transfer function
Gz = c2d (Gsys, Ts, 'tustin')
Gz = c2d (Gsys, Ts, 'zoh')


% figure
pzmap(Gz) %position of zeros and poles
 pzz1=zpk(Gz)
 hold on
 grid on

%bode(Gs)     %%%%Filter tf Bode Plot
%hold on

% figure
 %bode (Gsys2, 'b')    %open loop tf
%  hold on

%margin(Gsys)      %%closed-loop transfer function
%rlocus (Gsys)     %%closed-loop transfer function
%
%bode (Gz, 'r')
% hold off
% grid
%
% figure
%step (Gsys, 'b')
% hold on
%step (Gz, 'r')
% hold off
% grid
%bode(GPR)

% figure
 %rlocus (Gz)
% grid
%nyquist(Gsys2)
%%%%%%%%%%%%%%%%%%%%%%%%%%%%%%%%%%%%%%%%%%%%%%%%%%%%%%%%%%%%%%%%
%This is to compare Rd=0 and Rd=3.4
Rd = 0;
num=[1 Cf*Rd/(Cf*L2) 1/(Cf*L2)];
den=[0.6e-3 0.6e-3*Rd*Cf*wres2 0.6e-3*wres2 0];

Gs1 = tf (num, den)

Gsyss = series (GPRT, Gs1)                %%%% lcl filter and PR controller

% Open-loop trasfer function %%%%% loop gain
Gsyss = series (Gsyss, Gpwm)
%bode(Gsyss)
%%%%%%%%%%%%%%%%%%%%%%%%%%%%%%%%%%%%%%%%%%%%%%%%%%%%%%%%%%%%%%%%
%This is to see the effect of Kp
```

```
% Kp1=1;Kp2=10; Kp3=50;  Kp4=200;
%
% num11 = [Kp1 2*Kp1*wc+2*Ki*wc Kp1*W0*W0];
% den11 = [1 2*wc W0^2];
%
% GPR11 = tf (num11, den11);
% Gsys11 = series (GPR11, Gs);
% Gsys12 = series (Gsys11, Gpwm);
% Gsys122 = feedback (Gsys12, Gf);
% Gz1 = c2d (Gsys122, Ts, 'tustin')
% pzmap(Gz1) %position of zeros and poles
% %pzz1=zpk(Gz1)
% grid on
% hold on
% %%%%%%%%%%%%%%%%%%%%%%%%%%%%%%%%%%%%%%%%
%
% num22 = [Kp2 2*Kp2*wc+2*Ki*wc Kp2*W0*W0];
% den22 = [1 2*wc W0^2];
%
% GPR22 = tf (num22, den22);
% Gsys22 = series (GPR22, Gs);
% Gsys122 = series (Gsys22, Gpwm);
% Gsys222 = feedback (Gsys122, Gf);
% Gz2 = c2d (Gsys222, Ts, 'tustin');
% pzmap(Gz2) %position of zeros and poles
% %pzz1=zpk(Gz2)
% grid on
% hold on
% %%%%%%%%%%%%%%%%%%%%%%%%%%%%%%%%%%%%%%%%%%%%%%%%
% num33 = [Kp3 2*Kp3*wc+2*Ki*wc Kp3*W0*W0];
% den33 = [1 2*wc W0^2];
%
% GPR33 = tf (num33, den33);
% Gsys33 = series (GPR33, Gs)
% Gsys13 = series (Gsys33, Gpwm);
% Gsys123 = feedback (Gsys13, Gf);
% Gz3 = c2d (Gsys123, Ts, 'tustin')
% pzmap(Gz3) %position of zeros and poles
% %pzz1=zpk(Gz3)
% %grid on
% hold on
% %%%%%%%%%%%%%%%%%%%%%%%%%%%%%%%%%%
% num44 = [Kp4 2*Kp4*wc+2*Ki*wc Kp4*W0*W0];
% den44 = [1 2*wc W0^2];
%
% GPR44 = tf (num44, den44);
% Gsys444 = series (GPR44, Gs);
% Gsys124 = series (Gsys444, Gpwm);
% Gsys144 = feedback (Gsys124, Gf);
% Gz4 = c2d (Gsys144, Ts, 'tustin')
% pzmap(Gz4) %position of zeros and poles
% %pzz1=zpk(Gz4)
% %grid on
```